Reconstruction of the Gulf Stream variability since 1940 using a variational inverse method and study of its interaction with the North Atlantic Oscillation

Sylvain Watelet

A thesis presented for the degree of
Docteur en Sciences

Supervisor: Prof. Jean-Marie Beckers

Focus Research Unit
Department of Astrophysics, Geophysics and Oceanography
University of Liège
Belgium
January 2021

Reconstruction of the Gulf Stream variability since 1940 using a variational inverse method and study of its interaction with the North Atlantic Oscillation

Sylvain Watelet

Abstract

Most part of the research presented in this PhD thesis is published or submitted in international peer-reviewed scientific journals. The following abstract is mainly a compilation of the abstracts of the 3 corresponding publications (Watelet et al., 2017, 2020a,b).

In this study, the Gulf Stream's (GS) response to the North Atlantic oscillation (NAO) is investigated by generating an observation-based reconstruction of the GS path between 70° and 50°W since 1940. Using in situ data from WOD, SeaDataNet, ICES, Hydrobase3 and ARGO floats, a harmonized database of more than 40 million entries is created. A variational inverse method implemented in the software DIVA (Data-Interpolating Variational Analysis) allows the production of time series of monthly analyses of temperature and salinity over the North Atlantic (NA). These time series are used to derive two GS indices: the GS North Wall (GSNW) index for position and the GS Delta (GSD) index as a proxy of its transport. We find a significant correlation (0.37) between the GSNW and the NAO at a lag of 1 year (NAO preceding GS) since 1940 and significant correlations (0.50 and 0.43) between the GSD and the NAO at lags of 0 and 2 years between 1960–2014. We suggest this 2-year lag is due to Rossby waves, generated by NAO variability, that propagate westwards from the center of the NA. This is the first reconstruction of GS indices over a 75-year period based on an objective method using the largest in situ dataset so far. This enhanced tracking and quantification of the GS confirms and extends the temporal scope of this property: NAO+ phases lead to a stronger and more northward GS, and conversely for NAO− phases.

The teleconnections between the NAO and the variability of the GS were extensively studied these last years, often exhibiting time delays between both phenomena. These time lags, usually ranging between 0–2 years, are sometimes explained by the hypothesis of baroclinic Rossby waves generated by the NAO in the central NA and travelling westward before interacting with the GS. In this study, we use a numerical hindcast at an eddy-resolving resolution (1/12°) from the DRAKKAR project to examine the occurrence and properties of such Rossby waves between 1970–2015, thus including a large pre-TOPEX/Poseidon period. Through the use of a two-dimensional Radon Transform (2D-RT) on Hovmöller diagrams of the Sea Surface Height (SSH), a methodology easily portable to other oceanic model outputs, we show evidence of baroclinic Rossby waves travelling at 39°N at a speed of 4.17 $\mathrm{cm\,s^{-1}}$. This study extends the period over which Rossby waves have been

found that far north to a much longer period, which reinforces the findings of previous works. These results are consistent with the time lags observed between the NAO and the GS transport while the GS latitudinal shifts might obey additional processes.

The Barents Sea, located between the Norwegian Sea and the Arctic Ocean, is one of the main pathways of the Atlantic Meridional Overturning Circulation. Changes in the water mass transformations in the Barents Sea potentially affect the thermohaline circulation through the alteration of the dense water formation process. In order to investigate such changes, we present here a seasonal atlas of the Barents Sea including both temperature and salinity for the period 1965–2016. The atlas is built as a compilation of datasets from the World Ocean Database, the Polar Branch of Russian Federal Research Institute of Fisheries and Oceanography, and the Norwegian Polar Institute using the DIVA tool. DIVA allows for a minimization of the expected error variance with respect to the true field. The atlas is used to provide a volumetric analysis of water mass characteristics and an estimation of the ocean heat and freshwater contents. The results show a recent "Atlantification" of the Barents Sea, that is a general increase of both temperature and salinity, while its density remains stable. The atlas is made freely accessible as handy NetCDF files to encourage further research in the Barents Sea physics (10.21335/NMDC-2058021735, Watelet et al. (2020c)).

Reconstruction de la variabilité du Gulf Stream depuis 1940 à l'aide d'une méthode variationnelle inverse et étude de son interaction avec l'oscillation nord-atlantique

Sylvain Watelet

Résumé

La plupart du travail de recherche présenté dans cette thèse de doctorat est publiée ou soumise dans des revues scientifiques internationales à comité de lecture. Le résumé ci-dessous est principalement une compilation des abstracts des 3 publications correspondantes (Watelet et al., 2017, 2020a,b).

Dans cette étude, la réponse du Gulf Stream (GS) à l'oscillation nord-atlantique (NAO) est examinée en générant une reconstruction, basée sur des observations, de la position du GS entre 70° et 50°O depuis 1940. À partir de données in situ de WOD, SeaDataNet, ICES, Hydrobase3 et des bouées ARGO, une base de données harmonisée de plus de 40 millions d'entrées est créée. Une méthode variationnelle inverse implémentée dans le logiciel DIVA (Data-Interpolating Variational Analysis) permet la production de séries temporelles d'analyses mensuelles de température et salinité en Atlantique Nord (NA). Ces séries temporelles sont utilisées pour dériver deux indices de GS: le mur nord du GS (GSNW) pour sa position et le delta du GS (GSD) comme proxy de son transport. Nous trouvons une corrélation significative (0.37) entre le GSNW et la NAO avec un décalage de 1 an (la NAO précédant le GS) depuis 1940 et des corrélations significatives (0.50 et 0.43) entre le GSD et la NAO avec des décalages de 0 et 2 ans pour la période 1960–2014. Nous suggérons que ce décalage de 2 ans est causé par des ondes de Rossby, générées par la variabilité de la NAO, qui se propagent vers l'ouest à partir du centre du NA. Il s'agit de la première reconstruction d'indices de GS, sur une période de 75 ans, basée sur une méthode objective utilisant le set de données le plus étendu jusqu'à présent. Ces localisation et quantification améliorées du GS confirment et étendent la portée temporelle de cette propriété : les phases NAO+ amènent un GS plus intense et plus au nord, et inversement pour les phases NAO−.

Les couplages entre la NAO et la variabilité du GS ont été étudiés de manière extensive ces dernières années, mettant souvent en évidence des décalages temporels entre les deux phénomènes. Ces décalages temporels, en général compris entre 0 et 2 ans, sont parfois expliqués par l'hypothèse d'ondes de Rossby baroclines générées par la NAO dans le NA central et se propageant vers l'ouest avant d'interagir avec le GS. Dans cette étude, nous utilisons une simulation numérique du projet DRAKKAR résolvant les phénomènes tourbillonaires (1/12°) pour analyser l'occurence et les propriétés de telles ondes de Rossby entre 1970 et 2015, ce qui inclut une large période précédant TOPEX/Poseidon. En utilisant une transformée de Radon en deux dimensions (2D-RT) sur des diagrammes d'Hovmöller du niveau de la mer (SSH),

une méthodologie aisément compatible avec d'autres sorties de modèles océaniques, nous montrons des preuves d'ondes de Rossby se propageant à 39°N avec une vitesse de $4.17\,\mathrm{cm\,s^{-1}}$. Cette étude étend grandement la période sur laquelle des ondes de Rossby aussi septentrionales ont été découvertes, ce qui renforce les travaux précédents. Ces résultats sont cohérents avec les décalages temporels observés entre la NAO et le transport du GS, tandis que les mouvements latitudinaux du GS pourraient obéir à des processus additionnels.

La mer de Barents, située entre la mer de Norvège et l'Océan Arctique, est l'une d'est principales voies empruntées par la circulation méridienne de retournement atlantique (AMOC). Les changements dans les transformations des masses d'eau en mer de Barents affectent potentiellement la circulation thermohaline de par l'altération des processus de formation d'eaux profondes. Afin d'examiner de tels changements, nous présentons ici un atlas saisonnier de la mer de Barents incluant à la fois la température et la salinité pour la période 1965–2016. L'atlas est construit comme une compilation de sets de données du World Ocean Database, du Polar Branch of Russian Federal Research Institute of Fisheries and Oceanography, et du Norwegian Polar Institute, en utilisant l'outil DIVA. DIVA permet une minimisation de la variance de l'erreur attendue par rapport au champ réel. L'atlas est utilisé pour fournir une analyse volumétrique des caractéristiques des masses d'eau et une estimation des contenus de chaleur et d'eau douce de l'océan. Les résultats montrent une récente "Atlantification" de la mer de Barents, c'est-à-dire une augmentation générale de la température et de la salinité, tandis que sa densité reste stable. L'atlas est accessible gratuitement sous forme de fichiers NetCDF faciles à utiliser afin d'encourager de plus amples recherches sur la physique de la mer de Barents (10.21335/NMDC-2058021735, Watelet et al. (2020c)).

Acknowledgements

Ne dit-on pas qu'une femme qui éclabousse un homme, c'est un peu comme la rosée d'une matinée de printemps : c'est la promesse d'une belle journée et la perspective d'une soirée enflammée ? La partie "remerciements" d'une thèse, c'est exactement pareil. Premièrement, il n'y a pas d'illusion à se faire, la lecture de ce pavé vous emmènera au-delà du coucher du soleil, et j'en profite déjà pour vous en remercier bien bas. Deuxièmement, il est certain qu'à l'évocation des résultats proprement bluffants obtenus au prix de 2 laptops, 4 disques durs, 3 paires de lunettes, 6 chaises de bureau, 7 collègues de bureau, 1 pointeur laser volé à mon promoteur de thèse (pardon Jean-Marie), tomber en pâmoison est une expression qui vous semblera bien terne.

Mais au contraire d'Hubert Bonisseur de la Bath, la gratitude n'est pour moi pas un vain mot. Je la partage chaleureusement avec ceux qui m'ont apporté leur bienveillance durant la préparation de cette thèse. Lorsque l'on termine sa thèse à 30 ans après l'avoir commencée plus de 7 ans auparavant, de nombreux apprentissages ont été réalisés en cours de route, et certainement pas que dans le domaine scientifique. Cette expérience de longue durée a été concomitante avec une série de réalisations et de prises de conscience, et pour tout cela j'éprouve également beaucoup de gratitude. Quel honnête homme ne préférerait pas le tumulte des eaux chaudes du Gulf Stream à un fleuve tranquille ? Je remercie donc la Vie de m'amener de plus en plus régulièrement à la croisée des chemins.

Plus spécifiquement, et sans aucune attention apportée à l'ordre ni à l'exhaustivité. Brice, je n'oublierai pas de sitôt la confiance que tu m'accordes en amitié, j'en connais la valeur. Les soirées en terre batave se terminant dans les caves poisseuses d'Utrecht me laissent un goût amer mais néanmoins fort agréable. J'ai hâte de beugler à nouveau avec toi "On the rocky road to Dublin" au Temple Bar. Raphaël, ta bonne humeur constante et contagieuse ne me laisse pas de marbre. Tu es le seul à être fier d'affonner des mineurs d'âge, et pour cela on ne peut que t'applaudir. Tes blagues salasses me filent la gerbe (coucou Nicolas), mais entre nous j'aime cela. Puisse le clan des trois mousquetaires de la climatologie liégeoise se réunir à nouveau en 2021 sous un chapiteau miteux de Saint-Jean-Sart, une Val Dieu dans la main droite, et une autre dans l'autre. Charles, merci pour ton soutien volontaire et tes précieux conseils, notamment en LaTeX, j'apprécie beaucoup tes initiatives et ta modestie. Jean-Marie, je suis très reconnaissant pour la liberté que tu m'as laissée dans le choix du sujet de thèse, dans les voyages à l'étranger, dans la gestion de mon temps. Ta créativité scientifique est impressionnante et elle a contribué significativement à la richesse de ce manuscript. Les soirées dans les Cantons de l'Est, dans un style moins potache que les précédentes, n'en comptent pas moins parmi

les meilleures que j'ai connues à ce jour. Merci !

A special thanks to a special girl, you truly are a great person. I feel very lucky I had the chance to meet your soul.

I am also grateful to the Norwegian team who welcomed me heartily in Bergen, you all did a great job! Special thanks to Vidar and Øystein for helping with the paper on the Barents Sea. I feel also very grateful that I had the chance to meet you Helge and your wife in this amazing house of yours next to this fjord, I spent a perfect evening there just before boarding the night train to Oslo... Thank you for the memories.

Of course, thank you to all the jury members for accepting to read thoroughly this manuscript, and thank you in advance for torturing me with all these challenging questions during my thesis defence.

Many other people should be thanked, including persons from the IMR, PINRO, DRAKKAR team, NPI, GHER, NOAA, UOC, the colleagues of the RMI and many others friends. For those people that I forgot to mention, you should feel lucky because the day I remember you is also the day you get a good Belgian beer for free. How great is that?

DIVA was developed by the GHER and improved in the frame of the SeaDataNet project. The DIVA development has received funding from the European Union Sixth Framework Programme (FP6/2002–2006) under grant agreement n°026212, SeaDataNet, Seventh Framework Programme (FP7/2007–2013) under grant agreement n°283607, SeaDataNet II, and project EMODNet (MARE/2008/03 - Lot 3 Chemistry - SI2.531432) from the Directorate-General for Maritime Affairs and Fisheries. The National Oceanographic Data Center (NODC), International Council for the Exploration of the Sea (ICES), HydroBase3, SeaDataNet, Coriolis and Argo projects greatly helped the production of the present version of the monthly analyses by making the data freely available.

Contents

Chapter 1

Introduction: Gulf Stream and Atlantic Meridional Overturning Circulation

Contents

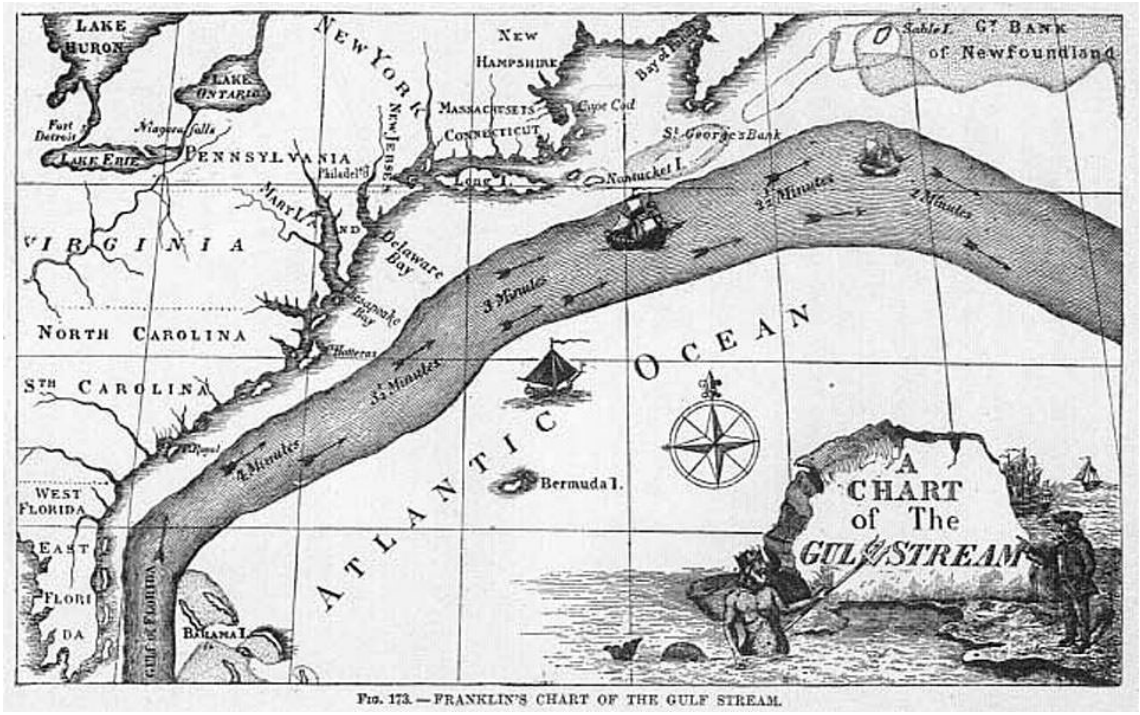

FIG. 173.—FRANKLIN'S CHART OF THE GULF STREAM.

Figure 1.1: First chart of the GS as observed by Franklin and Folger in 1769. Source: `https://oceanservice.noaa.gov/facts/bfranklin.html`

1.1 Gulf Stream

1.1.1 A bit of history

The Gulf Stream (GS), a highly topical issue nowadays in a changing climate, was seen as nothing but a strong contrary current on the 22^th of April 1513 when Juan Ponce de Léon found it out (Voituriez, 2006). Back then, the GS was mainly seen through pragmatic eyes as the contemporary concerns were focused on easy sailing and productive fishing. Although the American seafarers were reported to use this information in order to speed up the travel time across the North Atlantic (NA), this fact did not seem to occur to their English counterparts until 1769 when Benjamin Franklin draw the first detailed chart of the Gulf Stream (see Fig. 1.1). His cousin, Timothy Folger, even reported this colourful exchange between American and English sailors: "*We have informed them that stemming a current, that was against them to the value of three miles an hour; and advised them to cross it and get out of it; but they were too wise to be counselled by simple American fishermen*" (Manning & Cogliano, 2008).

In order to better describe such currents and following Franklin's advices, the crews started to systematise the sea temperature observations, all reported in their logbook (Voituriez, 2006). Since then, the scientific interest for the GS started to increase with specific ships and measurement campaigns designed accordingly. During the XX^{th} century, the mathematical formulation of such Western Boundary Current (WBC) improved as well as the understanding that the GS is only a part of a larger circulation pattern in the NA (see Section 1.2). Today, the GS is extensively

examined on a daily-basis by in situ data (moorings, drifters, ships, gliders,...), satellite sensors and numerical models in order to better assess its variability and the interactions with the rest of the climate system. The GS is not seen as a fixed river anymore but rather as a full share climate component changing at various scales in both space and time. The yearly amount of scientific publications shows no signs of decrease and definitely makes the GS one of the hottest topic in ocean science at present.

1.1.2 Definition

The exact definition of the GS varies among authors, in particular when it comes to its spatial extent. Within this thesis, we stick to the most restrictive one, which defines its western limit at the Cape Hatteras and its eastern one at the longitude of the southern tip of the Greenland in the NA. Between these longitudes, the GS flows in an open-ocean and its latitude is mostly constant, which simplifies its study. Upstream of the Cape Hatteras, the Florida Current flows from the straits of Florida to the southeastern US coast before joining the GS. The GS is continued downstream as the North Atlantic Current (NAC) of drift, and is a much broader and diffuse current that meanders less than the GS. As a result, cold or warm eddies are generally not generated by this current (Rossby, 1996).

The GS is a surface and subsurface current that extends up to a depth of 1000 m. At the surface, speeds have an order of magnitude of $2\,\mathrm{m\,s^{-1}}$ while at 1000 m, the speed is below $1\,\mathrm{m\,s^{-1}}$. At higher depths, a GS influence can still be detected but is much weaker (Johns et al., 1995). Rossby et al. (2014) estimated the GS transport at 94.5 Sv close to the Cape Hatteras, reaching 150 Sv at the longitude of Grand Banks (Hogg, 1992). The GS is actually the Western Boundary Current (WBC) of the NA, similarly to the Kurushio in the North Pacific Ocean or to the Agulhas current in the southern hemisphere (Indian Ocean). The origin of the WBC is explained in Section 1.2.

1.2 Atlantic Meridional Overturning Circulation (AMOC)

Looking at the broader picture, several currents allow the exchange of energy between low and high latitudes, both at the ocean surface and deeper levels. A representation of these connected currents is shown in Figure 1.2. The surface cirulation for the whole Atlantic is depicted in Figure 1.3. In this Figure, the waters of the subtropical gyre in the NA shows a clockwise motion, and conversely in the subtropical gyre of the South Atlantic. Given the theory of the Ekman transport, this type of configuration generates a downwelling due to the average wind stress which has a similar shape as the gyre patterns. A Sverdrup meriodional transport is thus yielded from the center of each subtropical gyre towards the Equator. The conservation of mass requires this water flux to be compensated by a poleward flux, but it is shown that such a flux can only follow the Sverdrup theory if it corresponds to a narrow boundary current travelling along the western side of each ocean basin, which ex-

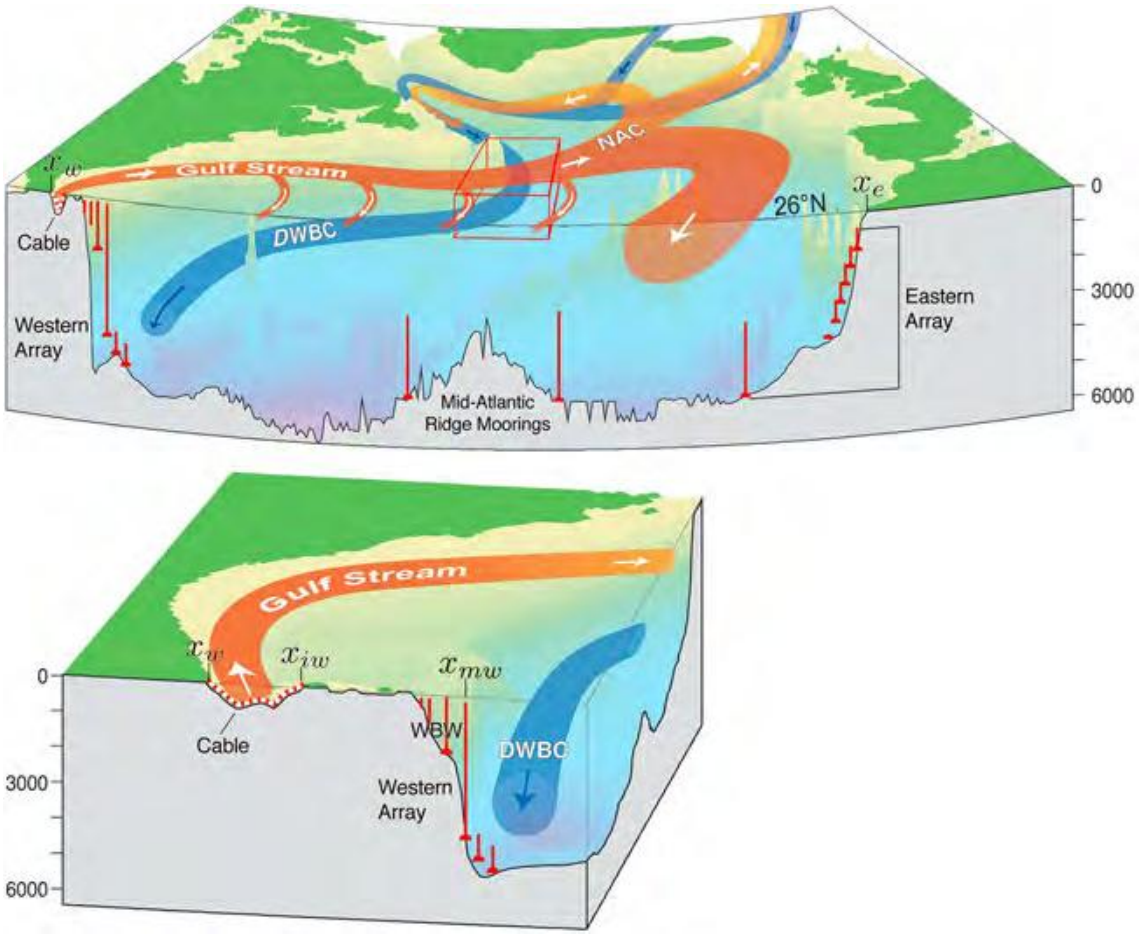

Figure 1.2: Representation of the AMOC as published by Church (2007) and modified by Buckley & Marshall (2016).

plains the GS and other WBCs. The theory behind this descriptive explanation is fully detailed in Cushman-Roisin & Beckers (2011).

1.3 Environmental impacts

1.3.1 Weather and climate

While this thesis focuses on the impacts of the atmosphere on the ocean, the teleconnections go both ways and neither the GS nor the NAC depart from this rule.

The GS is associated with an important meridional Sea Surface Temperature (SST) gradient, and a perturbation of this SST field was shown by Booth et al. (2012) to increase the strength of the storms. According to the review made by Kelly et al. (2010), the cross-frontal SST gradients in the GS also impact the lower atmosphere and intensifies the cyclogenesis in this area. However, although the ocean forcing on the storm activity is significant in the GS region, the upper-level atmospheric circulation remains described as the most important driver of storm intensification by Booth et al. (2012). Finally, Li et al. (2004) recently showed the GS can induce a very long cloud line parallel to its axis, provided the sky is clear

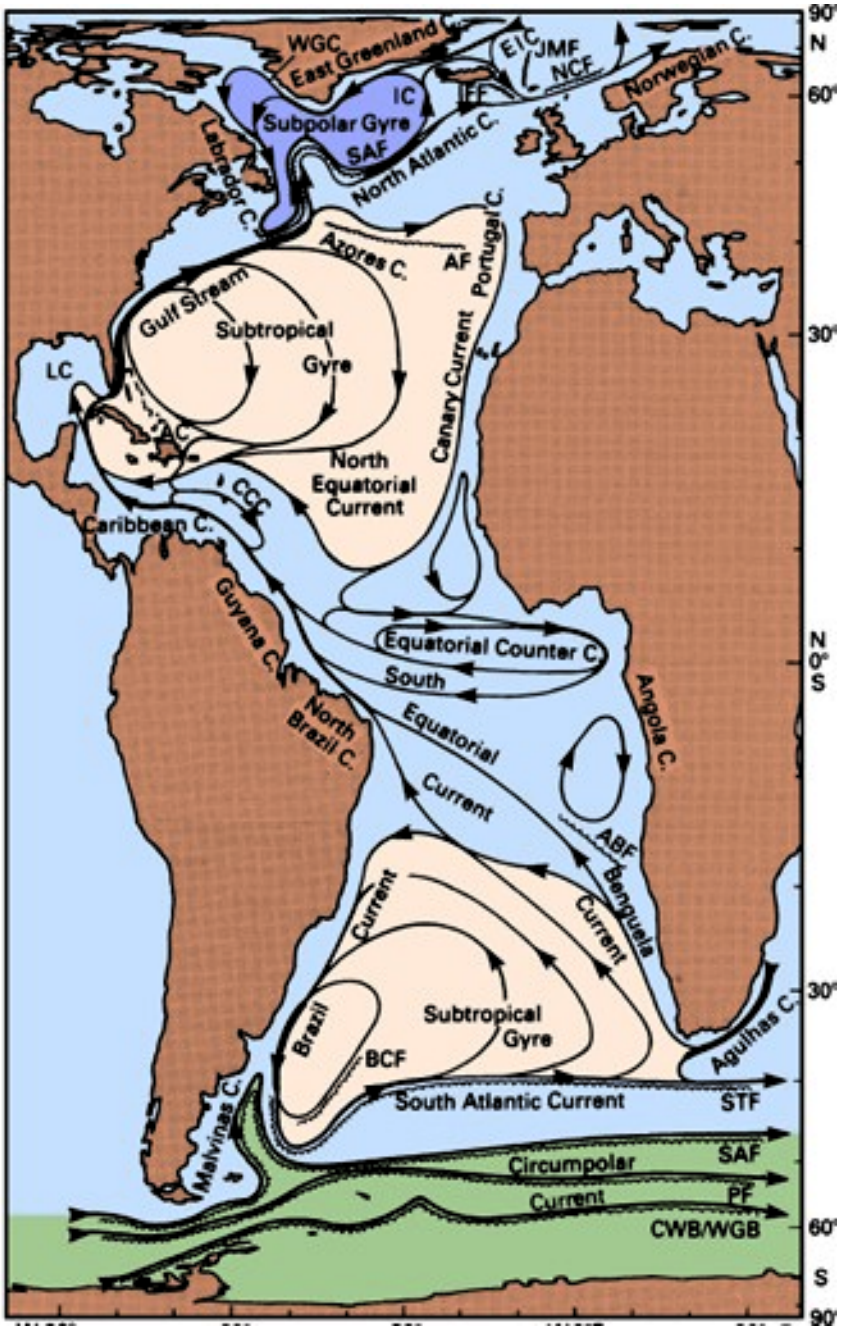

Figure 1.3: Average circulation at the surface of the Atlantic from Tomczak & Godfrey (2003).

and the low-level wind does not perturb this pattern.

The GS is associated with a sea level slope between its northern and southern sides. If the current weakens, the sea level will be lower offshore and higher onshore, along the coast. This correlation is reported on both short and long time scales by Ezer & Atkinson (2014), leading to a risk of an higher sea-level rise near the Cape Hatteras in case of a future weakening of the GS.

Although the GS and the NAC bring heat towards the North-Western Europe, it is shown that the milder winters in Europe with respect to similar latitudes in America are mostly due to the atmospheric circulation and do not require a dynamical ocean (Seager et al., 2002).

1.3.2 Biology and fisheries

The GS North Wall (GSNW) separates the cold biologically productive waters to the north from the warm less productive waters to the south. The shifts in its position are thus important for the marine biology (Hameed et al., 2018). Borkman & Smayda (2009) showed the plankton species *Skeletonema costatum* to be statistically related to variations of the GSNW path. During years with a GSNW shifted to the south, the Summer abundance was 3-fold higher and even 10-fold higher during Winter-Spring.

Regarding fisheries, Nye et al. (2011) showed that the silver hake (*Merluccius bilinearis*) spatial distribution at the North-East US shelf is highly correlated with the GS position, with a time lag of 6 months (GS leading the silver hake). A correlation was also found between the GS position and the recruitement of a yellowtail flounder (*Limanda ferruginea*): a northern GS yields a drop in the abundance of the fish one year later (Xu et al., 2018).

1.4 Global warming

Nowadays, there is a general scientific consensus on the existence of an anthropogenic global warming. Evidence of this consensus can be shown by looking at the scientific literature covering that topic. Cook et al. (2013) analyzed 11944 abstracts of peer-reviewed scientific papers including the words “global climate change” or “global warming”. Looking at the part of these papers expressing a position on the anthropogenic global warming, a crushing 97.1% endorse it, while only 1.9% reject it and 1.0% are uncertain. This percentage of rejection is slightly decreasing over time, the theory that the global warming is not mainly caused by human activities is thus currently vanishing. Moreover, looking at the simple rejection of the global warming can only yields lower figures. In this thesis, the global warming is thus considered as a scientific fact.

The evolution of the AMOC and the GS in this warming context is less certain though. The global warming could weaken the AMOC in several ways. Firstly, an higher amount of poleward moisture can induce increased precipitation and runoff. This freshwater flux in the deep convection areas could stabilize the water column. The melting Arctic ice caps and Greenland ice sheet would also tend to favor a slowdown of the AMOC by weakening the deep-water formation processes (Bakker

et al., 2016). According to the IPCC (Stocker et al., 2013), there is no evidence of a long-term trend in the past observations of the AMOC and its components. Parker & Ollier (2016) also concluded to a stability of the AMOC since 1860, but the debate is still alive since Caesar et al. (2018) concluded to a weakening of the AMOC by ∼15% since 1950. In addition, Smeed et al. (2014) observed a significant decrease of 2.7 Sv in the AMOC between 2004–2008 and 2008–2012, although this period is very short to draw further conclusions. Regarding the future, the IPCC reports (Solomon et al., 2007; Stocker et al., 2013) show that the AMOC is predicted to weaken over the 21^{st} century ("very likely"). However, Stocker et al. (2013) also conclude that a collapse of the AMOC is very unlikely within the course of this century.

Regarding the GS, the evidence suggest a recent stability. Smeed et al. (2014) showed the GS transport decreased by 0.2 Sv between 2004–2008 and 2008–2012. However, this GS negative trend is not statistically significant. The stability of the GS transport is strengthened by the study of Rossby et al. (2014) using Doppler current profilers and showing no significant trend over the longer 1992–2012 period. It is important to understand that the GS is primarily influenced by the wind stress curl and not by the variability of the other AMOC components, which can however play a secondary role Kwon et al. (2010). Thus, the link between the winds over the NA and the GS is crucial when considering the predictability of the GS variability. Finally, although the role of the GS on the mild winters of the North-Western Europe is shown to be minor (Seager et al., 2002), the GS is yet a key component of the climatic system in the NA with the many environmental impacts described in Section 1.3.

1.5 Purpose and structure of the thesis

Given the above, the main purpose of this thesis is to quantify the recent impacts of the atmosphere on the AMOC, in particular its GS component. The prevailing winds over the NA have a direct influence on the location and intensity of the GS by the transfer of momentum between atmosphere and ocean (Taylor & Stephens, 1998; De Coëtlogon et al., 2006; Kwon et al., 2010). Empirical Orthogonal Function (EOF) analysis reveals that the North Atlantic Oscillation (NAO), closely linked to the frequency of zonal winds over the NA, is the dominant mode of variability in terms of surface atmospheric circulation over the NA (Taylor & Stephens, 1998). The atmosphere variability over the NA is thus regarded through the North Atlantic Oscillation (NAO) index. A temperature and salinity atlas in the NA is reconstructed by using the variational inverse method described in Chapter 2. From there, the GSNW and the GS intensity are computed and correlated to the NAO in Chapter 3. These correlations are used to estimate the time lags between the NAO and the GS, which are explained in Chapter 4 by the propagation of baroclinic Rossby waves across the NA.

Since another driver of the GS variability is the AMOC, the deep water formation in the Arctic and Nordic Seas also deserves consideration. In this respect, studying the recent evolution of the water masses in a sea where the formation of deep water occurs can give relevant insights. Thanks to a collaboration with the IMR (Norway)

and PINRO (Russia) institutes, we carry out a temperature and salinity atlas of the Barents Sea and use it in Chapter 5 to perform a volumetric census of its water masses. The Barents Sea shelf is a "hotspot" in the rapid climatic changes taking place in the Arctic (Lind et al., 2018). During recent decades, the Barents Sea has contributed most of the reduction in Arctic winter sea-ice cover (Yang et al., 2016). Moreover, the northern, Arctic–dominated part of the Barents Sea has experienced an "Atlantification" with profound impact on its physical conditions, such as water mass transformations and properties (Lind et al., 2018). As the northern limb of the AMOC and a source for dense Arctic Intermediate Water (Schauer et al., 1997), changes to the water mass transformation processes in the Barents Sea affect the thermohaline circulation of the North Atlantic and Arctic oceans (Swift et al., 1983; Kuhlbrodt et al., 2009; Mauritzen et al., 2013; Lozier et al., 2019).

Finally, all the results of this thesis are discussed and summarized in Chapter 6 together with the remaining open questions.

The major part of the Chapter 3 was published in Watelet et al. (2017). Most of the Chapter 4 was submitted to Ocean Science as Watelet et al. (2020a). The Chapter 5 includes the research that was published in Watelet et al. (2020b).

Chapter 2

Data analysis techniques

Contents

2.1 The gridding issue

2.1.1 A bit of history

Before the advent of computers, the only way to generate a continuous field from irregularly distributed observations was the freehand drawing by an analyst. This subjective approach was used by the weather forecasters to solve this gridding issue, for instance in the case of isobars and fronts maps. Such methods have the undeniable weakness of preventing any repeatability of the results. However, the ability of the human brain to recognize patterns and thus add some statistics in the interpolation should not be underestimated. Nowadays, the objective methods have become overwhelmingly prevalent in the Earth sciences thanks to the easy access to data analysis softwares.

Managing to solve the gridding issue is relevant in many cases, not only when trying to produce maps of a certain variable, but also to calculate volume averages, control the quality of the original data or even prepare the initial conditions of a numerical model.

2.1.2 Formulation

Mathematically, the gridding issue consists of determining the field $\varphi(\vec{r})$ for every $\vec{r}$ of a regular grid. This vector $\vec{r}$ can either be in the 2D, 3D or 4D space. The N_d measurements that are used to determine $\varphi(\vec{r})$ are arbitrarily located in $\vec{r_j}$, $j = 1, ..., N_d$. The Figure 2.1 represents this field reconstruction from data inhomogeneously distributed in space.

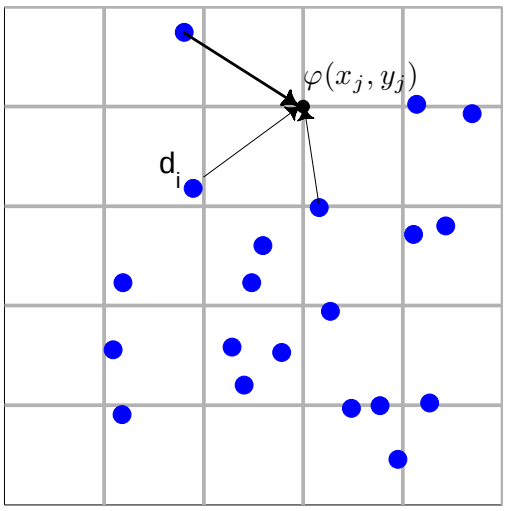

Figure 2.1: Scheme of the gridding issue from Troupin et al. (2016) showing the locations of the observations as blue dots and the nodes of the grid as the positions $\vec{r}$ where the field $\varphi(\vec{r})$ has to be calculated.

2.1.3 From interpolation to data analysis

To solve the gridding issue, the objective methods can be divided as follows: interpolation and analysis.

The former yields a reconstructed field $\varphi(\vec{r})$ that is exactly equal to the observations at their locations $\vec{r_j}$. The strict interpolation implies that these observations

are all regarded as error free, which is definitely not realistic. Besides, these methods have to deal with the issue of almost simultaneaous observations at the same locations or chose to erase of some of them. On the bright side, the interpolation methods are usually simpler to implement. Among the strict interpolation methods described in Section 2.2, we can cite the nearest neighbour, the inverse distance or the linear interpolation.

The latter allows some error on the observations, which leads to a smoother and more realistic reconstructed field. The methods using analysis requires an estimate of statistical parameters, such as the signal-to-noise ratio, in order to weight at best the observational constraints with respect to the smoothness of the field. The data analysis allows several observations at the same location.

2.2 Strict interpolation methods

2.2.1 Nearest neighbour

The nearest neighbour is the simplest interpolation method one could imagine, that is considering the closest observation as exactly equal to the reconstruted field $\varphi(\vec{r})$. This very straightforward method can be used as a first approximation in specific cases with low accuracy requirements or in case of a very dense and regular observational network. The drawbacks of this method include: discontinuities at equal distance from two observations, huge inaccuracy in case of too scarce observations, topographic bareers not taken into account, and many more.

2.2.2 Linear and Delaunay triangulation

The linear interpolation simply consists of drawing a straight line between two observations before extracting the values at the required intermediate locations. To apply such a method on a 2-dimensional domain, one cannot simply connect each pair of observations by straight lines because that would let many grid point without reconstructed field. One way to overcome this issue is to break down the domain into triangles connecting the locations of the observations following the method of Delaunay. This method uses the criterion that any circumcircle of the triangles does not include any observation. This ensures that the angles of the triangles are not too small, which would lead to sliver triangles and less realistic interpolation. Several algorithms can be used to generate such a triangulation covering the whole domain, as shown by Lee & Schachter (1980). Once the triangulation is done, the field $\varphi(\vec{r})$ can be reconstructed within each triangle by solving the plane equation:

$$ax + by + cd = h \tag{2.1}$$

where d are the observations at each tip of the triangle. Once a, b, c, h are known, the same equation is applied at each $\vec{r}(x_i, y_i)$ to find:

$$\varphi(\vec{r}) = \frac{h - ax_i - by_i}{c} \tag{2.2}$$

An example of this kind of interpolation technique is shown in Figure 2.3 by using the artificial data set with random errors shown in Figure 2.2. The discontinuities are obvious and there is no extrapolation possible since the planes only defined inside the triangles.

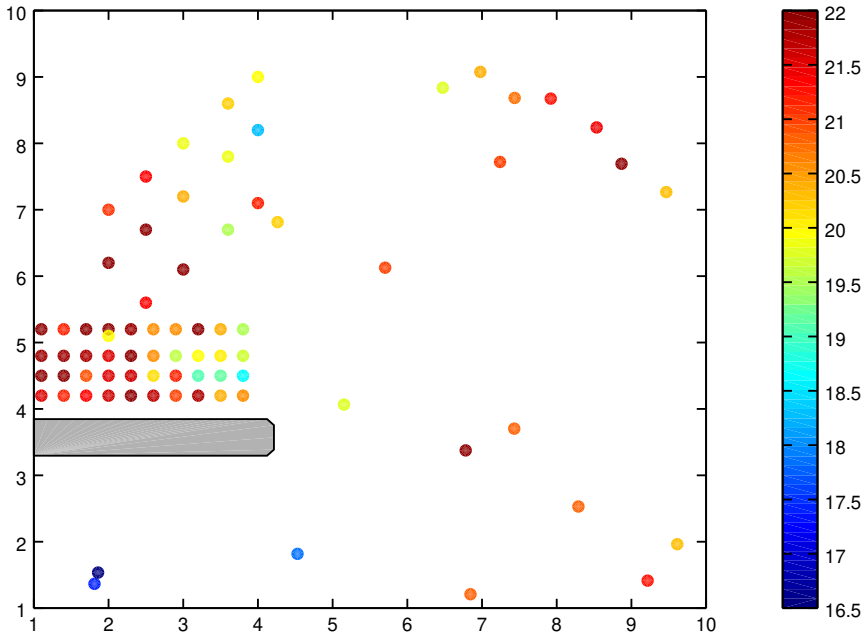

Figure 2.2: Set of artificial observations with a random error. Image courtesy of Alexander Barth.

2.2.3 Inverse distance

This type interpolation consists of weighting the observations by the distance to the location where the field is reconstructed. This yields this formulation:

$$\varphi(\vec{r}) = \begin{cases} \frac{\sum_{i=1}^{N} w_i d_i}{\sum_{i=1}^{N} w_1} & \text{if } d(\vec{r}, \vec{r_i}) \neq 0 \\ d_i & \text{otherwise} \end{cases} \tag{2.3}$$

where d is the distance. The weights are defined as follows:

$$w_i = \frac{1}{d(\vec{r}, \vec{r_i})} \tag{2.4}$$

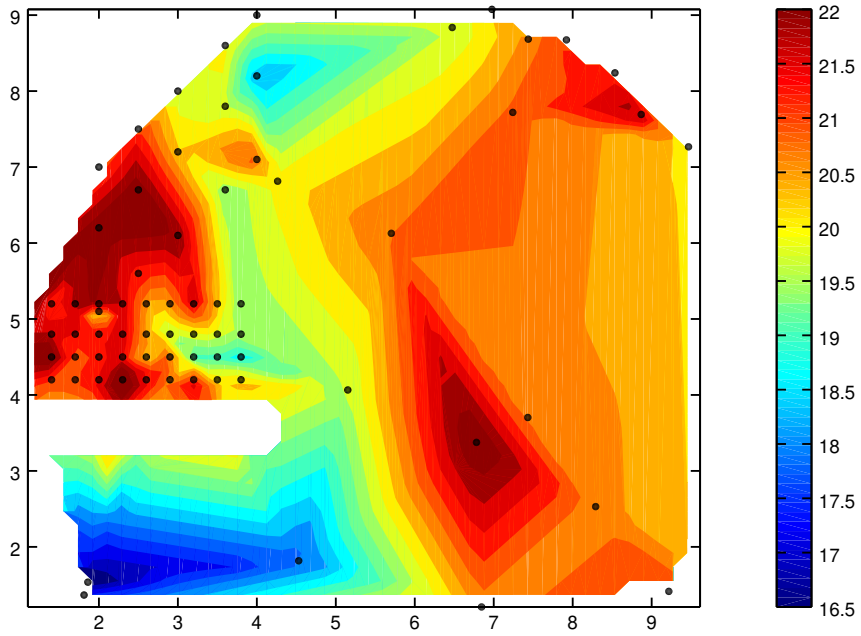

Figure 2.3: Linear interpolation of the data set shown in Figure 2.2 after a Delaunay triangulation. Image courtesy of Alexander Barth.

2.2.4 Polynomial

A data set can be interpolated by a polynomial as long as it is relatively smooth. When gradients are large, the order of the polynomial must be increased and the use of several local polynomials is preferred. It is possible to use a fitting method such as the weighted least squares to avoid overfitting. In this case, the interpolation is best refered to as an analysis.

2.2.5 Spline

A spline is actually a function defined piecewise as a ensemble of polynomials. In the 1D case, each observation is called a node, and a polynomial is defined between each node. To ensure a minimum bending while passing by all nodes, the first and second derivatives of each of the neighbouring polynomials of a node have to be equal. The spline interpolation avoids the Runge's phenomenon that occurs when using the polynomial interpolation at high degree, that is an oscillation close to the domain's edges.

2.2.6 Natural neighbours

The natural neighbours interpolation is based on the Voronoï tessalation. This tessalation is performed by defining the polygons including all the grid points that are closer to a particular observation than any other one. Each observation is thus

surrounded by a polygon of variable "influence" depending on the direction. From this domain decomposed into polygons, the idea of the natural neighbours interpolation is to choose a location where the field has to be reconstructed, define a new Voronoï polygon around this point, and use the intersecting surface with each of the previous polygons to define the weights to be used for each surrounding observation in the following recontruction of the field:

$$\varphi(\vec{r}) = \sum_{i=1}^{N_p} w_i d_i \tag{2.5}$$

where N_p is the number of polygons associated with the natural neighbours of the desired location. The larger the intersecting surface, the higher the weight, with several formulations possible.

2.3 Advanced data analysis techniques

2.3.1 Kriging

We describe here the ordinary kriging as detailed by Hartman & Hössjer (2008). The observations can be decomposed as follows:

$$d_i = \mu + \gamma_i + \epsilon_i \tag{2.6}$$

where μ is the mean value of the field, γ_i is the anomaly with respect to the mean and ϵ_i is the error on the observation. From there, the reconstructed field is a linear combination of the data with weights computed for the whole data set, unlike the Equation 2.5:

$$\begin{cases} \varphi(\vec{r}) = \sum_{i=1}^{N} w_i d_i = \vec{w}^t \vec{d} \\ \sum_{i=1}^{N} w_i = 1 \end{cases} \tag{2.7}$$

where the condition on the weights is set in order for the estimator to be unbiased. Let us define the observational covariance matrix as $\mathbf{D}$ and the vector $\vec{\omega}$ as the covariances between $\mathbf{D}$ and the field $\varphi(\vec{r})$ at en arbitrary location. By minimizing the mean square estimator error, one can find the weights:

$$\vec{w} = \mathbf{D}^{-1} \left(\vec{\omega} + \vec{1}_n \frac{1 - \vec{1}_n^t \mathbf{D}^{-1} \vec{\omega}}{\vec{1}_n^t \mathbf{D}^{-1} \vec{1}_n} \right) \tag{2.8}$$

where $\vec{1}_n$ is a unit vector of size n. The error variance of the estimator can also be computed, see Hartman & Hössjer (2008). For the covariance function of the kriging

method, most applications use an exponential, spherical, Gaussian, pure nugget, or a linear combination of these functions.

2.3.2 Optimal Interpolation (OI)

The OI is a method equivalent to Kriging, but with a different formulation. The mathematical criterion used by the OI is also the minimization of the expected error between the analyzed field and the true field, which is unknown. The field $\varphi(\vec{r})$ can be decomposed as the sum of a background field φ_b and an anomaly φ':

$$\varphi(\vec{r}) = \varphi_b(\vec{r}) + \varphi'(\vec{r}). \tag{2.9}$$

The data anomalies relative to the background are also considered from here. This background field is based on a priori knowledge and can be defined for instance by a climatological average, a linear regression, or a theoretical solution.

Similarly to the Equation 2.7, the field anomaly φ' is a linear combination of the data. Minimizing the expected error variance of the analyzed field yields:

$$\varphi(\vec{r}) = \vec{c}^t(\mathbf{B} + \mathbf{R})^{-1}\vec{d} \tag{2.10}$$

where $\vec{c}$ contains the covariances between the analysis location and all data points, $\mathbf{B}$ is the background covariance matrix and $\mathbf{R}$ the data error covariance matrix. Both matrices have the size $N_d * N_d$. The asociated error on the analysis is expressed as:

$$\epsilon_a = \sigma^2 - \vec{c}^t(\mathbf{B} + \mathbf{R})^{-1}\vec{c} \tag{2.11}$$

where σ^2 stands for the field variance.

A typical issue is to specify the covariances in $\vec{c}$ and $\mathbf{B}$. In rare cases, the covariances can be based on a priori knowledge, but otherwise they have to be determined by computing statistics on the data. In the standard OI, a choice has to be made on the shape of a covariance function f between locations. Usually, a function $f(r/L)$ is used, where r is the distance between locations and L is called the correlation length. Similarly to Kriging, several functions can be chosen, for instance a Gaussian. As we shall see, the covariances can also be derived from the use of functionals when using Variational Inverse Methods (VIM), see Section 2.3.3.

2.3.3 Variational Inverse Method (VIM)

The variational inverse method implemented in the software DIVA relies on the minimization of the following functional:

$$J[\varphi] = \sum_{i=1}^{N} \mu_i \left[d_i - \varphi(x_i, y_i)\right]^2 + \int_D \left(\nabla\nabla\varphi : \nabla\nabla\varphi + \alpha_1 \nabla\varphi \cdot \nabla\varphi + \alpha_0 \varphi^2\right) dD \quad (2.12)$$

The first term minimizes the difference between the data and the analysis, which is balanced by a regularization of the field in the second term. The equation 2.12 can be made non-dimensional by using the following variable changes: $\tilde{\nabla} = L\nabla$ and $D = L^2\tilde{D}$:

$$\tilde{J}[\varphi] = \sum_{i=1}^{N} \mu_i L^2 \left[d_i - \varphi(x_i, y_i)\right]^2 + \int_{\tilde{D}} \left(\tilde{\nabla}\tilde{\nabla}\varphi : \tilde{\nabla}\tilde{\nabla}\varphi + \alpha_1 L^2 \tilde{\nabla}\varphi \cdot \tilde{\nabla}\varphi + \alpha_0 L^4 \varphi^2\right) d\tilde{D} \quad (2.13)$$

In variational methods, the correlation function is not explicitely defined a priori. Here, the correlations are subsequent to the shape of the differential equation in Equation 2.13. One can show that the following specifications of the parameters

$$\begin{cases} \alpha_0 L^4 = 1 \\ \alpha_1 L^2 = 2 \\ \mu L^2 = 4\pi \frac{\sigma^2}{\epsilon^2} \end{cases} \quad (2.14)$$

lead to a correlation function that has this specific form, provided an infinite domain is assumed:

$$C(r) = \frac{r}{L} K_1 \left(\frac{r}{L}\right) \quad (2.15)$$

where K_1 is the modified Bessel function. In Equation 2.14, $\frac{\sigma^2}{\epsilon^2}$ is the Signal to Noise Ratio (SNR). Once these choices on the form of the functional have been made, two important parameters need to be decided: the correlation length L and the SNR. The former measures the typical length of influence of the data while the latter can be seen as how reliable the data is. L is estimated through a least-square fit of the data correlations as a function of distance to the theoretical correlation function (Equation 2.15). An estimate of the SNR can be obtained by using generalized cross validation techniques.

2.4 Comparison of Kriging, OI and VIM

2.4.1 Mathematical equivalence

As mentioned above, Kriging and OI only differ by their mathematical formulation, that is how the mean is specified, but the results are the same. The VIM and the

OI also give very similar results, provided the covariances of the OI are consistent with the kernel of the VIM implemented in DIVA. Rixen et al. (2000) also showed this equivalence through a practical interpolation case comparing the fields resulting from OI and VIM.

2.4.2 Advantages of VIM

Throughout the research presented in this thesis, we use the VIM implemented in the software DIVA. This method is used to generate the atlas of temperature and salinity in both the NA and the Barents Sea.

Physical aspects

Against subjective methods, the VIM as the obvious advantage of being fully reproducible given the analysis process is fully documented. The human a priori knowledge can also be used in the VIM, but in a much more formal way, including a priori knowledge of the background field and covariances. Given the wide range of objective methods directly accessible nowadays, the subjective methods have become immaterial.

VIM brings many advantages in comparison to strict interpolation methods. First of all, VIM takes into account the error on data, which not only includes the observational error but also the fact that an exact measurement might not necessarily be representative of the field to be reconstruted. Secondly, the reconstructed field is smoother using the VIM, unkike several strict interpolation methods that produce discontinuities in the field. Finally, the extrapolation is also possible in VIM.

Kriging and OI are among the most advanced analysis techniques, similarly to VIM. However, thanks to the mathematical formulation of the VIM, it is easier to take into account physical barreers such as islands or peninsula. The OI also requires the inversion of a $N_d * N_d$ matrix, making the number of operations proportional to N_d^3 for each analysis. In the VIM implemented in DIVA, the computation time is proportional to $N_a^{5/2}$ where N_a is the amount of grid points where the analysis is performed. Finally, the OI is not fully objective in the sense that it requires the explicit choice of the covariance functions while the VIM only requires the specification of a few parameters: VIM kernel class of Bessel function controlled by α_0, α_1, α_2, type of functions. In DIVA, a part of these parameters are chosen after performing statistics on the data set, see Section 2.3.3.

Technical aspects

In the forthcoming table, we compare the standards and the methods used by 11 recent popular gridding softwares designed to perform analysis and/or visualisation of ocean data. Regarding the gridding techniques or the specification of the covariances, these softwares are clearly not aiming to the same purposes. Some of them mostly focus on the quick visualisation of NetCDF files with a minimal support for interpolation (Panoply, Ferret,...), while others offer a wide range of advanced possibilities to analyse the data.

The documentation is not always very clear or even available, so this comparison still suffers from limitations, especially on the compliance with OGC standards which is not specified in most cases. One of the critical point towards any harmonisation between these softwares is probably the input and output file formats. Although most of these software can work with simple text files, their conventions are not standardized. The netCDF format is widely used in the ocean community, so that is a good thing the majority can deal with them (import/export), although some potential remains for a generalized use of the version 4. Already 8 softwares can also import these netCDF files via OPeNDAP. Considering the other formats, there is a broad range from proprietary formats such as shapefile to common images such as png. Several softwares also developed their own customized format. The majority of softwares are already multi-platform and allow the scripting or the implementation of an API.

While 8 softwares are open-source and distributed for free, 3 of them are proprietary and profitable. Although there is a free open-source alternative for IDL and arcGIS, it seems there is no direct alternative for SURFER.

Gridding tools	**IDL**	**ODV**	**IDV**	**(arc)GIS**	**DIVA**	**divand**	**diva-on-web**	**SURFER**	**Ferret**	**GNU R**	**Panoply**
Gridding techniques	Nearest neighbour, inverse distance, bilinear, polynomial, spline, natural neighbours, kriging	Inverse distance, Variational Inverse Method (VIM)	Inverse distance	Inverse distance, polynomial, spline, natural neighbours, kriging	Variational Inverse Method	Variational Inverse Method	Variational Inverse Method	Nearest neighbourg, moving average, linear, inverse distance, radial basis function, (local) polynomial, natural neighbours, minimum curvature, Modified Shepard's Method, kriging	Nearest neighbour, moving average, linear	Inverse distance, moving average, linear, spline, kriging	Linear
Knowledge of covariances	Kriging: choice between 4 covariance functions	VIM: covariances implicitely chosen by the shape of the norm	A priori	Kriging: choice between 5 variogram models	VIM: covariances implicitely chosen by the shape of the norm	VIM: covariances implicitely chosen by the shape of the norm	VIM: covariances implicitely chosen by the shape of the norm	Kriging: choice between 10 variogram models or a combination of each	A priori	Kriging: choice between 3 variogram models	A priori
Error estimation	No	Yes	No	No	Yes	Yes	Yes	No (only RMSE with respect to the data)	No	No	No
Interpolation or analysis?	Interpolation / Analysis	Interpolation / Analysis	Interpolation	Interpolation / Analysis	Analysis	Analysis	Analysis	Interpolation / Analysis	Interpolation	Interpolation / Analysis	Interpolation

Multivariate analysis	No	No	No	Yes (cokriging)	Yes	Yes	No	No	No	Yes	No
Scripting / API	Yes	Yes (API for C++ and Java)	Yes	Yes	Yes	Yes	Yes	Yes	Yes	Yes	Yes (beta)
Physical constraints	No	Coastlines, advection along isopycnals	No	No	Coastlines, advection fields, ocean bottom	Coastlines, advection fields	Coastlines, advection fields	No	No	No	No
Maximum dimensions	2D (3D if inverse distance)	2D	2D	2D	2D, pseudo-3D, pseudo-4D	nD	2D	2D	4D	2D	2D
Gridding tools	**IDL**	**ODV**	**IDV**	**(arc)GIS**	**DIVA**	**divand**	**diva-on-web**	**SURFER**	**Ferret**	**GNU R**	**Panoply**
Handling of anisotropy	Ellipse defining a line of equal influence	Advection along isopycnals	No specific feature	Covariance modeling along each direction	Variable correlation length field, advection fields	Advection fields	Advection fields	Angle of preferred direction	No specific feature	Angle of preferred direction	No specific feature
Input file format	Text, netCDF4 (OPeN-DAP)	Text, ODV4, netCDF (OPeN-DAP)	Text, GRIB, ESRI, netCDF (OPeN-DAP),...	Text, ArcGIS, ESRI, raster, shapefile, netCDF4 (OPeN-DAP),...	Text, ODV4	Text, netCDF4 (OPeN-DAP)	Text, ODV4	Text, netCDF, AutoCAD DXF, Excel, SRTM HGT,...	Text, netCDF4 (OPeN-DAP)	Text, Excel, .csv, netCDF4 (OPeN-DAP)	NetCDF4 (OPeN-DAP)
Output file format	Text, netCDF4	Text, ODV4, netCDF	JPEG and PNG images	ESRI, ERDAS, .tiff, images, netCDF4	GHER binary, text, netCDF	Text, netCDF4	netCDF, .mat, .kml, images	Text (.grd), images, MIF/MID, SHP/DBF, .klm, .svg, netCDF,...	Text, images, netCDF4	Text, images, Excel, netCDF4	Images (.png, .tiff, .gif,...)

OGC compliance	Yes ?	?	No ?	Yes	?	?	Yes	?	?	?	No ?
Sharing policy and/or license	Profitable, proprietary	Free, open-source, license here: https://odv.awi.de/software/register/terms/	Free, open-source, GNU LGPL	Profitable, proprietary, license here: https://developers.arcgis.com/terms/	Free, open-source, GNU GPL	Free, open-source, GNU GPL	Free, open-source, GNU GPL	Profitable, proprietary, license here: http://www.goldensoftware.com/terms-of-use	Free, open-source, license here: http://ferret.pmel.noaa.gov/Ferret/downloads/ferret-legal	Free, open-source, GNU GPL	Free, open-source, license here: https://gcmd.nasa.gov/records/NASA_GISS_Panoply.html
Operating system	GNU/Linux, macOS, Windows	GNU/Linux, macOS, Windows	GNU/Linux, macOS, Windows	Windows	GNU/Linux, macOS, Windows	GNU/Linux, macOS, Windows	GNU/Linux, macOS, Windows	Windows	GNU/Linux, macOS, Windows	GNU/Linux, macOS, Windows	GNU/Linux, macOS, Windows
Comments	GDL is a free open-source clone of IDL	ODV includes an implementaion of DIVA		QGIS is a free open-source alternative		Divand is a package on Octave/Matlab & Julia	Diva-on-web is a web application implementing basic DIVA features				

Glossary of the table

- Analysis: while the interpolation implies an exact passage of the reconstructed field through the data, the analysis takes into account the observational and representativity errors, which allows the solution to be somewhat different than the original values.

- Kriging: this gridding method is based on the study of the empirical variogram computed from the original data. The idea of the variogram is to explicit the spatial variation of the data as a function of the distance, and fit this function by a theoretical model (spherical, exponetial, gaussian,..) with specific parameters. This model defines the covariances to be used in the analysis.

- Optimal Interpolation (OI): the OI aims to minimize the error variance of the analysis with respect to the true field, in order to get the BLUE (Best Linear Unbiased Estimator) as a solution. It also provides an error field associated with the analysis. Similarily to the kriging, the OI requires the choice of the covariance function.

- Variational Inverse Method (VIM): the VIM, first implemented in DIVA, is a gridding technique based on the minimisation of a cost function. This cost function contains a term accounting for the misfits between the data and the analysis, while the second term (the "norm") penalizes the anomalies with respect to a first guess as well as the strong variations. The problem is solved efficiently on a finite-element grid. Although the choice of the formulation of the norm implicitely defines the covariances used in the analysis, the VIM has some practical advantages with respect to kriging and OI: it is cost-efficient (no need to invert a huge covariance matrix) and it easily deals with physical constraints (topographic barriers, advection fields).

Important: Although using different implementations and mathematical formulations, kriging, OI and VIM are all equivalent methods under some assumptions on the covariances.

Chapter 3

Gulf Stream indices and correlation with the North Atlantic Oscillation

Contents

Preliminary remark

The major part of this Chapter was published in Watelet, Beckers & Barth (2017). Most of the additional information is emphasised by coloured boxes.

3.1 Introduction

The western boundary current of the North Atlantic Ocean, the Gulf Stream (GS), transports approximately 31 Sv of water and 1.3×10^{15} W of heat along the east coast of Florida (e.g. Lund et al., 2006). This intense northward transport of energy continues as far as the Cape Hatteras where the GS leaves the continental margin. Close to the cape, the GS transport is estimated at 94.5 Sv by Rossby et al. (2014). It then veers in a northeastward direction passing the longitude of the Grand Banks (150 Sv at that point according to Hogg (1992)) towards the longitude of the southern tip of Greenland (Chaudhuri et al., 2009). The GS then becomes the North Atlantic drift, heading towards Scandinavia. Prevailing winds over the North Atlantic (NA) have a direct influence on the location and intensity of the GS by the transfer of momentum between atmosphere and ocean (Taylor & Stephens, 1998; De Coëtlogon et al., 2006; Kwon et al., 2010). Therefore, the study of interannual variability of the GS requires the identification of sources of variability within the atmospheric circulation. Empirical Orthogonal Function (EOF) analysis reveals that the North Atlantic Oscillation (NAO), closely linked to the frequency of zonal winds over the NA, is the dominant mode of variability in terms of surface atmospheric circulation over the NA (Taylor & Stephens, 1998). It explains 36% of the variance of the winter surface pressure over the period 1899–1994 and the zone 20–80°N, 90°O – 40°E (Hurrell, 1995).

Various studies have highlighted the impact of the NAO on the variability of the GS position. Taylor & Stephens (1998) computed a GS North Wall (GSNW) index based on monthly charts of the north wall of the GS published by the US Naval Oceanographic Office in "Gulf Stream Monthly Summary" from 1966 to 1974, by the US NOAA in "Gulf Stream" from 1975 to 1980, and in "Oceanographic Monthly Summary" from 1981 to 1994 (Taylor & Stephens, 1998). These charts were drawn using in situ, aircraft and satellite observations, while the north wall was located by analysis of sea surface semperature (SST) gradients or the location of the 15 °C isotherm at 200 m (National Oceanic and Atmospheric Administration, 1977). Taylor along with various collaborators derived the GSNW from these charts for 6 longitudes following the procedure described in Taylor & Stephens (1980), Taylor et al. (1992) and Taylor (1995). Their GSNW index is then computed via an EOF analysis. Using more charts from the NOAA (up to three times per week) over the period 1973–1992, Drinkwater et al. (1994) analysed the GSNW at 26 longitudes between 75°W and 50°W. Here also, the criterion used by the NOAA to draw the GSNW on the charts is the maximum SST gradient or the 15 °C isotherm at 200 m. Gangopadhyay et al. (1992) reconstructed a time series of the latitude of the GS separation from the coast using charts from the NOAA between 1977 and 1988. Joyce et al. (2000) constructed a GSNW index with data from the Levitus & Boyer (1994) atlas over the period 1954–1989. Following Fuglister (1955, 1963) and Halkin & Rossby (1985), they used the 15 °C isotherm at 200 m as a convenient marker for the northern wall of the GS. An EOF analysis was then performed using the GSNW at 9 selected longitudes between 75°W and 50°W, the first mode being their GSNW index.

Furthermore, other methods to derive the GS position which are not focused

on the GSNW have been developed. For instance, Kelly & Gille (1990) used the maximum gradient of the sea surface height (SSH) from the Geosat altimeter to compute the position of the centre of the GS at 69°W between 1986–1989. This technique was also used by Peña-Molino & Joyce (2008) for the period 1993–2007, with SSH data originating from the TOPEX-Poseidon and Jason satellites. Pérez-Hernández & Joyce (2014) computed a GS position index based on the position of the maximum variability of the sea level anomaly (SLA) at 16 longitudes between 75°W and 45°W. These SLA satellite data were acquired from the AVISO data centre over the period 1992–2012. Finally, Sasaki & Schneider (2011) used the OFES model and satellite and subsurface observations to determine the latitude of the GS jet axis. They used the SSH monthly outputs at -20 cm, -15 cm, and -10 cm from OFES, the 17 °C isotherm of annual mean temperature at 200 m (following Frankignoul et al. (2001)), and the -10 cm contours from monthly satellite data. An EOF analysis between 75°W and 55°W was then conducted to determine the GS position index from 1960 to 2003.

Taylor & Stephens (1998) compared a NAO index (based on the winter pressure difference between Lisbon, Portugal and Stykkisholmur, Iceland) with their GS position index over the period 1966–1996. Their results show a strong correlation between both indices, with a time lag of two years. Two years after a winter characterized by strong zonal winds, the GS takes a more northern position, and conversely for negative winter NAO phases. Sasaki & Schneider (2011) obtained similar results using a near-global model with high spatial resolution. Chaudhuri et al. (2009, 2011) also showed a more northern position of the GS during positive NAO phases however, since they only used 2 periods (1958–1971 and 1980–1993) in which both NAO and GS path were averaged, no time lag was detected between a specific NAO phase and its impact on GS position. Finally, Pérez-Hernández & Joyce (2014) estimate this time lag at one year, while Joyce et al. (2000) obtained the same significant NAO-GS correlations for time lags of 0 and 1 year. Joyce et al. (2000) explain the discrepancy in lag time with Taylor & Stephens (1998) by citing the different periods that were used. Therefore, they updated their index to 1998 and used both 1966–1998 and 1975–1998 periods to compare with Taylor's indices. Over the shorter period, both GS indices exhibit time lags of 1 year with the NAO, while the longer period is still affected by different time lags. Some peculiarities in the GS north wall charts over the initial years are invoked by Joyce et al. (2000) to account for this. We discuss in Section 3.2 the reason why these GS charts should be considered with care.

In the present study, we focus on two different aspects of the GS: in addition to its position, another feature of interest is its transport. The vast majority of previous studies find a positive correlation between the NAO and the GS transport, although the methods and their limitations are very different. Sato & Rossby (1995) used 130 hydrographic stations along the GS path and observed a decrease of 6 Sv in the GS transport between the end of the 1950s and the beginning of the 1970s, a period over which the NAO was also declining, although no comparison is presented. Curry & McCartney (2001) estimated the GS transport through an index based on the difference of eddy kinetic energy anomaly between the centers of the subpolar and subtropical gyres. The calculation is based on only 2 hydrographic stations

from both zones and is representative of the eastward mass transport between these two gyre centers over the first 2000 meter depth. Their results show a weakening of the GS during the 1960s followed by a persistent strengthening between 1970 and 1995, consistent with the evolution of the NAO. More recently, De Coëtlogon et al. (2006) gave support to this link between the NAO and the GS transport using outputs from five OGCMs. These simulations, that starts in 1948, show the NAO leading the GS transport by 0–2 years, and also indicate an influence from the Atlantic Meridional Overturning Circulation (AMOC). Nevertheless, these OGCMs are not able to accurately represent GS meanders because of a number of approximations, e.g. their limited spatio-temporal resolution (in general, the spatial step is higher than 1°) so that they do not resolve mesoscale eddies. For these reasons, these OGCMs are not able to represent strong enough thermal gradients, leading them to strongly underestimate the GS transport. Furthermore, the GS path does not separate from the coast at Cape Hatteras in non-eddy-resolving models (De Coëtlogon et al., 2006). On the contrary, Penduff et al. (2004) performed a simulation at higher spatial resolution (1/6°) of the eddy kinetic energy (EKE) on a smaller domain limited to the Atlantic basin. Their results show that the EKE field varies in correlation with the NAO only when the NAO changes are strong, and with a delay varying between 0 and 12 months. Although limited to a shorter period (1979–2000) than the De Coëtlogon et al. (2006) work, this study also showed a stronger (and more northward) GS during positive NAO phases.

While the aforementioned studies indicate positive correlations between the NAO index and GS transport, the study by Gangopadhyay et al. (1992) suggests the contrary, i.e., a weaker GS transport during NAO positive phases. Finally, Chaudhuri et al. (2011) used a regional oceanic model with a spatial resolution of 1/6° to model the GS transport. Their simulations show, during negative NAO phases, an augmentation of the transport upstream of Cape Hatteras and a decrease of the transport downstream of the cape.

This currently limited understanding of the links between the NAO and the GS, as well as several limitations in past reconstructions of GS characteristics (see also Section 3.2), impels us to reduce errors in the spatial and temporal distribution of the GS. Our main purpose in this study is to build enhanced indices of GS position and transport based on an objective method that minimises errors (DIVA), over a longer period (1940–2014) and using a much larger in situ dataset made up of 5 different databases. To this end, we reconstruct spatially continuous fields of ocean (sub)surface temperature and salinity in the NA from these in situ time series, for every month since 1940. From these GS indices we are able to compute the correlations between the current and the NAO. Finally, we examine the time lag between the NAO and GS in the light of interaction with planetary waves.

3.2 Data and methods

The bulk of the literature contains at least one of these main drawbacks: short time series, poor data coverage or low spatial resolution. Further, several studies are based on subjective GS charts. In this Section, we explain how we addressed these issues to achieve a more robust calculation of the GS indices.

We used the DIVA (Data-Interpolating Variational Analysis) tool, which is a numerical implementation of the variational inverse method (VIM) using the finite elements method to reconstruct continuous fields from discrete measurements (Troupin et al., 2012). This VIM consists of selecting the best fit among the functions analysing the data. For this purpose, we use as a selection criterion a global calculation of analysis quality by minimizing the following cost function J (Brasseur, 1995; Troupin et al., 2012):

$$J[\varphi] = \sum_{j=1}^{Nd} \mu_j \left[d_j - \varphi(x_j, y_j)\right]^2 + ||\varphi||^2 \tag{3.1}$$

with

$$||\varphi||^2 = \int_D (\alpha_2 \nabla\nabla\varphi : \nabla\nabla\varphi + \alpha_1 \nabla\varphi.\nabla\varphi + \alpha_0 \varphi^2) dD \tag{3.2}$$

where α_0 penalizes the field itself (anomalies with respect to a background field, e.g., a climatological average), α_1 penalizes gradients (no trends), α_2 penalizes variability (regularization), and μ_j penalizes data-analysis misfits (objective analysis) (Troupin et al., 2015). Given the nature of the method, it thus requires a higher density of observations to model the local value of a strong gradient than estimating the amplitude of the variation on a larger scale. Besides, it is even easier to just detect the position of such a gradient.

The VIM gives equivalent results to those from optimal interpolation (OI) if covariances are chosen accordingly (Rixen et al., 2000); these are hidden in DIVA via the coefficients α and μ that define a correlation length scale and a signal-to-noise ratio as in OI. VIM, as well as OI, are both considered as objective methods, in the sense that a given set of inputs always produces the same particular output (see Wilks (2011)). On the contrary, subjective methods require a priori knowledge or a decision by the analyst, that conflicts with repeatability.

This study uses hydrographic data (temperature and salinity) going back to the early twentieth century from the following databases: WOD (World Ocean Database, NOAA), SeaDataNet, ICES (International Council for the Exploration of the Sea), Hydrobase3 and ARGO floats. These discrete measurements are all non-gridded and non-interpolated data, in order to work with the original data from each database. The profiles are vertically interpolated onto 15 horizontal levels from 0 to 3000 m depth. Exact duplicates were removed from the data sets, while near duplicates (considering space and time) were passed through a specific algorithm that removed the vast majority of those cases. The detection of the near duplicates used the following thresholds: 0.1°for longitude and latitude, 1h for time, at each depth layer. If two near measurements are below all these thresholds, the value of the variable is averaged. Further, the weight of this average in the analysis is reduced when the difference between both near duplicates is higher than 0.1°C or 0.1 PSU. The relative importances of each database in terms of data quantity as well as the total numbers of duplicates are given in Table 3.1, the predominant database

being the WOD for both temperature and salinity. Considering the temporal coverage of these databases, we show data abundance at the surface since 1900 in Figure 3.1. The graph clearly shows the large increase of measurement campaigns over the Atlantic after 1940. Both world wars also impact the data abundance. The large decrease of data in 2015 can be explained by the time required by data centers to process and make them available in their public databases, which leads to an absence of data in November and December 2015. We subsequently decided not to use this entire year to avoid a seasonal bias in our GS reconstruction.

Variable	Database	Number of observations	Total	Number of duplicates	Total without duplicates
Temperature	WOD	24 234 836	40 737 763	13 695 754	27 042 009
	SeaDataNet	3 778 937			
	ICES	5 810 552			
	Hydrobase3	3 962 613			
	ARGO	2 950 825			
Salinity	WOD	13 468 105	28 363 948	12 560 338	15 803 610
	SeaDataNet	2 546 423			
	ICES	5 592 437			
	Hydrobase3	3 962 613			
	ARGO	2 794 370			

Table 3.1: Numbers of observations considered for each database after vertical interpolation to 15 layers (column 1) and total numbers of observations before (column 2) and after duplicate removal (column 4). The total number of duplicates is given in column 3, representing 34% (temperature) and 44% (salinity) from the original data sets.

The accuracy of each type of instrument (CTD, XBT,...) was also taken into account when attributing the relative weights μ_j to observations. Using in particular the WOD documentation of Boyer et al. (2013) on data accuracy, as well as technical reports from the other databases, we decided to apply a weight factor of two between APB, XBT, MBT measurements and other data sources which are more reliable, such as CTDs. The signal-to-noise ratio and the correlation length were optimized for each of the 15 horizontal layers and filtered vertically to avoid unrealistic discontinuities. The filtering of the correlation length is detailed in Appendix 3.A.

For each layer, an analysis has been performed for each month since January 1900 on the domain shown in Figure 3.2 and covering the NA. A relative error field associated with each analysis was also computed by the poor man's error method (Brasseur, 1995).

We also used an annual NAO index based on an EOF analysis of the sea level pressure (SLP) anomalies over the Atlantic (20°–80°N, 90°W-40°E). This index is less noisy than the station-based one and uses all the spatial patterns over the Atlantic, not only 2 meteorological stations. This index is available at https://climatedataguide.ucar.edu/climate-data/hurrell-north-atlantic-oscillation-nao-index-pc-based and more details are given in Hurrell (1995), Hurrell et al. (2003), Hurrell & Deser (2010) and Trenberth & Hurrell (1999).

At this point, we can compare our method to generate temperature and salinity fields (the basis for the computation of GS indices, see Sections 3.3 and following) with past studies considering the evolution of GS characteristics. In Table 3.2,

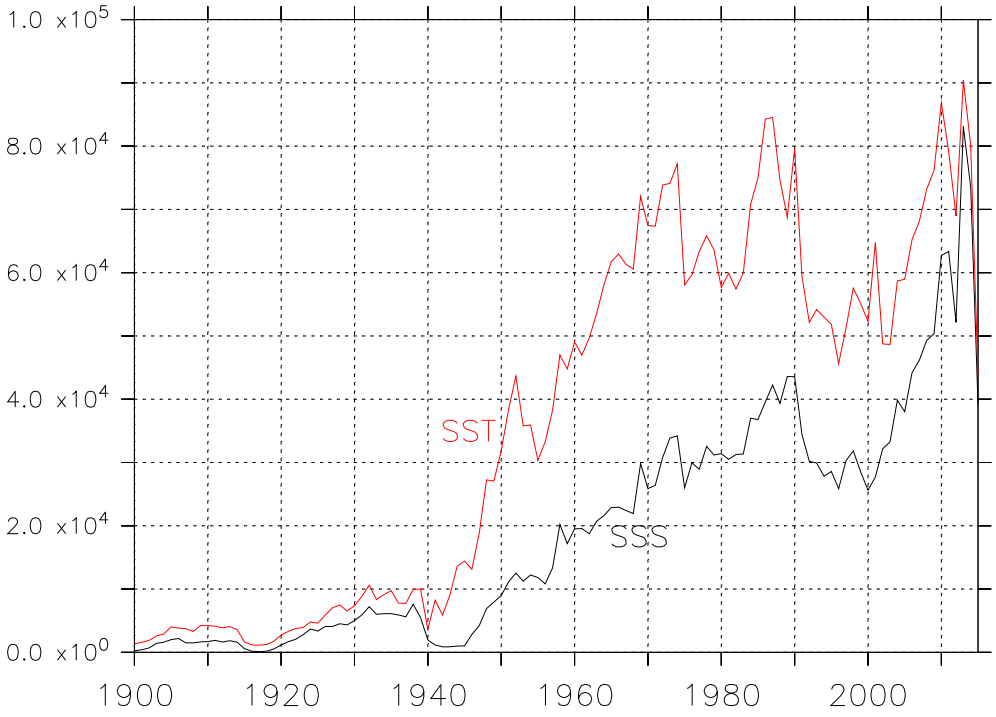

Figure 3.1: Numbers of temperature (red) and salinity (black) surface observations, compiled from our 5 databases (WOD, SeaDataNet, ICES, Hydrobase3, ARGO) for each year between 1900 and 2015, after removal of duplicates.

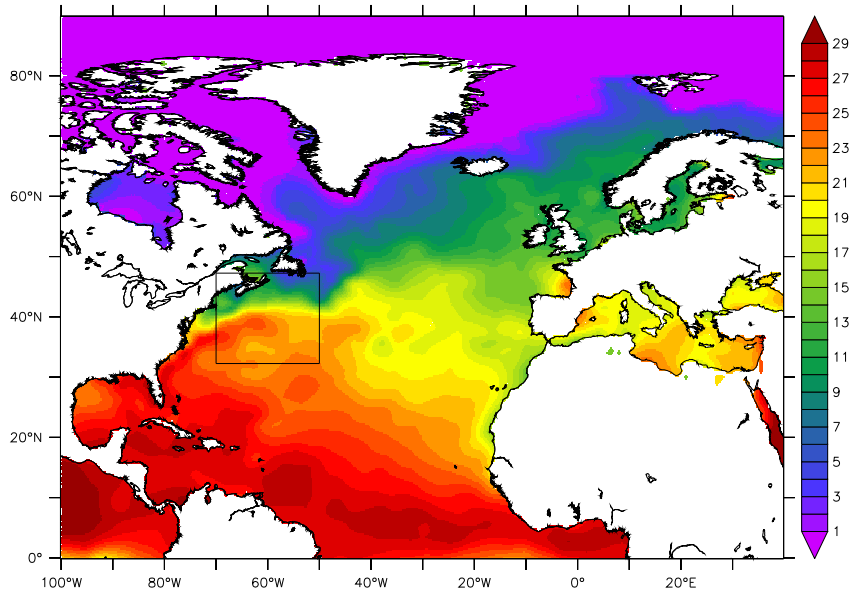

Figure 3.2: Our SST (°C) product in June 1984 on large and small domains where analysis and detection of the GS position, respectively, were carried out.

we summarise these 15 studies according to their method and limitations. Three of them (Fuglister, 1963; Drinkwater et al., 1994; Taylor & Stephens, 1998) used methods based on GS charts drawn subjectively by analysts. It remains unclear whether and when the GS was located by SST gradients or the 15 °C isotherm at 200 m. Five authors (Fuglister, 1963; Halkin & Rossby, 1985; Kelly & Gille, 1990; Gangopadhyay et al., 1992; Frankignoul et al., 2001) focused on periods of 10 years or less, while only five (Sato & Rossby, 1995; Joyce et al., 2000; Curry & McCartney, 2001; De Coëtlogon et al., 2006; Sasaki & Schneider, 2011) extended their GS index to 30 years at least. Among them, Sato & Rossby (1995) used a limited set of 130 hydrographic stations, Joyce et al. (2000) based their work on the Levitus & Boyer (1994) atlas at a low spatial resolution (1°x 1°), Curry & McCartney (2001) only used one station at the center of both the subtropical and subpolar gyres, and De Coëtlogon et al. (2006) and Sasaki & Schneider (2011) used rather low resolution ($\geq$0.5°) models. Considering this, the present study can be seen as the first attempt to build GS indices on a very long period (75 years) based on a fully objective method (DIVA) by using the largest set of in situ data by far (more than 40 millions entries (see Table 3.1)). This unique data set is made up of a combination of 5 well-known databases. In addition, owing to the high resolution of our maps (0.25°x 0.25°), we were able to build our GS indices over a much denser array of meridional transects between 70°W and 50°W: this makes our indices less sensitive to noise. The use of gradients rather than thresholds also makes the GS detection more realistic. Finally, our GS indices come with error bars computed from the error fields on the analyses.

Note 3.1: Comparison against ERA-20C

In order to strengthen the confidence in our DIVA analyses, we compared them with the realanyses ERA-20C (see Poli et al. (2016)). These pilot reanalyses cover the time period 1900–2010. The assimilation scheme is based on surface observations of pressure and marine winds only. The spatial resolution is about 125 km while the output is gridded every 1°. The DIVA analyses described above are given on an output grid of 0.25° and are thus interpolated on the same grid as ERA-20C through a weighted average. Figure 3.3 shows an example comparing both DIVA analyses and ERA-20C before the interpolation on the same grid.

Authors	Period	Domain	GS characteristics	Main method / data source	Objectivity	Spatio-temporal resolution	Correlation coefficient with NAO
Fuglister (1963)	1960	71–48° W	position	1 analyst GS map	no	(1 snapshot)	/
Halkin & Rossby (1985)	1980–1983	73° W	transport	1 currentmeter	yes	1 lon, bi-monthly	/
Kelly & Gille (1990)	1986–1989	69° W	position & transport	Geosat altimeter	yes	1 lon, ev. 17 days	/
Gangopadhyay et al. (1992)	1979–1988	75.5–70° W	position & transport	AVHRR T maps (0.1°)	yes	1 lon, yearly	/
Drinkwater et al. (1994)	1973–1992	75–50° W	position	analyst GS maps	no	26 lon, monthly	/
Sato & Rossby (1995)	1932–1988	75–68° W	transport	hydro stations	yes	130 stations, yearly	/
Taylor & Stephens (1998)	1966–1994	79–65° W	position	analyst GS maps	no	6 lon, monthly	GS - NAO-0: 0.02 (not sig.), GS - NAO-2: 0.55
Joyce et al. (2000)	1954–1989	75–55° W	position	Levitus T maps (1°)	yes	9 lon, yearly	GS - NAO-0: 0.6, GS - NAO-1: 0.6, GS - NAO-2: ¡0.45 (not sig.)
Curry & McCartney (2001)	1950–1997	gyres	transport	hydro stations	yes	2 stations, yearly	GS - NAO-0: ¡0.4 (not sig.), GS - NAO-1: ¡0.6
Frankignoul et al. (2001)	1992–1998	73–50° W	position	TOPEX altimeter	yes	17 tracks, ev. 10 days	GS - NAO-0: ¡0.05 (not sig.), GS - NAO-12m: ¡0.4, GS - NAO-16-17-18m: ¡0.4, GS - NAO-24m: ¡0.2 (not sig.)
De Coëtlogon et al. (2006)	1948–1998	75–55° W	position & transport	5 OGCM's (¿0.5°)	yes	17 lon, yearly	GS - NAO-0-1-2: ¡0.5
Peña-Molino & Joyce (2008)	1993–2007	76–60° W	position	TOPEX altimeter	yes	6 tracks, ev. 10 days	/
Chaudhuri et al. (2011)	58–71/80–93	75–45° W	position & transport	ROMS model (0.17°)	yes	(2 snapshots)	/
Sasaki & Schneider (2011)	1960–2003	75–55° W	position	OFES model (0.5°)	yes	41 lon, yearly	GS - NAO-0: ¡0.3 (not sig.), GS - NAO-1: ¡0.4, GS - NAO-2: 0.56
Pérez-Hernández & Joyce (2014)	1992–2012	75–45° W	position	AVISO SLA maps (0.25°)	yes	16 lon, monthly	GS - NAO-0: 0.4, GS NAO-1: 0.6, GS - NAO-2: ¡-0.15 (not sig.)
This study	1940–2014	70–50° W	position & transport	DIVA maps (0.25°)	yes	81 lon, monthly	GSNW - NAO-1: 0.37, GSD - NAO-0: 0.50, GSD - NAO-2: 0.43

Table 3.2: Compilation of studies dedicated to the detection of the GS position and/or transport. The column "Objectivity" refers to the method used to derive the GS characteristics. The spatial resolution refers to the data resolution in the case of hydrographic or satellite measurements, otherwise (analyst, model or interpolated maps) it refers to the number of longitudes used to create the GS index. Temporal resolution refers to the time axis of the GS index.

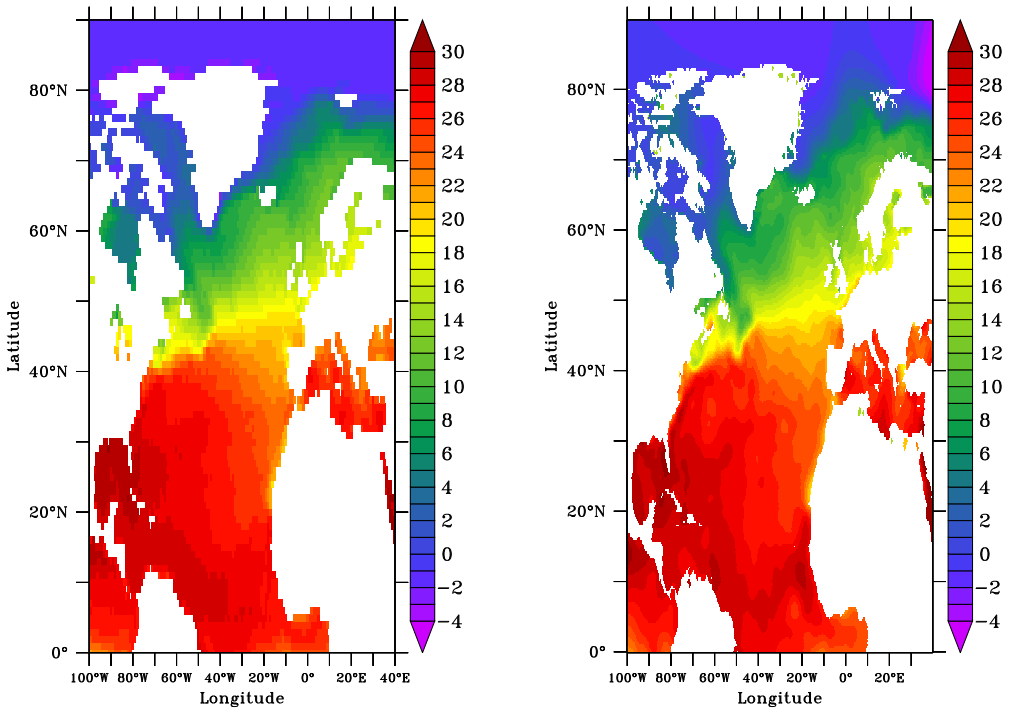

Figure 3.3: Sea Surface Temperature (°C) in August 1989 from ERA-20C reanalyses and DIVA analyses.

The RMSE between both products is computed over 1940–2010 and displayed in Figure 3.4. From these 4 panels, the RMSE is usually close to 1 °C in the North Atlantic, does not vary much with the season, significantly decreases between 1940 and 2010, and is generally below 2 standard deviations of the error on the DIVA analyses. Altogether, these results show that the DIVA analyses are relatively close to ERA-20C reanalyses. However, in the GS region, the RMSE is significantly higher (close to 2 °C), which indicates that the high resolution of the DIVA analyses brings new information in this area where the GS meanders at small scales, which is probably not resolved at the coarse grid of ERA-20C.

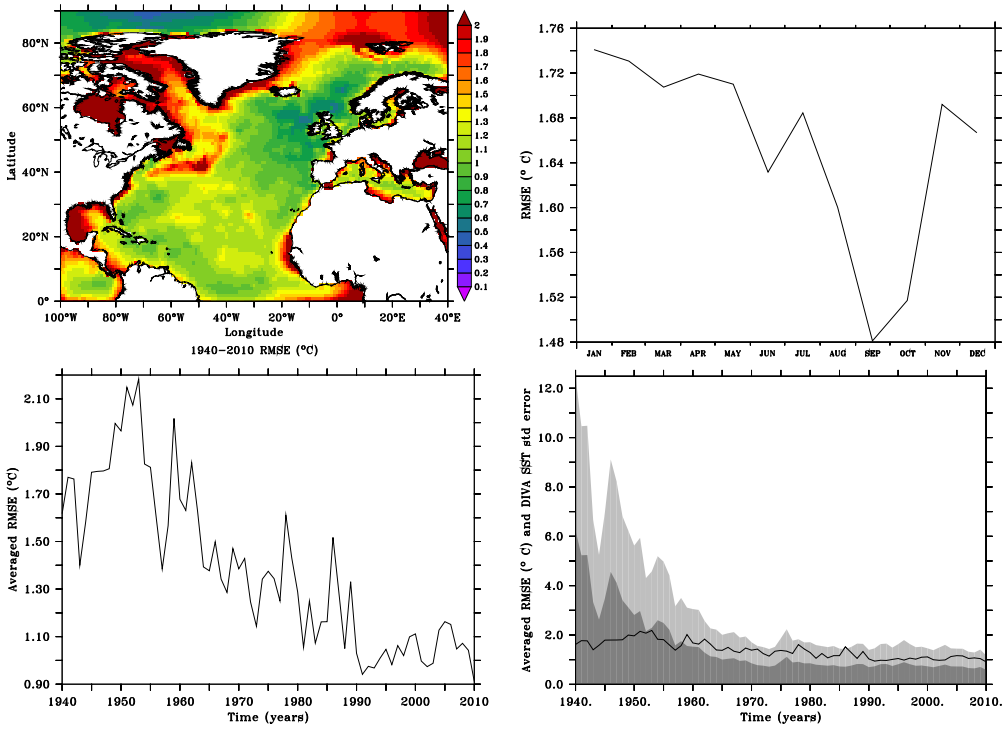

Figure 3.4: Comparison between ERA-20C reanalyses and DIVA analyses. Top left: two-dimensional root mean square error between the two products for the period 1940–2010. Top right: monthly root mean square error averaged on 1940–2010. Bottom left: averaged root mean square error over the domain shown in the top left panel. Bottom right: same as the bottom left panel with the averaged error on the DIVA analyses (1 standard deviation in dark grey, 2 standard deviations in light grey).

3.3 GS north wall index and NAO

In order to synthesize the interannual evolution of the GS position from our DIVA reconstruction, it was necessary to create a GS index to track the latitude of the GSNW. Following the literature in Section 3.1, we computed from our SST product a GSNW index based on the maximum gradient of SST at several longitudes. In order to find this GSNW, we performed a fit of the SST by an error function at 81 equally spaced zonal positions (0.25°) between 70°W and 50°W. The mathematical formulation of this function is:

$$f(y, p_1, p_2, p_3, p_4) = p_2 + p_3 \operatorname{erf}\left(\frac{y - p_1}{p_4}\right) \tag{3.3}$$

where, after the fit, p_1 is the latitude of the maximum gradient of SST, p_2 is the SST at this latitude, p_3 is half the SST difference between the waters north of the GS and south of it, and p_4 represents the strength of the SST gradient at the latitude p_1.

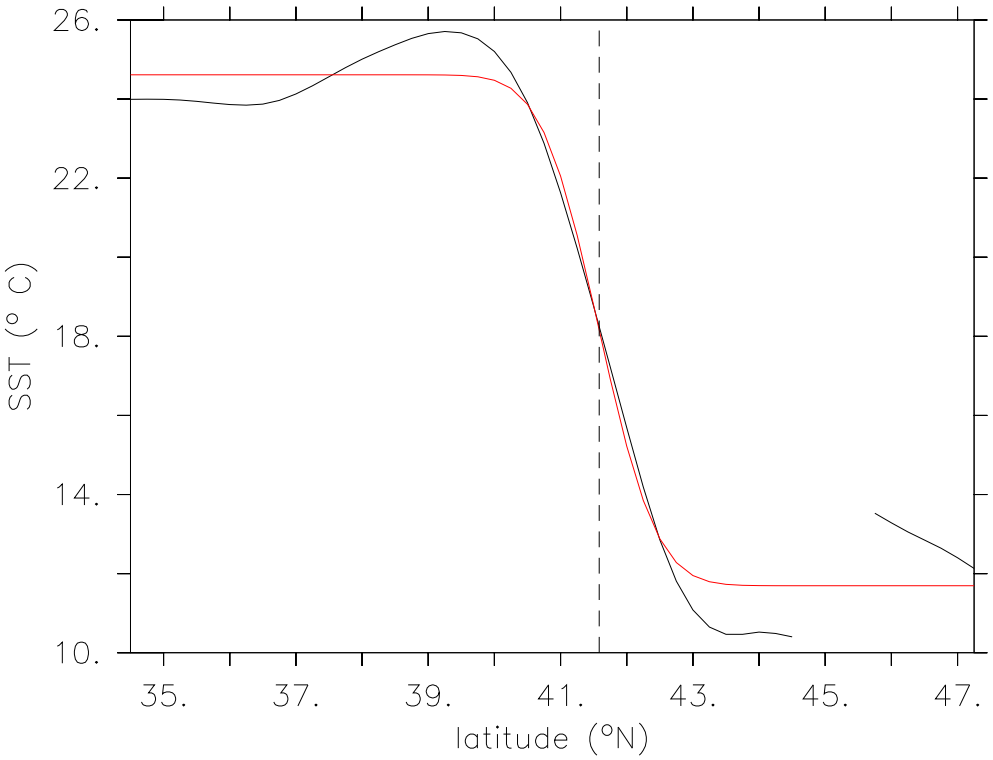

Figure 3.5: In black, our SST product in June 1984 at the longitude 63.25°W. In red, the fit by the error function. The fit focuses on the GS and avoids local maxima of the SST gradient. The dashed line represents the estimated latitude of the GSNW at this specific longitude.

The shape of the error function (erf) is particularly suited for the detection of the GS, smoothing the small artefacts and avoiding coastal gradients. Figure 3.5 shows an example of the fit while Figure 3.2 indicates the subdomain used for the GS detection. The 81 fits are then filtered by increasing the weight when the quality of the fit is good, and the converse. The quality of the fit is computed as the sum of the squared differences between the data and the fit. The filtering method is similar to that of the correlation length described in Equations 3.7 and 3.8. The 81 latitudes of the GSNW are then found as the highest slopes.

In order to derive the GSNW index, we performed an EOF analysis on these 81 GSNW latitudes for each month to obtain the main EOF representative of the north-south GS movement, which becomes our GSNW index after averaging on a yearly basis. This method is similar to those of Taylor & Stephens (1998) and Joyce et al. (2000), although ours is less sensitive to noise since we used more longitudes. The results are shown in Figure 3.6. Also shown in this figure is the Hurrel's NAO index with a lag of one year with respect to the GSNW index (NAO preceding GS).

In Figure 3.6, the high NAO phases around 1950, the mid-1970s and 1990s are coherent with our GSNW index, as well as the low NAO phases of early 1940s, 1960s, mid-1990s and early 2010s. Before 1940, SST analyses are often associated with a high error field, due to the sparsity of data. Therefore, we decided to keep only the reliable period 1940–2014 for the following correlations.

The correlations between our GSNW index and the NAO between 1940 and

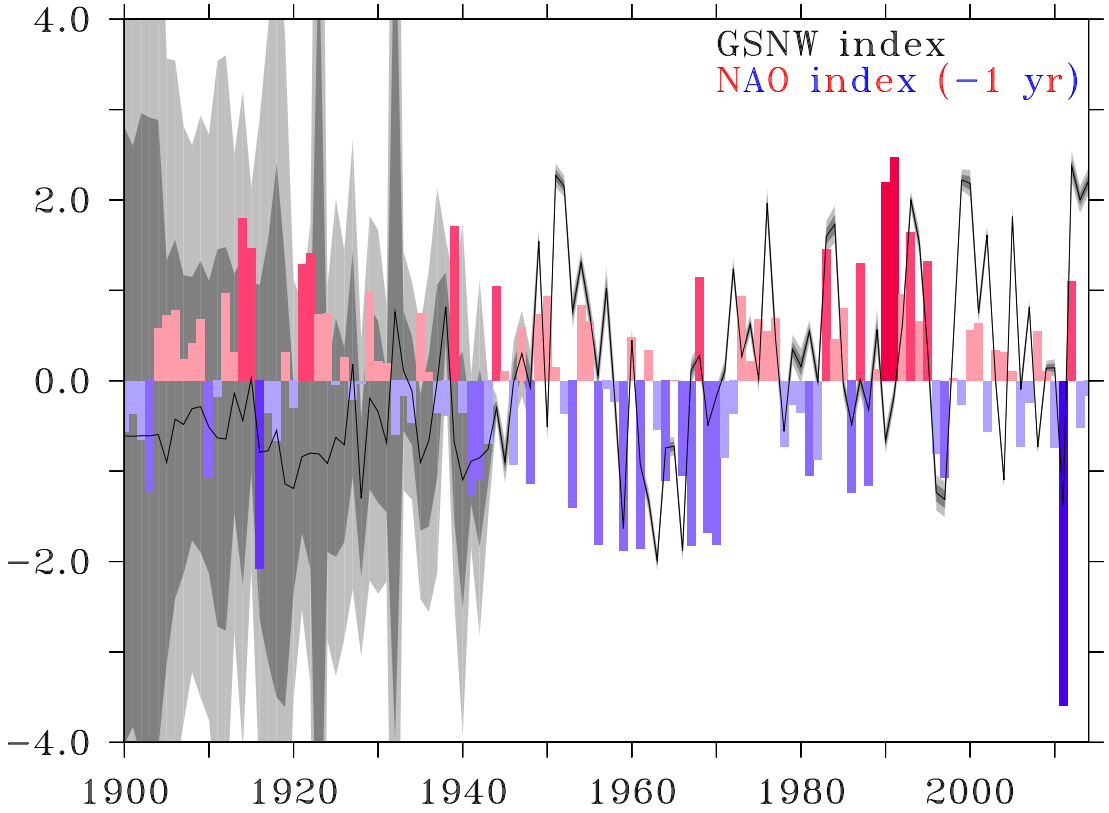

Figure 3.6: In black, our GSNW index between 1900 and 2014. In blue and red, the NAO annual index at a lag of one year. Both indices are expressed in standard deviations. A GSNW index of 1 corresponds to a shift of 17.75 km to the north. The shaded grey zones represent the estimated uncertainties in the GSNW index at one and two standard deviations.

2014 are 0.1812, 0.3692 and -0.02329 when using respective time lags of 0, 1 and 2 years (NAO preceding GS). Considering a level of confidence of 95%, the 1940–2014 correlation is significantly different from zero only when using a time lag of one year.

Given the important errors affecting the early century SST fields, a quality factor w_x was computed for each analysis from the relative error fields of DIVA. These error values were averaged over the oceanic part of the subdomain shown in Figure 3.2. The quality factor w_x for the GSNW index was then used in the correlation computation as follows, while the quality factor w_y for the NAO was set to a constant value due to a lack of information on its uncertainties:

$$r_{weighted} = \frac{\sum_{i=1}^{N} w_{x_i}(x_i - \bar{x}) w_{y_i}(y_i - \bar{y})}{\sqrt{\sum_{i=1}^{N} w_{x_i}^2 (x_i - \bar{x})^2} \sqrt{\sum_{i=1}^{N} w_{y_i}^2 (y_i - \bar{y})^2}} \tag{3.4}$$

where the averages $\bar{x}$ and $\bar{y}$ also take the quality factor w into account:

$\bar{x} = \sum_{i=1}^{N} w_{x_i} x_i$ and $\bar{y} = \sum_{i=1}^{N} w_{y_i} y_i$, where w_x and w_y are normalized so that their sum is equal to 1.

These weighted correlations between our GSNW index and the NAO for time lags of 0, 1 and 2 years are, respectively, 0.1771, 0.3718 and -0.01852 over 1940–2014. There is almost no difference with the unweighted correlations in 1940–2014, which means that putting more weight on the most reliable years implies an unchanged or slightly stronger correlation between the GSNW and the NAO. In other words, the less reliable years do not skew the correlations, at least after 1940. Here again, the correlation is maximum and significant at a level of confidence of 95% when the GSNW follows the NAO by one year.

Note 3.2: Do the NAO cycles affect the correlations?

As reported by Gangopadhyay et al. (2016), the NAO index includes several low frequency cycles. Cook et al. (1998) performed a winter NAO reconstruction in order to work with longer times series. Between 1700–1980, they found evidence for long-term NAO cycles with periods of 24, 8 and 2.1 years. However, the 2.1-year peak is the only one to clearly exhibit a significance above the 95% level of confidence. Besides, even if their reconstruction is stated as representing very well the spectral characteristics of the instrumental NAO, they acknowledge a rather low 41% of explained variance by the proxy-based index. Such a discrepancy raised questions about several proxy-based NAO reconstructions, as highlighted by the very critical study of Schmutz et al. (2000). According to them, the index used by Cook et al. (1998) (among others) cannot be considered as reliable when comparing it to low frequency oscillations of the NAO, although its performance improves with time. Furthemore, Wunsch (1999) found some evidence for weak signals in the winter NAO (1864–1996) at periods of 8–10 years and around 2 years, but also noted that such cycles contain less than 10%

of the total energy which is mainly concentrated at the highest frequencies. Finally, Gangopadhyay et al. (2016) reported similar oscillation periods (7–10, 5 and 3 years) when considering the winter NAO index between 1966–2006, with the 5-year peak being not significant at the 90% confidence level.

In order to further examine the occurrence of such NAO cycles in the annual index defined in Section 3.2, we computed the autocorrelations between 1940–2014 for lags ranging between 0–5 years (Figure 3.7). Except the trivial 0-year maximum, the other autocorrelations are very low as they peak at a maximum of 0.1. These results are consistent with Wunsch (1999) as they obtain very similar autocorrelations in their Figure 5.

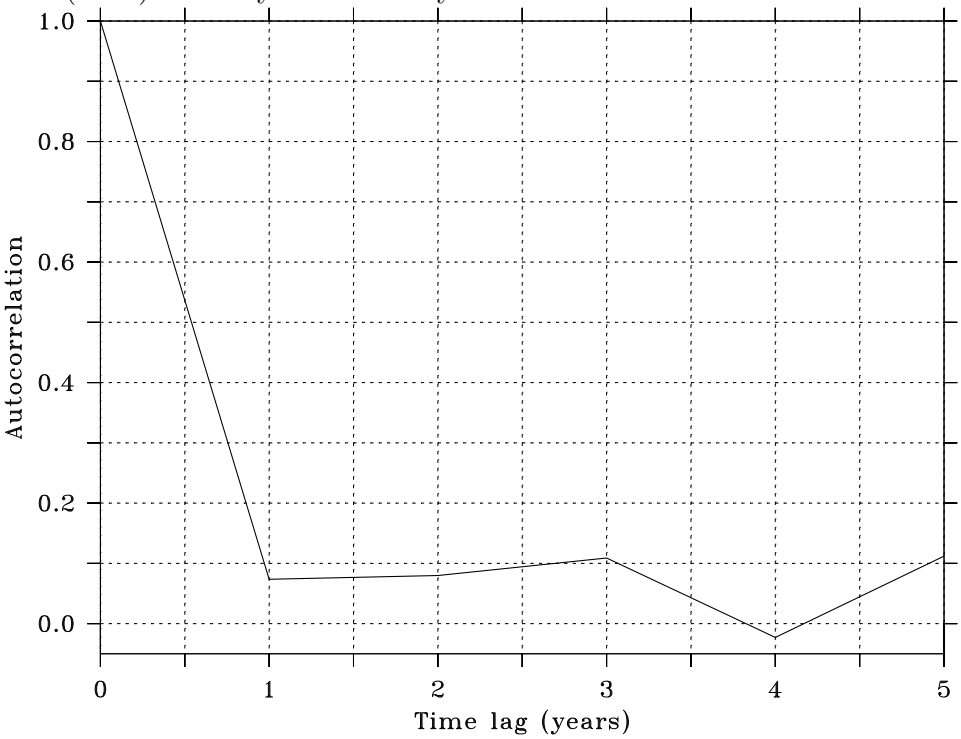

Figure 3.7: Autocorrelations of the annual NAO index as defined in Section 3.2 for time lags ranging between 0–5 years.

Furthermore, the impact of this weak NAO autocorrelation on correlations with GS properties is systematically taken into account when computing their level of significance (see Note 3.3). Altogether, the impact of NAO cycles on our results can be regarded as next to nil.

In Table 3.3, the GSNW index trends have been computed for various periods as well as their significance, following the Fisher-Snedecor test described in Chouquet (2009) and Montgomery et al. (2012). The GSNW index shows slight positive trends in the long term (1940–2014 and 1960–2014) although the GSNW has not significantly shifted to the north since 1980.

GSNW index	Slope	R^2	Trend
1940–2014	0.01339	0.07043	positive
1960–2014	0.02541	0.1351	positive
1980–2014	0.01584	0.02094	not significant

Table 3.3: Slope of the linear trend, coefficient of determination (R^2), and significance of the trend at a level of confidence of 95%.

3.4 GS delta index and NAO

To derive a simple proxy for the GS intensity from our SST analyses, we computed a GS Delta (GSD) index on our subdomain defined in Section 3.3. This GSD index is the normalized yearly average of the SST amplitudes across the GSNW, which are filtered and averaged beforehand over all the 81 longitudes (from 70°W to 50°W). These delta values are calculated from the derivative of 3.3 from which we only keep the amplitude part as $\frac{2p_3}{\sqrt{\pi}}$. The correlations shown in Table 3.4 are insignificant for the period 1940–2014, while the highest correlations between 1960 and 2014 are found when time lags of 0 and 2 years are considered. These two correlations are significant at a level of confidence of 95%, strengthening our confidence in the impact of a positive NAO phase on the intensification of the GS, and the converse.

Before 1960, the scarcity of data significantly affects our ability to measure the GS intensity. Indeed, modeling a large SST delta in DIVA requires a much better data density than tracking the latitude of the GSNW (see Section 3.2). We consider there is thus a negative bias in the GSD index over most of 1940–1960, due to too smooth SST fields in the vicinity of the GS. In those years, the variability is therefore underestimated because the GS intensity is never negative. These issues can only deteriorate the correlation with the NAO.

Figure 3.8a shows the evolution of the GSD index between 1940 and 2014 and its correlation (0.43) with the NAO at a lag of 2 years (NAO preceding GS). The strong positive NAO events of the mid-1970s and early 1990s are clearly followed by a stronger GS delta. The running averages presented in Figure 3.8b demonstrate in an even clearer way the close link between both indices after 1960.

GSD index	NAO (no lag)	NAO (lag = 1 year)	NAO (lag = 2 years)
1940–2014	0.2077	0.1667	0.2069
1960–2014	**0.4974**	0.2838	**0.4297**

Table 3.4: Correlations between our GSD index and the NAO, with a time lag of 0, 1 or 2 years (NAO preceding GS). The correlations in bold are significantly different from zero (at a level of confidence of 95%).

The GSD index trends are computed for various periods as well as their significance (not shown here), following the Fisher-Snedecor test described in Chouquet (2009) and Montgomery et al. (2012). While the GSD index has slightly increased since 1960, its trend is barely significant and the negative trends calculated since 1980 and 2004 remain insignificant. We did not find any significant negative trend for the period 2004–2012 either.

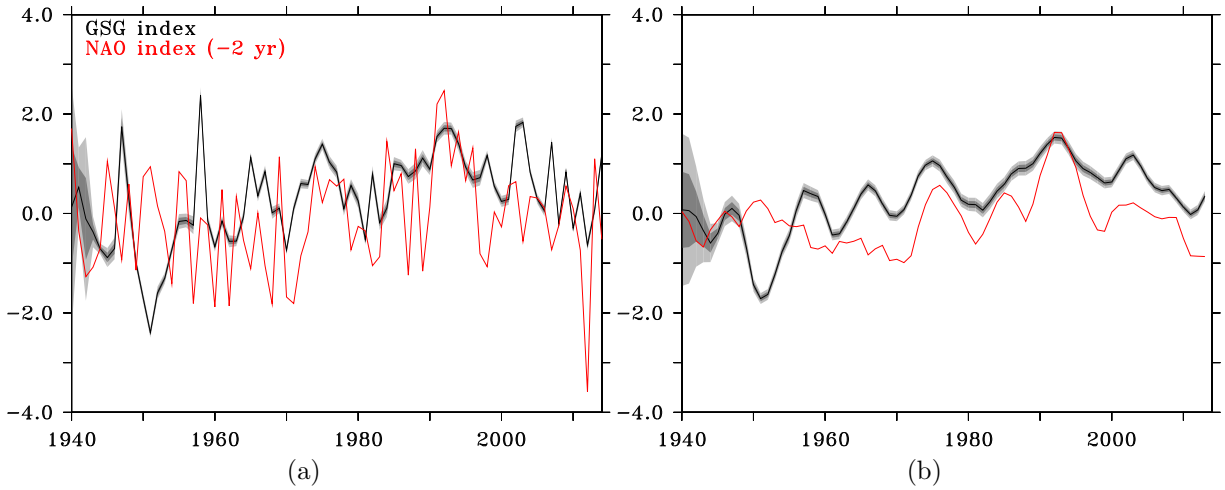

Figure 3.8: (a) GSD index between 1940 and 2014 computed from DIVA SST analyses (black) and NAO index lagged of 2 years (red). (b) Running averages of these indices (GSD and NAO) presented on a 4–year basis. (a) & (b) The shaded grey zones represent the estimated uncertainties in the GSD index, at one and two standard deviations.

3.5 Comparison with a satellite product

In order to strengthen the confidence in our GSNW and GSD indices, we used a satellite-based SST product to recalculate these indices over the shorter period 1982–2014. This product, called "Reynolds SST", is an optimal interpolation of SST derived from the Advanced Very High Resolution Radiometer (AVHRR) satellite sensor as well as from other platforms (ships, buoys). We used the product "AVHRR-only", available at a spatial resolution of 1/4 degree over the period 1981–present, on a daily basis. The methodology employed is described in Reynolds et al. (2007) and updated in Banzon & Reynolds (2013).

Figure 3.9 shows the good agreement on an annual basis between these two computations of the GSNW index. Between 1982 and 2014, the correlation between both GSNW indices is 0.7336. Since both interpolation schemes are similar (see Section 3.2), we do not expect the remaining discrepancies to be mainly due to the statistical method but rather to the datasets themselves. On the one hand, DIVA could smooth the field too much where the SST is likely to present strong gradients, but where not enough in situ data are available to compensate for that effect. This particular case could occur near the GS meanders, modifying somewhat the GSNW index. We expect this drawback to be limited since the in situ data coverage over 1982–2014 is excellent. On the other hand, the Reynolds SST product could also be affected by temporary unavailability of data around the GS meanders. For instance, Wentz et al. (2000) showed that, due to the presence of clouds, the GS is sometimes barely visible in the Reynolds product compared to SST images produced by a microwave sensor (TMI, launched in 1997).

Furthermore, we compared both indices with an updated version (A.H. Taylor, February 2017, personal communication) of the GSNW index presented in Taylor

& Stephens (1998). Although significant, both correlations with the satellite-based and DIVA-based indices are lower : respectively 0.4458 and 0.4331. However, the large variations over several years are still rather well depicted. In order to compare both the Taylor and DIVA indices on more comparable domains, we recomputed our GSNW index on the western half of our domain (70–60°N). The correlation improved somewhat to 0.5315, which indicates the choice of the domain explains a part of the remaining discrepancies. However, as stated in Section 3.2, other reasons can also be invoked for this. Firstly, the Taylor index relies on GS charts that were drawn subjectively, and switching between two different thresholds to track the GS position. Secondly, Taylor & Stephens (1998) only used 6 longitudes to build their index, which could thus be more sensitive to noise. Finally, the correlations between our GSNW index narrowed to 70–60°N and the NAO remains virtually unchanged, regardless of the time lag.

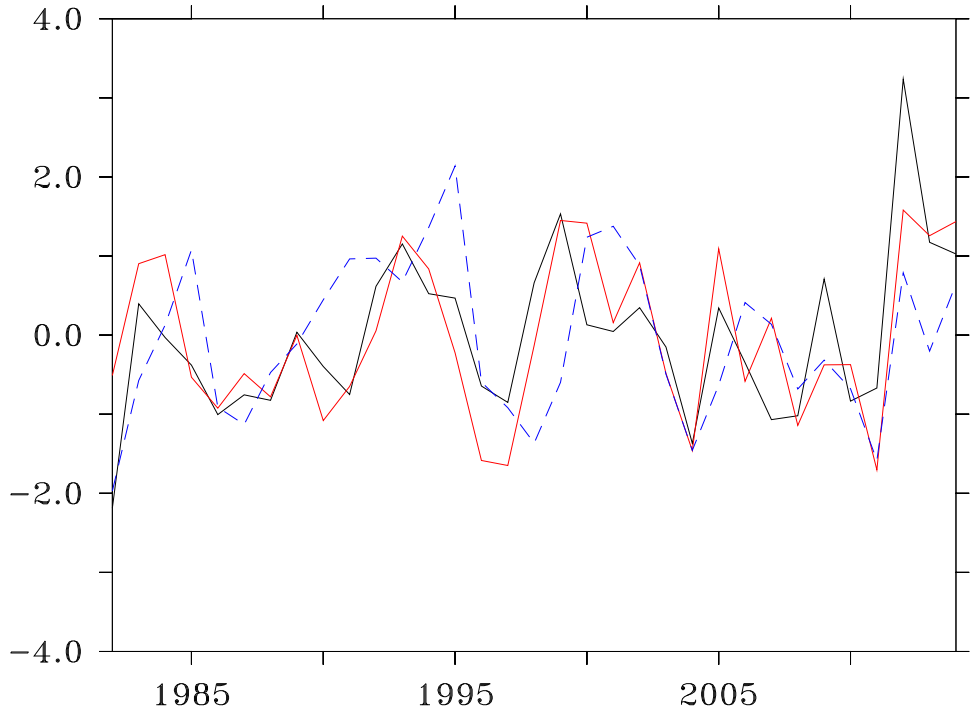

Figure 3.9: GSNW index between 1982 and 2014 computed from DIVA SST analyses (red) and Reynolds SST (black). The correlation is 0.7336. In dashed blue, the GSNW index from Taylor & Stephens (1998) updated to 2014. Its correlation with the Reynolds index is 0.4458.

Considering the GSD indices, we have a similar agreement between both sources (DIVA and Reynolds) with a correlation coefficient of 0.7559. In the vast majority of cases, the interannual evolution has the same sign for both products (see Figure 3.10), which is a critical point towards forecasting of the GS characteristics.

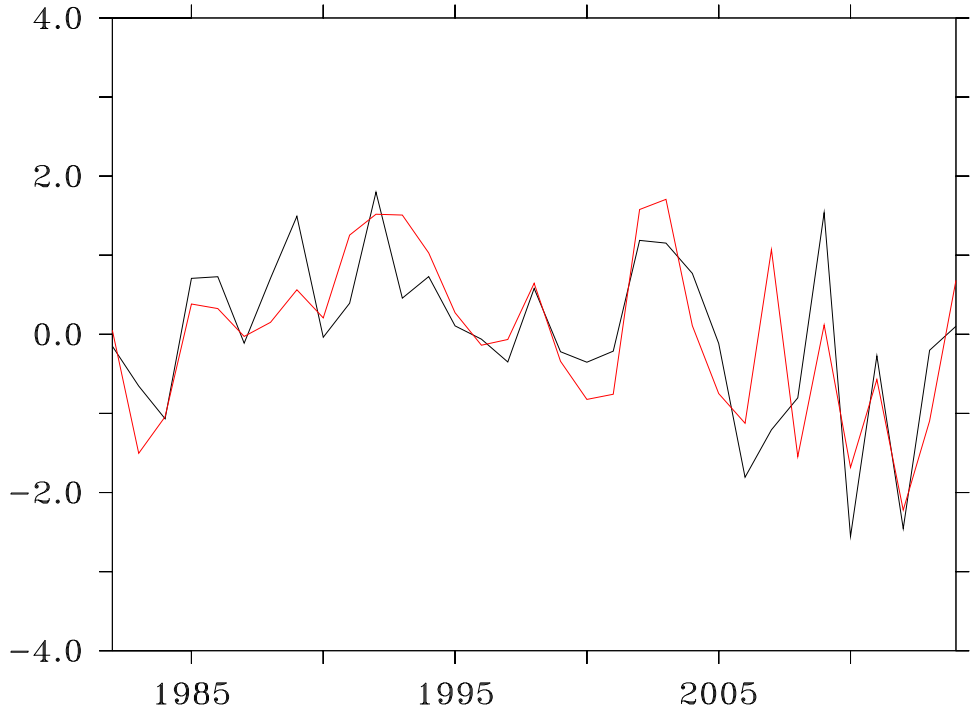

Figure 3.10: GSD index between 1982 and 2014 computed from DIVA SST analyses (red) and Reynolds SST (black). The correlation is 0.7559.

3.6 GS transport index

With the aim of assessing the quality of the GSD index as a proxy for the GS transport, we decided to compute the geostrophic transport associated with our temperature and salinity products at 15 depths. The computation of this GS transport (GST) index requires the determination of the density. For each of our 81 longitudes, the density is computed from 6° south of the GSNW position to 2° north of it. The calculus is based on the linearized version of the Unesco state equation 1980, concerning which details are provided in Talley (2011). These monthly density slices are then averaged together along the GS path. The level of no motion is chosen as our deepest level (3000 m depth), from which we are able to reconstruct the geostrophic horizontal speed (u_g,v_g) at every depth up to the surface as per:

$$f\frac{\partial v_g}{\partial z} = -\frac{g}{\rho_0}\frac{\partial \rho'}{\partial x} \tag{3.5}$$

$$f\frac{\partial u_g}{\partial z} = \frac{g}{\rho_0}\frac{\partial \rho'}{\partial y} \tag{3.6}$$

where ρ' is the density anomaly with respect to the density of a reference ocean ρ_0 and the Coriolis frequency $f = 2\Omega sin\lambda$ with λ the latitude and Ω the angular speed of Earth's rotation.

These average speeds are then computed on a finer grid every 50 m depth . Figure 3.11 shows an example of average speeds parallel to the GS path in March 2014. The GS core is rather easy to identify, and is located as expected just south of the position of the GSNW. The situation is virtually the same every month : a

distinct ribbon of higher speeds ($> 0.1 - 0.15\, m/s$) south of the GSNW, with speeds very close to zero at depths above 1000 m.

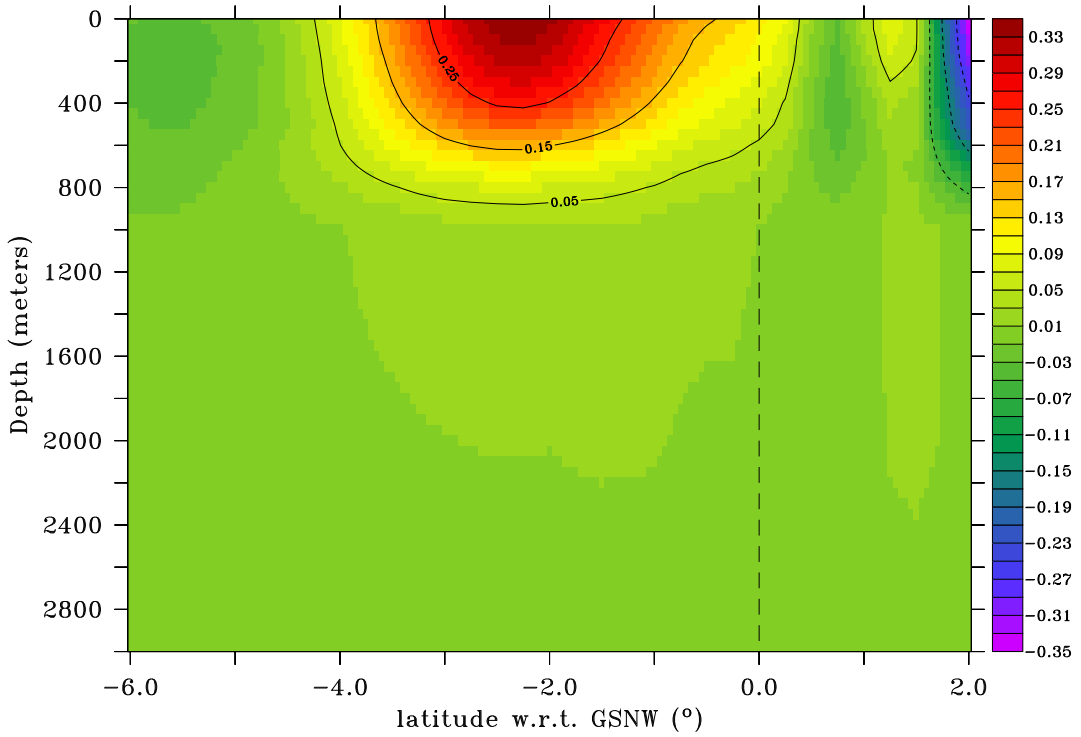

Figure 3.11: Average speeds (m/s) along the GS path in March 2014. The dashed line represents the position of the GSNW.

We then computed the flow rate for each cell where the speed is higher than 0.15 m/s. In general, this threshold corresponds quite well with the GSNW and is not too low, so that a GS core is detected even when data are less abundant. The flow inside the GS core is integrated, and then normalised in the same way as the GSD was. Since we need an analysis for each depth to compute the speeds from the bottom to the surface, the method requires data at each level otherwise no GST index is computed, as shown in Figure 3.12 for years 1942–1946. In this figure, we show the relatively good agreement between GSD and GST indices on a decadal scale, although the correlation is too weak to be significant.

In Table 3.5, we list the correlations between our GST index and the NAO for various time lags. Although only the correlations without time lag are significant, the higher ones over both the 1940–2014 and 1960–2014 periods are found each time when using a time lag of 0 and 2 years, similarly to the GSD behaviour. In order to further study the response of the GSD and GST indices to NAO events between 1960–2014, we recalculated both indices over running years starting in February, March,... This allowed us to use time lags in multiples of one month for computing the correlations with the NAO. The result can be seen in Figure 3.13, where it clearly appears that both curves are virtually parallel. Besides, the correlation between GSD and NAO peaks at 0.5273 and 0.4521 when using respective lags of 1 or 29 months, while the GST curve shows similar optimal time lags of 0 and 28 months corresponding to the local correlation maxima of 0.3030 and 0.2596. This

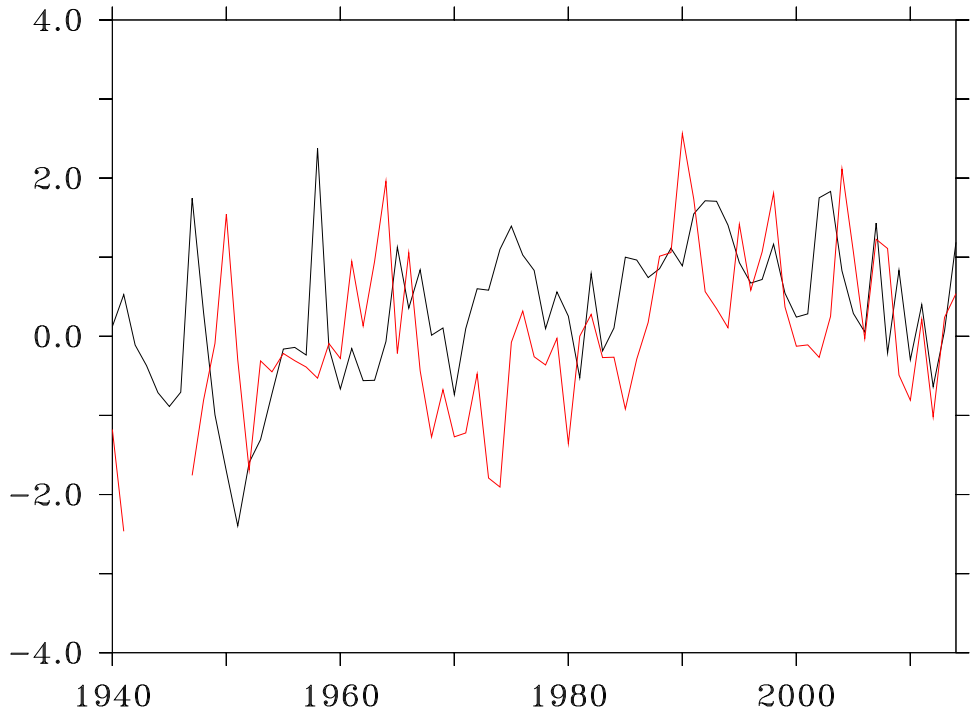

Figure 3.12: GSD index between 1940 and 2014 computed from DIVA SST analyses (black) and our GST index computed from DIVA analyses of temperature and salinity at 15 depths (red). The correlation is 0.1475 between 1940–2014.

last value is the only one not to be significant, although the significance threshold is very close (0.3005). We also note that here, as well as throughout the paper, we used the most severe significance test that includes a penalisation for the autocorrelation (see Wilks (1995)).

Note 3.3: On the tests of significance

Throughout this Chapter, the Fisher-Snedecor test is used in order to assess the significance of correlations and trends. Following Chouquet (2009), the statistics

$$F = (n-2)\frac{R^2}{1-R^2}$$

follows a Fisher distribution $\mathcal{F}$ with $(1; n-2)$ degrees of freedom, where n is the length of the time series and R^2 is the coefficient of determination. The correlation or the trend is significantly different from zero if $F > \mathcal{F}_{1;n-2;1-\alpha/2}$ where α is chosen as to ensure a level of confidence of 95%.

However, oceanographic time series often contains autocorrelation to some degree, which might artificially increase the correlation between time series. In other words, the level of significance could be reached too easily (see e.g. Ebisuzaki (1997)), which needs to be addressed on a case-by-case basis. With this in mind, the lag-1 autocorrelation coefficient ρ_1 is computed for each time

series and allows for an estimate of the effective sample size

$$n^{'} = n\frac{1-\rho_1}{1+\rho_1}$$

which yields higher levels of significance for the same level of confidence, except in the absence of autocorrelation where $n = n^{'}$ is retrieved (Wilks, 1995).

This procedure was applied to all trends and correlations, keeping the most penalising effective sample size from two time series. This ensures a reliable filtering of non-significant results.

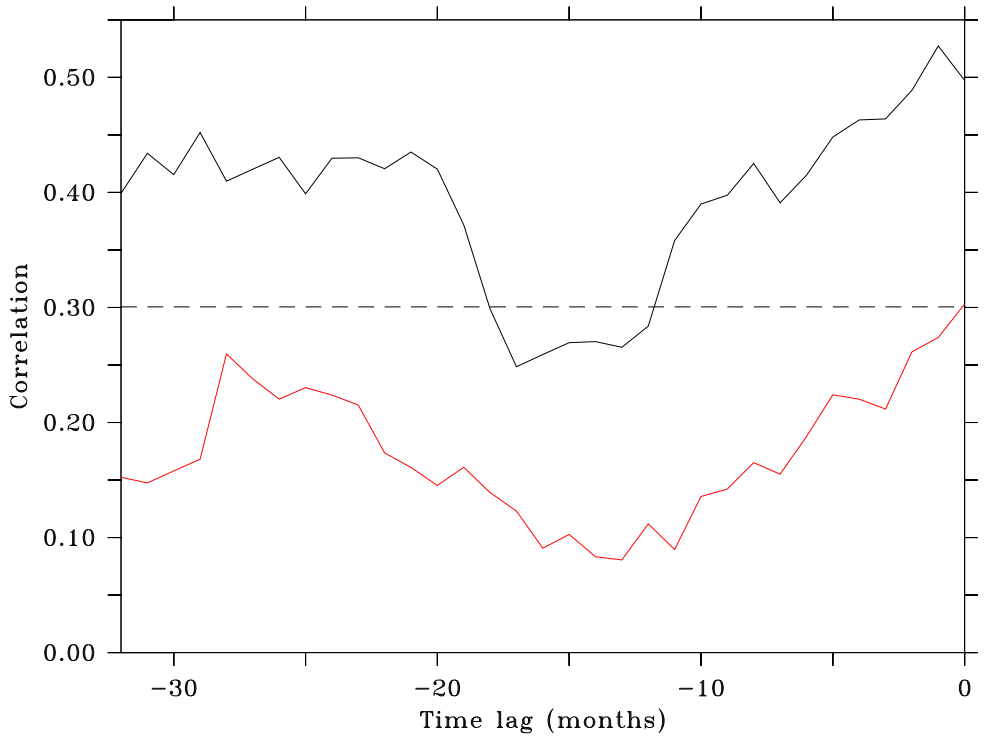

Figure 3.13: Correlations according to time lag between the GSD index and NAO (black), and between the GST index and NAO (red) between 1960–2014, NAO preceding GS. The dashed line represents the significance threshold.

We conclude from this comparison of correlations that the GST shows a similar response to the NAO as the GSD does, while its intensity is weaker. We suggest this weak signal is mainly linked to the difficulties in detecting gradients below the ocean surface. Indeed, the density of data decreases rapidly with depth, forcing the analyses to be smoother and closer to the reference state. On top of that, the GST index requires the availability of both temperature and salinity, while the GSD does not.

Note 3.4: Sensitivity to the NAO index

In order to test the sensitivity of the correlations to the NAO index, we recomputed them by using the NAO index provided by the CPC. This monthly index

GST index	NAO (no lag)	NAO (lag = 1 year)	NAO (lag = 2 years)
1940–2014	**0.3476**	0.1620	0.2202
1960–2014	**0.3030**	0.1119	0.2239

Table 3.5: Correlations between our GST index and the NAO, with time lags of 0, 1 or 2 years (NAO preceding GS).

is available since 1950 and can be found here: `https://www.cpc.ncep.noaa.gov/products/precip/CWlink/pna/nao.shtml#publication`. This NAO index is based on the anomalies of the geopotential 500 hPa between 20-90° N over the NA. Both the NAO and the GS monthly indices were averaged on a yearly basis. The references for this alternative NAO index are the following: Barnston & Livezey (1987), Chen & Van den Dool (2003) and Van den Dool et al. (2000). The correlations are shown in Table 3.6 and are consistent with the time lags already found between the Hurell's NAO and the GS indices.

r(1950–2014)	NAO	NAO (-1 yr)	NAO (-2 yr)
GSNW	0.1408	**0.3257**	-0.05597
GSD	**0.3339**	0.2028	**0.3750**
GST	**0.2825**	0.07576	0.1430

Table 3.6: Correlations between the CPC NAO and the GS indices with various time lags for the period 1950–2014. Both indices are averaged on a yearly basis. The correlation in bold are statistically significant.

3.7 Summary and discussion

In this study we make significant improvements to the way in which the GS evolution is quantified. We used 5 well-known databases to build the largest dataset ever used for this purpose. This collection of in situ data was analysed objectively to produce 4D gridded products of temperature and salinity fields in the GS region. This was achieved by using the DIVA software, which allows each analysis to be as close as possible to the true state by making use of VIM, a technique equivalent to OI which minimises the expected error. From there, we were able to compute GS position, delta and transport indices for a record-breaking duration of 75 years. These indices are available at `https://swatelet.github.io/#gs-indexes`.

On the one hand, the latitude of the GSNW is significantly correlated with the NAO, with a delay of 1 year. This result is in accordance with the papers of Taylor & Stephens (1998), Joyce et al. (2000), Sasaki & Schneider (2011), Chaudhuri et al. (2009, 2011) and Pérez-Hernández & Joyce (2014), although the delay may vary. On the other hand, the intensity of the GS is significantly correlated with the NAO, with a delay of about 0 or 2 years. Our GST index responds similarly to the NAO. This result is in accordance with Sato & Rossby (1995), Curry & McCartney (2001), De Coëtlogon et al. (2006), Penduff et al. (2004) and Chaudhuri et al. (2011), but in disagreement with Gangopadhyay et al. (1992).

In both cases, one may wonder if these positive correlations are the sign of a physical link, or just statistical parameters indicating internal processes implying strong autocorrelations, without any cause and effect relationship between NAO and GS. With this aim in mind, we computed the autocorrelations of the GSNW, GSD and NAO, with an offset of 1 and 2 years, for 1940–2014 and 1960–2014. These autocorrelations are always weaker than the significant correlations found in the same tables, indicating the existence of a physical link between the NAO and the GS.

The literature suggests these correlations and time lags to be linked with Rossby waves propagating westwards. Such Rossby waves have been observed by Cipollini et al. (1998) in the Northeast Atlantic. Using data from TOPEX/POSEIDON radar altimeters, they draw longitude/time (or Hovmöller) diagrams of SSH at given latitudes on which they applied Fast Fourier and Radon transform. The clearest signal of Rossby waves they were able to reveal occurs around 33–34° N, thanks to graphs of energy density derived from the Radon transform. The main peaks of energy correspond to speeds of 3–4 km/day. Similarly, De Coëtlogon et al. (2006) used Hovmöller diagrams in the GS region to explain the time lag between the NAO and GS transport. They found some evidence for Rossby waves travelling westwards at 27 and 32° N with a speed close to respectively 3.5 and 2.5 cm/s as calculated by Chelton et al. (1998), while Osychny & Cornillon (2004) found similar wave speeds. This is roughly consistent with the delay of 2 years we computed between the NAO and the GS transport and strengthens the hypothesis for Rossby waves generated by NAO variability and propagating from the center of the NA Ocean towards the west. According to De Coëtlogon et al. (2006), this slow response to the NAO is linked to the baroclinic component of the Rossby waves, while the faster one (less than one month) is due to its barotropic component. The link between the NAO, the Rossby waves and the GS is extensively addressed in Chapter 4.

Finally, in the context of global warming, a relevant question is the possible weakening of the GS in recent decades. According to the IPCC (Solomon et al., 2007; Stocker et al., 2013), the Atlantic Meridional Overturning Circulation (AMOC) is predicted to decrease over the 21^{st} century. The IPCC (Stocker et al., 2013) also reported "medium confidence" in a near-term increase of the NAO. Smeed et al. (2014) observed a significant decrease of 2.7 Sv in the AMOC between 2004–2008 and 2008–2012. Most of this change is due to the mid-ocean geostrophic flow (-2 Sv), while the GS and Ekman transports decreased, respectively, by 0.5 and 0.2 Sv. These two last trends are however not significant. The stability of the GS transport is strengthened by the study of Rossby et al. (2014) using Doppler current profilers and showing no significant trend over the longer 1992–2012 period. Our GSD trends tend to indicate that the GS has not weakened since 1960, 1980 or 2004. As Smeed et al. (2014) stated, we did not find any significant negative trend for 2004–2012 either.

3.A Vertical filtering of the correlation length

Some notation and definitions are presented in Table 3.7.

Quantity	Definition	Remark
l_k^*	initial correlation length	layer k
l_k	filtered correlation length	layer k
$\bar{L}$	arithmetic average of the l_k	
z_k	depth (m)	layer k
K	number of layers	$K = 15$
Δ	$\dfrac{z_1 - z_k}{K-1}$	
N_k	number of samples used in the optimization of l_k	
q	quality of the l_k optimization	$\in [0,1]$
α_k	$\dfrac{N_k}{100}\max(q-0.7,0)$	

Table 3.7: Notation and definitions.

We minimize a cost function made of three terms, penalizing the distance between l_k and its initial value, its neighbours, and its vertical average:

$$\sum_{k=1}^{K} \alpha_k (l_k - l_k^*)^2 + \sum_{k=2}^{K} \Delta^2 \left(\frac{l_k - l_{k-1}}{z_k - z_{k-1}} \right)^2 + \sum_{k=1}^{K} (l_k - \bar{L})^2. \tag{3.7}$$

The minimization process gives:

$$\begin{pmatrix}
M_{11} & C_1 & 0 & 0 & 0 & 0 & 0 & 0 & 0 & 0 & 0 & 0 & 0 & 0 & 0 \\
A_2 & B_2 & C_2 & 0 & 0 & 0 & 0 & 0 & 0 & 0 & 0 & 0 & 0 & 0 & 0 \\
0 & A_3 & B_3 & C_3 & 0 & 0 & 0 & 0 & 0 & 0 & 0 & 0 & 0 & 0 & 0 \\
0 & 0 & & & & 0 & 0 & 0 & 0 & 0 & 0 & 0 & 0 & 0 & 0 \\
 & & & & \ddots & & & & & & & & & & \\
0 & 0 & 0 & & & 0 & 0 & 0 & 0 & 0 & 0 & 0 & 0 & 0 & 0 \\
0 & 0 & 0 & 0 & & & 0 & 0 & 0 & 0 & 0 & 0 & 0 & 0 & 0 \\
0 & 0 & 0 & 0 & 0 & & & 0 & 0 & 0 & 0 & 0 & 0 & 0 & 0 \\
0 & 0 & 0 & 0 & 0 & 0 & A_k & B_k & C_k & 0 & 0 & 0 & 0 & 0 & 0 \\
0 & 0 & 0 & 0 & 0 & 0 & 0 & & & 0 & 0 & 0 & 0 & 0 & 0 \\
0 & 0 & 0 & 0 & 0 & 0 & 0 & 0 & & & 0 & 0 & 0 & 0 & 0 \\
 & & & & & & & & & \ddots & & & & & \\
0 & 0 & 0 & 0 & 0 & 0 & 0 & 0 & 0 & & & 0 & 0 & 0 & 0 \\
0 & 0 & 0 & 0 & 0 & 0 & 0 & 0 & 0 & 0 & & & 0 & 0 & 0 \\
0 & 0 & 0 & 0 & 0 & 0 & 0 & 0 & 0 & 0 & 0 & & & & 0 \\
0 & 0 & 0 & 0 & 0 & 0 & 0 & 0 & 0 & 0 & 0 & 0 & A_{K-1} & B_{K-1} & C_{K-1} \\
0 & 0 & 0 & 0 & 0 & 0 & 0 & 0 & 0 & 0 & 0 & 0 & 0 & A_K & M_{KK}
\end{pmatrix}
\begin{pmatrix} l_1 \\ \vdots \\ l_{k-1} \\ l_k \\ l_{k+1} \\ \vdots \\ l_K \end{pmatrix}
=
\begin{pmatrix} \alpha_1 l_1^* + \bar{L} \\ \vdots \\ \alpha_{k-1} l_{k-1}^* + \bar{L} \\ \alpha_k l_k^* + \bar{L} \\ \alpha_{k+1} l_{k+1}^* + \bar{L} \\ \vdots \\ \alpha_K l_K^* + \bar{L} \end{pmatrix} \tag{3.8}$$

where

$$M_{11} = \alpha_1 + \frac{\Delta^2}{(z_2 - z_1)^2} + 1;$$

$$M_{KK} = \alpha_K + \frac{\Delta^2}{(z_K - z_{K-1})^2} + 1;$$

$$A_k = \frac{-\Delta^2}{(z_k - z_{k-1})^2};$$

$$B_k = \alpha_k + \frac{\Delta^2}{(z_k - z_{k-1})} + \frac{\Delta^2}{(z_{k+1} - z_k)} + 1;$$
$$C_k = \frac{-\Delta^2}{(z_{k+1} - z_k)^2}.$$

Since the matrix M in (3.8) is tridiagonal, the system can be solved by a method based on the Thomas algorithm (Cushman-Roisin & Beckers, 2011) that has been implemented in DIVA since version 4.6.4.

Chapter 4

Rossby waves in the North Atlantic

Contents

Preliminary remark

Most of this Chapter was submitted to Ocean Science as Watelet, Beckers, Molines & Troupin (2020a).

4.1 Introduction

Although there is growing evidence of teleconnections between the North Atlantic Oscillation (NAO) and the variability of the Gulf Stream (GS) path and transport (e.g. Taylor & Stephens, 1998; Joyce et al., 2000; De Coëtlogon et al., 2006; Sasaki & Schneider, 2011; Watelet et al., 2017), the physical causes are yet to be further explored in the light of the literature suggesting the time lags might be attributed to Rossby waves carrying the NAO signal from the central North Atlantic (NA) towards the GS region. Given the long time lags involved, establishing a cause and effect relationship between NAO and GS is fundamental to boost the predictability of the GS characteristics.

Rossby waves in the NA were first observed by Chelton & Schlax (1996) using 3-year time series from TOPEX/Poseidon altimeters, before Cipollini et al. (1997) confirmed their presence around 34°N by combining Sea Surface Height (SSH) from TOPEX/Poseidon and Sea Surface Temperature (SST) from ERS-1 radiometer. They developed an objective detection technique based on Hovmöller (or longitude-time) diagrams (Hovmöller, 1949) of SSH or SST and Fast Fourier transforms applied on them, the method being extensively described in Cipollini et al. (2006). This technique allowed the detection of what are suggested to be the three first baroclinic modes of Rossby waves propagation, with estimated speeds of 2.7, 1.6 and $0.8\,\mathrm{km\,d^{-1}}$ (i.e. 3.1, 1.9 and $0.93\,\mathrm{cm\,s^{-1}}$) at 34°N and between 37-8°W. De Coëtlogon et al. (2006) later used similar Hovmöller diagrams based on transport outputs from an Oceanic General Circulation model (OGCM) to explain the 2-year time lag between the NAO and the GS transport, and found evidence for baroclinic Rossby waves travelling at speeds close to 3.5 and $2.5\,\mathrm{cm\,s^{-1}}$ at 27°N and 32°N, as previously computed by Chelton et al. (1998). They also suggested the fast (less than 1 month) response of the GS transport to the NAO could be due to faster barotropic Rossby waves. Osychny & Cornillon (2004) also used TOPEX/Poseidon SSH data to show evidence of Rossby waves, in particular at 39°N in the NA, where they travel at estimated speeds comprised between 3–$4\,\mathrm{cm\,s^{-1}}$. Finally, Lecointre et al. (2008) showed a high-resolution (1/6°) numerical model can generate Rossby waves at speeds similar to those detected from altimetry.

The present study aims at detecting Rossby waves from a state-of-the art eddy-resolving model. The region of interest is located around the latitude of the average GS path (∼39°N). At these relatively high latitudes, Rossby waves detection is still challenging, and only a few studies can be found in the literature (e.g. Osychny & Cornillon, 2004). The use of a numerical model instead of satellite data has the advantage of being independent of the satellite constellation as well as allowing future subsurface exploration of these waves. Besides, the simulations used here cover a longer time span including the pre–TOPEX/Poseidon era (i.e. before 1992), which fosters the detection of such slow signals.

4.2 Data and methods

We have used the outputs of a global hindcast performed in the frame of the DRAKKAR project (Barnier et al., 2006, 2007) at the eddy-resolving resolution

of 1/12° with the ORCA12 configuration described here (`https://github.com/meom-configurations/ORCA12.L46-MJM189`). This hindcast is based on the NEMO ocean / sea ice GCM numerical code (Madec & NEMO-team, 2016). In the past, similar simulations based on OPA 8.1 were performed during the CLIPPER experiments and compared to Eddy Kinetic Energy (EKE) satellite observations by Penduff et al. (2004) whereby concluded to a reasonable agreement. In addition, such simulations showed a good agreement with altimetry when considering Rossby waves phase occurence and speeds (Lecointre et al., 2008), which is a prerequisite for our study. Both studies were however performed with a 1/6° ORCA grid, which is only eddy-permitting at the latitudes of interest. Besides, Barnier et al. (2006) also showed the introduction of partial steps topography can significantly improve mean flow and EKE representation, leading to simulations at 1/4° (NEMO) performing as well or even better than above-mentioned 1/6° simulations (OPA 8.1). Using this numerical development, Penduff et al. (2010) and then Sérazin et al. (2015) showed how increasing the resolution from 1–2° to 1/4° or 1/12° allows a better agreement between altimetry and modeled SSH. We therefore expect a quantitative improvement in the Rossby waves detection from the use of an enhanced resolution.

This simulation covers the period 1958–2015 and was forced by the interannual DRAKKAR Forcing Set DFS5.2 (based on a rescaling of ERA-Interim ECMWF atmospheric re-analysis) (Dussin et al., 2018). The relevant parametrisations for this study are: linear filtered free surface technique to avoid fast barotropic waves, biharmonic horizontal lateral viscosity, and isopycnal lateral diffusivity. Vertical mixing is controlled by the TKE scheme (Blanke & Delecluse, 1993; Madec et al., 1998).

The basic data set consists of the SSH fields (5–day average) model output, for the period 1970–2015, extracted from the global simulation on the NA (0–65°N). These fields are available at 10.5281/zenodo.3968801 between 38 and 40°N (Molines, 2020). The chosen period allows for a 13–year spin-up of the simulation. We decided to focus on the latitude 39°N which was considered representative of the average GS path from our SST fields in Watelet et al. (2017). Here, indeed, we only examine the zonal component of the Rossby waves travelling across the NA. Since this study focus on the delayed impact of the NAO on the GS, other latitude bands are considered outside the scope of this paper. Regarding longitudes, we chose to analyse propagating signals from 30 to 70°W, i.e. between the approximate center of the NA at 39°N where we can expect the NAO signal to be carried to the ocean through wind forcing and the western limit of the GS region as defined in Watelet et al. (2017).

These SSH fields, originally provided at a horizontal resolution of 1/12° (ORCA12 grid), were interpolated bilinearly to a constant 1/12.5° or 0.08° grid in order to avoid truncation issues with repeating decimals. From there, we removed the climatological annual cycle as well as the 1970–2015 trend. The data set is available at 10.5281/zenodo.3968885 (Watelet, 2020). Figure 4.1 shows these detrended SSH anomalies as an Hovmöller (or lon-time) diagram. On this diagram, Rossby wave-like patterns are already visible as the lines of similar SSH with a slope tilted to the left and close to the vertical. Looking at a much shorter time scale (see Figure 4.2), between 1985–1988, it is even possible to draw subjective slopes (dotted lines)

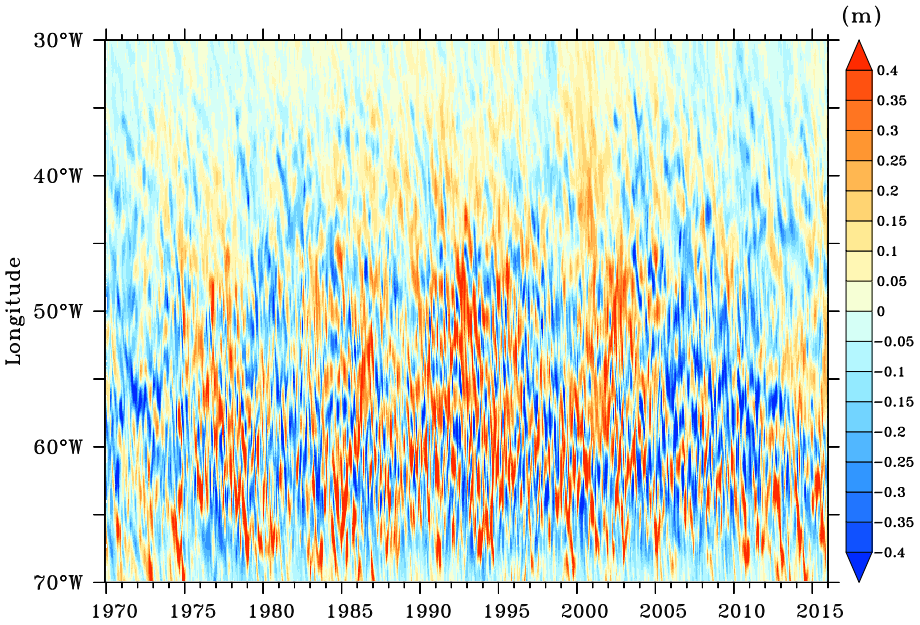

Figure 4.1: Hovmöller diagram of detrended SSH anomalies at 39°N between 30–70°W and 1970–2015, showing Rossby wave-like patterns. A running average on 30 days and 28 km is applied.

of these waves, allowing a rough estimate of their speed.

Detrended SSH anomalies between 70-30°W and 37-43°N averaged on 30 days also make it possible to detect features propagating westward, especially in the eastern part of the domain. West of 50°W, these waves are more difficult to discern, probably because this relatively weak and varying signal interacts with the strong flow of the GS and its meanders.

With the aim of avoiding subjective biases, we then followed the method explained in detail in Cipollini et al. (2006). At first, the SSH fields were averaged with moving 30-day and 28-km boxcar windows in order to avoid short space and time scales noise, as shown in Figure 4.1. Other than these spatial and temporal smoothing, we did not use any filtering method, which explains why the Rossby waves signal is not a pure signal on Figure 4.1 and 4.2. Using the RT approach method enhances our confidence in the presence of Rossby waves since we are able to detect them without the need for specific subjective filters. Then, a two-dimensional Radon Transform (2D-RT) as defined by Deans (1983) and Challenor et al. (2001) was applied to this Hovmöller diagram. The idea of this 2D-RT is to perform a rotation of the ($x = \frac{time}{\Delta t}, y = \frac{lon}{\Delta lon}$) dimensionless coordinates (Δt = 5 days, Δlon = 0.08°) by an angle φ before summing the SSH for each x' (x rotated) on all y' (y rotated). Thus, each (x',y') is associated to (x,y) as follows:

$$x = x^{'} \cos(\varphi) - y^{'} \sin(\varphi) \tag{4.1}$$

$$y = x^{'} \sin(\varphi) + y^{'} \cos(\varphi) \tag{4.2}$$

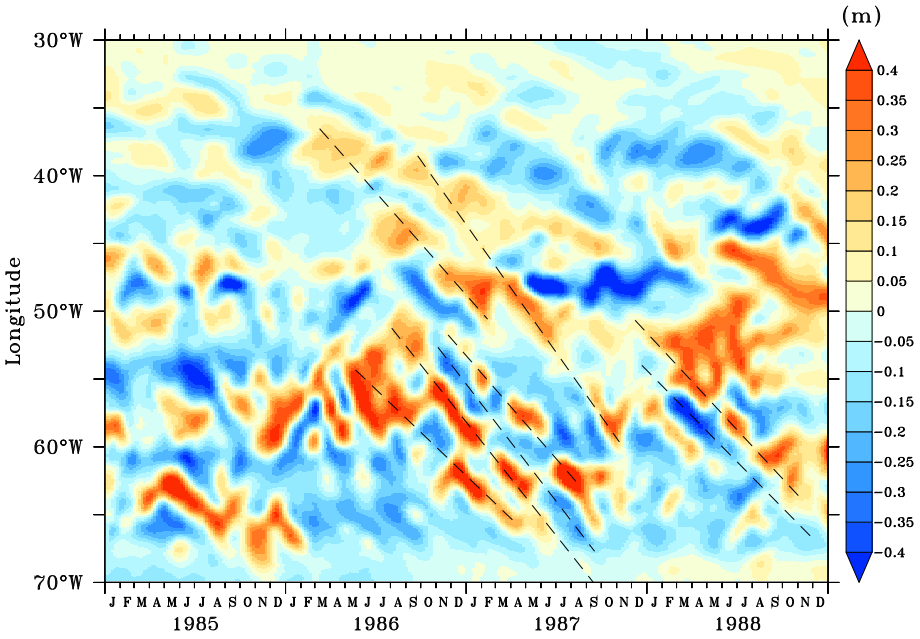

Figure 4.2: Hovmöller diagram (longitude–time) of detrended SSH anomalies at 39°N between 30–70°W and 1985–1988. A running average on 30 days and 28 km is applied. Black dotted lines represent possible examples of Rossby waves.

allowing the calculation of the 2D-RT from the SSH in Figure 4.1:

$$RT(\varphi, x^{'}) = \int_{y^{'}} SSH(x, y)dy^{'} \tag{4.3}$$

The 2D-RT is here computed for a set of angles φ ranging from 0 to 90° by steps of 1°. For each angle, we then computed the energy of the 2D-RT:

$$RTE(\varphi) = \int_{x^{'}} (RT(\varphi, x^{'}))^2 dx^{'} \tag{4.4}$$

The angle for which the 2D-RT energy is maximum is logically the one for which the maximum energy propagates westward.

4.3 Properties of the Rossby waves

Figure 4.3 shows the 2D-RT values for each time (x') and angle φ. The energy of this 2D-RT is shown in Figure 4.4, exhibiting a maximum when using an angle φ of 21°. In order to make sure that the peak at 21° is significantly different than the background noise, we generated 50 random noise fields and added them to the 2D-RT before recomputing its energy curve. The random fields extend between -2 and +2 standard deviations computed from the original 2D-RT. In 82% of the cases, the peak remained within 1° of 21°, while 98% were comprised within 2°. This angle

is consistent with the Rossby waves visually detected on Figures 4.1 and 4.2 (where an angle of 45° is defined as 0.08° in 5 days). Its speed can now be objectively estimated at $4.17\,\mathrm{cm\,s^{-1}}$.

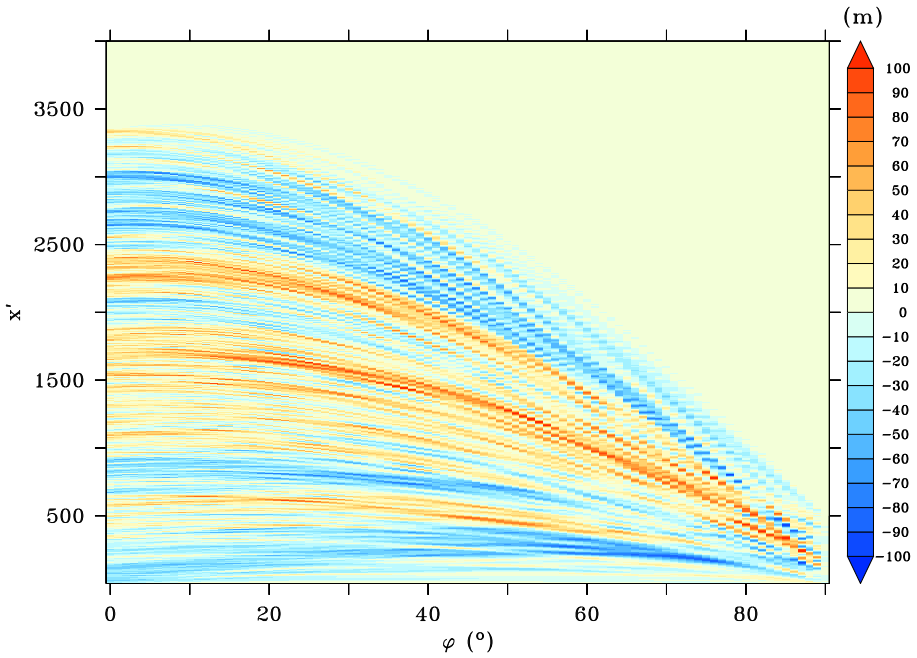

Figure 4.3: 2D-RT as defined in Eq. 4.3 computed on detrended SSH anomalies shown in Fig. 4.1, after applying 30-day and 28-km boxcar smoothings.

In order to compare this speed estimate with theory, we need to compute the Rossby wavenumber. Considering the RT at $\varphi = 21°$ (Figure 4.5), the first step in identifying this wavenumber is to perform a Fast Fourier Transform (FFT) on this 2D-RT, and then look for the leading period present in the signal. The first and last 5 years of the time series of the 2D-RT were removed beforehand to avoid edge effect. Figure 4.6 shows the power spectrum of this FFT for various periods between 0 and 2 years. The highest peak corresponds to a period of 269 days, while two other peaks can be seen at 190 and 467 days. The highest peak represents the first baroclinic Rossby wave and the following peak might correspond to contamination from higher order Rossby waves, although Maharaj et al. (2004) showed this last question remains open. In order to check the sensitivity of these periods against the angle of the RT, we carried out the same procedure for both RT angles of 20 and 22°. The resulting power spectra in Figures 4.7 and 4.8 confirm the highest peak around 269 days with virtually identical periods for the 3 main peaks.

From this leading period, the spatial wavelength is computed by projecting the period on the longitude axis of the Hovmöller diagram in Figure 4.1. This yields a wavelength of 13.37° corresponding to 1066 km at this latitude. Hence, the wavenumber is estimated at $5.878 \times 10^{-6}\,\mathrm{m^{-1}}$. The beta parameter β_0 is computed as follows:

$$\beta_0 = 2\frac{\Omega}{a}\cos(\alpha_0) \tag{4.5}$$

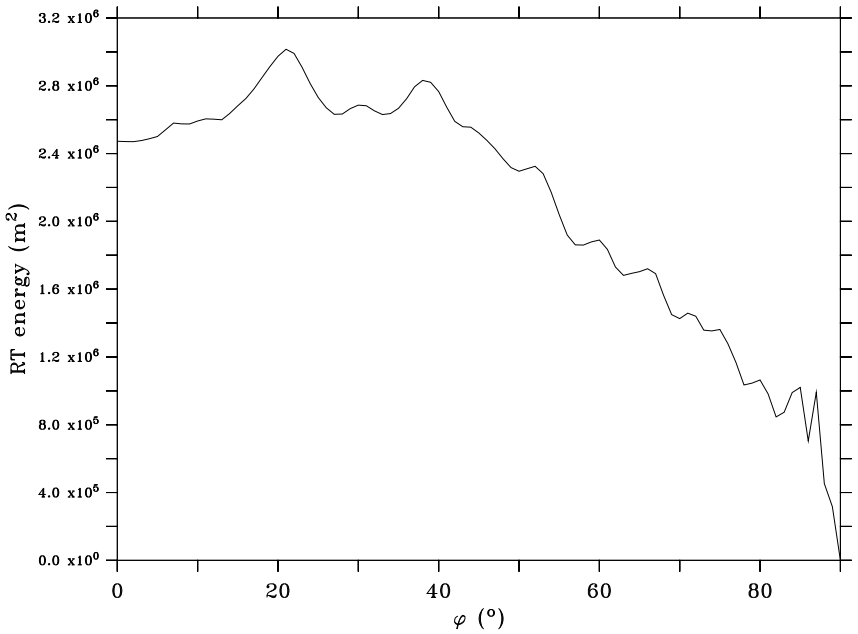

Figure 4.4: 2D-RT energy as defined in Eq. 4.4 computed on detrended SSH anomalies shown in Fig. 4.1, after applying 30-day and 28-km boxcar smoothings.

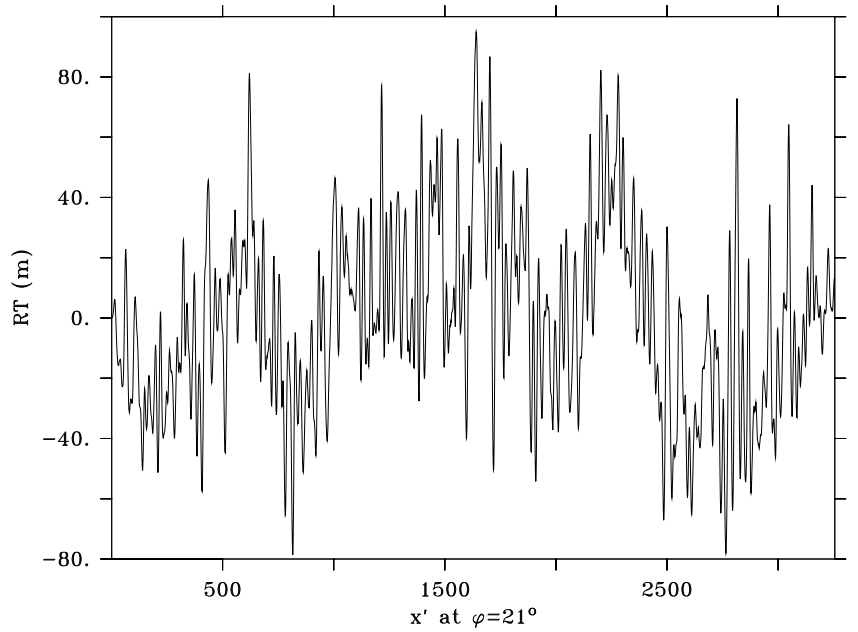

Figure 4.5: RT at $\varphi = 21^\circ$ extracted from Fig. 4.3.

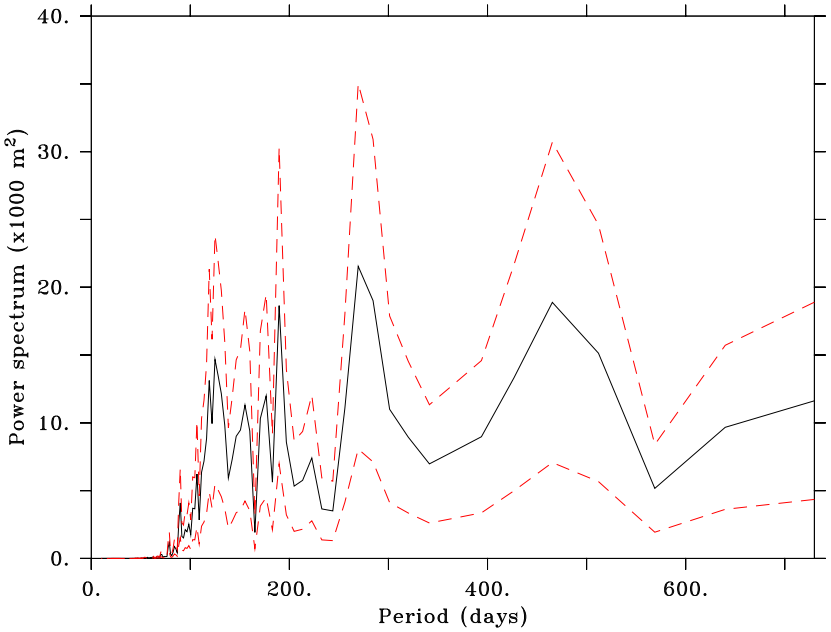

Figure 4.6: Power spectrum of the FFT applied to the RT at $\varphi = 21°$ for periods ranging between 0–2 years. Between both dashed red lines, an uncertainty of two standard deviations is shown.

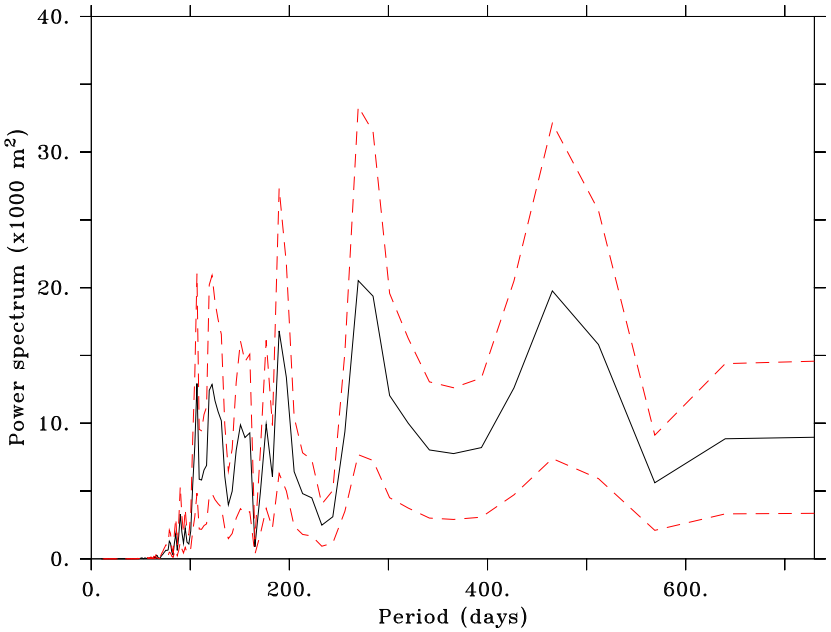

Figure 4.7: Power spectrum of the FFT applied to the RT at $\varphi = 20°$ for periods ranging between 0–2 years. Between both dashed red lines, an uncertainty of two standard deviations is shown.

where Ω is the angular speed of the Earth's rotation (7.29×10^{-5} rad/s), a is the Earth's radius (6371 km) and α_0 the latitude of the wave (39°N). In this case, β_0 equals $1.77 \times 10^{-11}\,\mathrm{m^{-1}\,s^{-1}}$.

The first baroclinic Rossby radius of deformation R is then estimated following the atlas published by Chelton et al. (1998). In the GS region, R is close to 30 km which is thus used in the calculation hereafter.

For this set of parameters, one can show that the group speed computed from our Radon analysis should be similar to the corresponding phase speed. Indeed, the dispersion relation of the Rossby waves reads:

$$\omega = -\beta_0 R^2 \frac{k_x}{1 + R^2(k_x^2 + k_y^2)} \tag{4.6}$$

and the zonal phase speed that follows:

$$c_x = \frac{\omega}{k_x} = \frac{-\beta_0 R^2}{1 + R^2 k_x^2} \tag{4.7}$$

where we used $k_y = 0$. From these equations, the group speed is defined as:

$$c_{xg} = \frac{\partial \omega}{\partial k} = -\beta_0 R^2 \frac{1 - 2R^2 k_x^2}{1 + R^2 k_x^2} \tag{4.8}$$

which is close to c_x provided we use typical values of $\sim 10^{-6}\,\mathrm{m^{-1}}$ for k_x and $\sim 10^4\,\mathrm{m}$ for R, since $2R^2k_x^2$ is then negligible when compared to 1.

We can thus consider the speed computed from our Radon analysis as a phase speed, and compare it with the theory using the parameters above and the equation 4.7. This yields a theoretical phase speed of $1.55\,\mathrm{cm\,s^{-1}}$, 2.7 times weaker than our empirical estimate.

Such a discrepancy between theory and practical estimates of baroclinic Rossby wave speeds have been encountered by many authors (e.g. Chelton & Schlax, 1996; Osychny & Cornillon, 2004; Maharaj et al., 2004). At 39°N, Osychny & Cornillon (2004) found a factor of discrepancy slightly larger than ours. The standard theory was accordingly adjusted by Killworth et al. (1997) and updated by Killworth & Blundell (2003, 2004, 2005) to account for the effects of the baroclinic background mean flow and topographic gradients, the former being generally dominant according to Maharaj et al. (2007). As reported by Killworth et al. (1997), the discrepancy factor between observed speeds and those predicted by standard theory reaches 2 poleward of 30°N. Besides, their estimated maximum ratio between standard and extended theory reaches 3 at 39°N, which is consistent with our estimate of 2.7.

4.4 Summary and discussion

This study shows that it is possible to detect Rossby waves at latitudes compatible with the average position of the GS while using long time ranges covering pre-altimetry era, provided sufficiently resolved numerical simulations are used. The methodology described here was applied to 1/12° SSH outputs from the DRAKKAR project, but it can easily be adapted for other models or variables. In particular, it would be instructive to examine the sensitivity of the Rossby waves detection to an even finer spatial resolution.

Following the state of the art, the time lag between a specific NAO phase (+ or –) and its consequence on the GS path and transport still remains a question on which there is no perfect consensus at this stage. As a matter of fact, the bulk of estimates ranges between 0 and 2 years considering both GS path and transport (Watelet et al., 2017).

Considering the NAO signal transfers momentum through the wind stress to the central part of the NA (Visbeck et al., 1998), with a maximum impact on the SSH in this area (Esselborn & Eden, 2001), we use hereafter the longitude 30°W as a reference for the perturbation initiating a westward SSH Rossby wave. In order to compare with GS indices from Watelet et al. (2017) established by considering EOF's computed on 81 equally spaced longitudes between 70°W and 50°W, we use the longitude 60°W as representative of the place where the incoming Rossby wave would impact the characteristics of the GS. These assumptions leads to 30° to be travelled westward at the latitude 39°N. Using our phase speed estimate of $4.17\,\mathrm{cm\,s^{-1}}$ or $15.22\,^{\circ}\,\mathrm{yr^{-1}}$ yields a travel time of 1.97 years (∼24 months), which is consistent with usual NAO–GS delays.

Still, the major part of GS indices are computed on a yearly basis, for both position and transport, which leaves room for deeper investigation. We thus used the monthly GS Delta index (GSD, proxy for its transport) from Watelet et al. (2017), already averaged on running 12 months, and used their monthly GS North Wall index (GSNW, representative of its position) that we averaged the same way. This allows the computation of correlations with NAO using monthly time lags, as shown in Figure 4.9. Looking at delays at a resolution of 1 month instead of 1 year is necessary in order to allow an accurate comparison with the Rossby wave speeds. The NAO indices we use in this Section are the Hurrell annual or monthly NAO index, both based on an EOF analysis of the sea level pressure over the NA (see National Center for Atmospheric Research Staff, 2015; Hurrell, 1995; Hurrell et al., 2003; Hurrell & Deser, 2010; Trenberth & Hurrell, 1999). Both are available online (at `https://climatedataguide.ucar.edu/climate-data/hurrell-north-atlantic-oscillation-nao-index-pc-based`).

The correlations are shown for the period 1960-2014, chosen as the longest reliable period for the GSD index. The NAO–GSD correlation peaks at time lags of 1 and 29 months, possibly indicating the influence of a fast barotropic Rossby wave followed by its slower baroclinic counterpart, in accordance with De Coëtlogon et al. (2006). Although this last delay is consistent with the baroclinic waves we detected, the interpretation of the NAO–GSNW correlations remains unclear, with significant correlations between 3 and 14 months, peaking at 7 months. Nevertheless, the exact

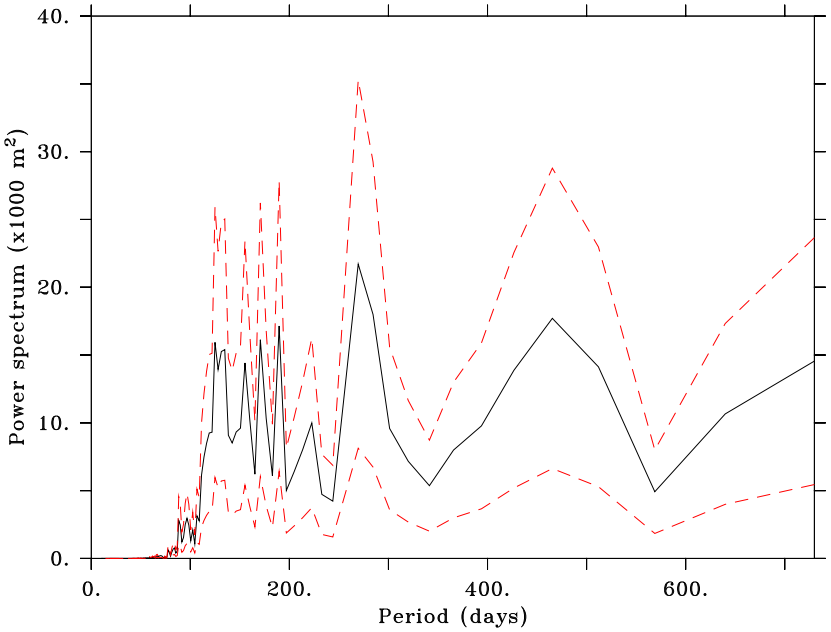

Figure 4.8: Power spectrum of the FFT applied to the RT at $\varphi = 22°$ for periods ranging between 0–2 years. Between both dashed red lines, an uncertainty of two standard deviations is shown.

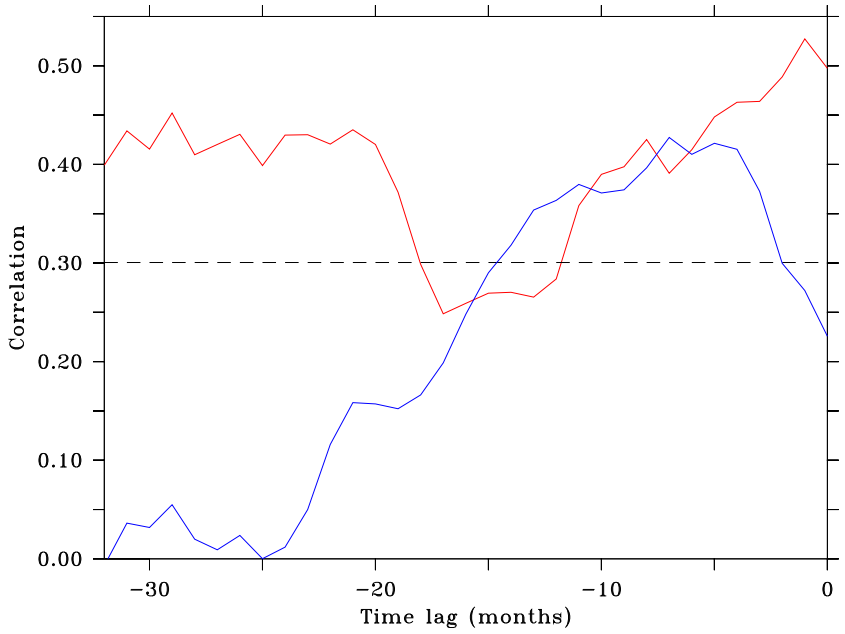

Figure 4.9: Correlations between monthly NAO–GSD (red) and NAO–GSNW (blue) for time lags ranging between 0 and 32 months. The black dotted line shows the significance threshold at a 95% confidence level.

value of this time lag is still discussed and depends on methods, periods and data used (e.g. Taylor & Stephens, 1998; Joyce et al., 2000; Watelet et al., 2017).

Apart from the influence of westward Rossby waves, another mechanism was proposed to account for the GSNW shifts: the fluctuations in the southward flow of Labrador Sea water might impact the GS path (Rossby, 1999). Hameed & Piontkovski (2004) even suggested this last mechanism to be preponderant against the influence of the NAO through Rossby waves, by showing the Icelandic Low has a dominant influence on the GSNW while the Labrador Sea wind stress is mainly connected to the same Icelandic Low. While outside the scope of this paper, this second mechanism might explain our difficulties to find a straightforward link between the NAO and the GSNW.

Finally, in order to further explore the link between the NAO and the baroclinic Rossby waves, we compare the monthly NAO index to the RT at $\varphi = 21°$ between 1970–2012. As a reminder, the RT computation is based on the sum of the SSH of a Hovmöller diagram along the spatial axis progressively tilted to the left as the angle φ increases. We assigned time values to the RT by considering the approximate moment at which the wave is generated by the NAO signal, i.e. we attributed the time corresponding to 30°W for a particular SSH wave. In other words, we projected the axis x' on the original time axis x to get a time series from the RT at $\varphi = 21$. This explains why we had to somewhat shorten the original 1970–2015 period. Then, we smoothed both signals by using a 9-month running average, and normalised them to get Figure 4.10. This smoothing length is chosen as the estimated period of Rossby waves. The positive correlations between unsmoothed NAO and RT (not shown) and between both smoothed indices are not significant. Nevertheless, there are visual similarities between smoothed NAO and SSH waves, especially looking at multi-year time scales. Besides, we show in Figure 4.11 that the direct correlations between NAO and SSH between 50–30°W and 1970–2015 exhibit small peaks at time lags increasing westward (red line), consistently with the hypothesis of the NAO generating a Rossby wave around 30°W. The linear regression (black dashed line) between these peaks is significant and reveals a Rossby wave speed of $12.67\,^\circ\,\mathrm{yr}^{-1}$ or $3.47\,\mathrm{cm\,s}^{-1}$, which is close to our previous estimate (black solid line). While the correlations are not significant, the figures are nevertheless interesting. These weak correlations are an argument to encourage further research in the physical processes linking NAO and Rossby waves. In particular, the connection between a specific NAO phase and the generation of oceanic Rossby waves has been rather neglected so far and thus requires more numerical experiments, such as sensitivity tests of Rossby waves intensity to various wind stress forcings.

4.5 Code and data availability

The code used to perform the DRAKKAR simulations is available at 10.5281/zenodo.3968307. The data sets used in this study are available at 10.5281/zenodo.3968801 and 10.5281/zenodo.3968885.

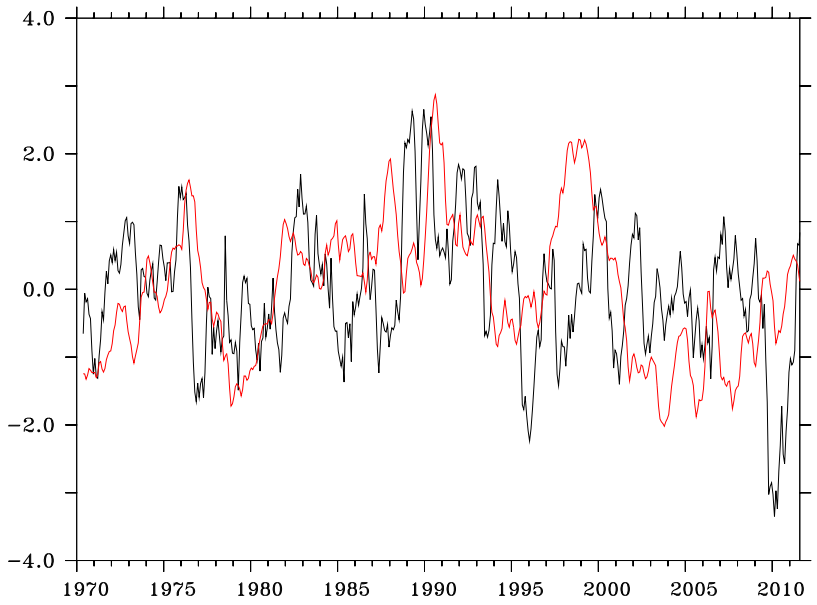

Figure 4.10: Normalised NAO index (black) and RT at $\varphi = 21$ (red) between 1970–2012. A 9-month smoothing was applied on both indices.

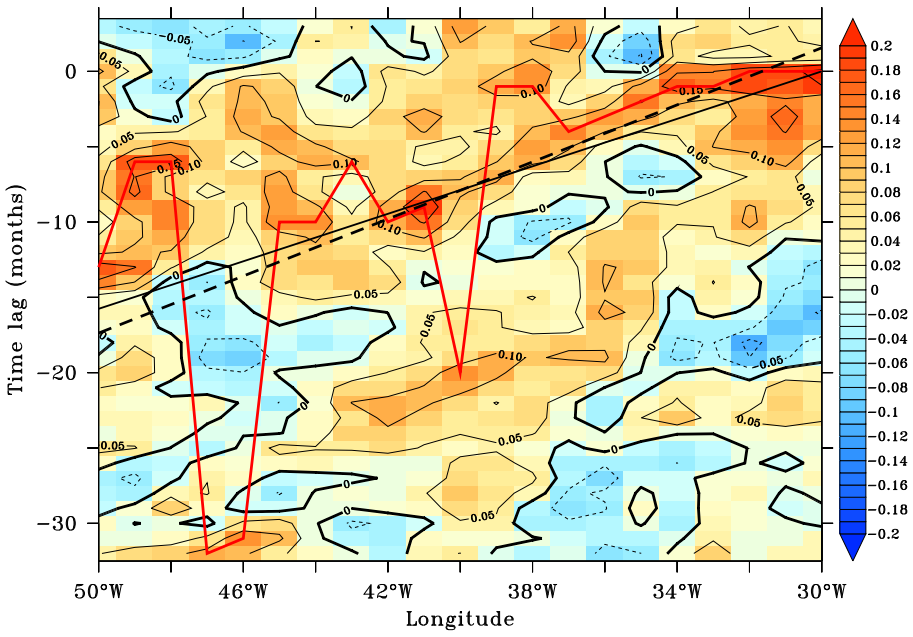

Figure 4.11: Correlations between monthly NAO index and DRAKKAR SSH between 1970–2015 for time lags ranging from -32 to +3 months (negative lags means NAO precedes SSH) and for longitudes between 50–30°W. The red line shows the maximum correlation for each longitude, while the black dashed line is its linear regression with a slope of $0.947\,\mathrm{mth}^{\circ-1}$ corresponding to a propagation speed of $12.67^{\circ}\,\mathrm{yr}^{-1}$. The black solid line corresponds to our estimated Rossby wave speed from RT (see previous Sections).

Chapter 5

Atlantic water inflow and deep water formation in the Barents Sea

Contents

Preliminary remark

Most of this Chapter was published in Watelet, Skagseth, Lien, Sagen, Østensen, Ivshin & Beckers (2020b).

5.1 Introduction

The Barents Sea shelf is a "hotspot" in the ongoing, rapid climatic changes taking place in the Arctic (Lind et al., 2018). During recent decades, the Barents Sea has contributed most of the reduction in Arctic winter sea-ice cover (Yang et al., 2016). Moreover, the northern, Arctic–dominated part of the Barents Sea has experienced an "Atlantification" (or "borealization") with profound impact on its physical conditions, such as water mass transformations and properties (Lind et al., 2018), as well as on biology and marine ecosystem (Fossheim et al., 2015). As the northern limb of the Atlantic Meridional Overturning Circulation (AMOC) and a source for dense Arctic Intermediate Water (Schauer et al., 1997), changes to the water mass transformation processes in the Barents Sea affect the thermohaline circulation of the North Atlantic and Arctic oceans (Swift et al., 1983; Kuhlbrodt et al., 2009; Mauritzen et al., 2013; Lozier et al., 2019).

The Barents Sea is the largest shelf sea of the Arctic Ocean, and it is bounded by Norway and the Kola Peninsula (Russia) to the south, the Svalbard and Franz Josef Land archipelagos to the north, and Novaya Zemlya to the east (see Fig. 5.1). The Barents Sea is connected to the Norwegian Sea to the west through the Barents Sea Opening (BSO), and to the Arctic Ocean to the north and northeast. Together with the Fram Strait between Svalbard and Greenland, the BSO is the main gateway between the North Atlantic and the Arctic and, thus, a main pathway for Atlantic Water transport northwards from the Nordic Seas to the Arctic Ocean (Knipowitsch, 1905; Helland-Hansen & Nansen, 1909). Due to its climatic importance and vast marine resources, the Barents Sea area is sampled and monitored on a seasonal timescale (Eriksen et al., 2018). However, the coverage varies between seasons and years, especially during winter and spring, and the spatial coverage is sometimes only semi-synoptic or concentrated at fixed sections.

Satellite remote sensing provides observations of sea surface temperature, and recently sea surface salinity, with high resolution in both space and time. For example, using AVHRR data, Comiso & Hall (2014) found the northern Barents Sea to be one of the areas within the Arctic that shows the highest temperature increase for the period 1981–2012. Furthermore, they found a significant decline in sea-ice cover between the two periods: 1979–1995 and 1996–2012. However, to investigate regional climate processes, such as water mass transformation and property changes, *in situ* observations are needed. *In situ* data often have disadvantages of a limited coverage in space (e.g. repeated hydrographic sections) and/or time (e.g. ship surveys). Thus, providing these observations on a regular grid is desirable in order to examine spatio-temporal changes.

Here, we present a gridded dataset of temperature and salinity in the Barents Sea region at seasonal temporal resolution for the period 1965–2016, based on all available *in situ* observations. The dataset is compiled using the Data-Interpolating Variational Analysis (DIVA) tool. We provide the dataset including fields of expected error, and present two examples of usage where this gridded dataset has an advantage over the non–gridded raw data: volumetric analysis of water mass characteristics, and estimation of ocean heat and freshwater content.

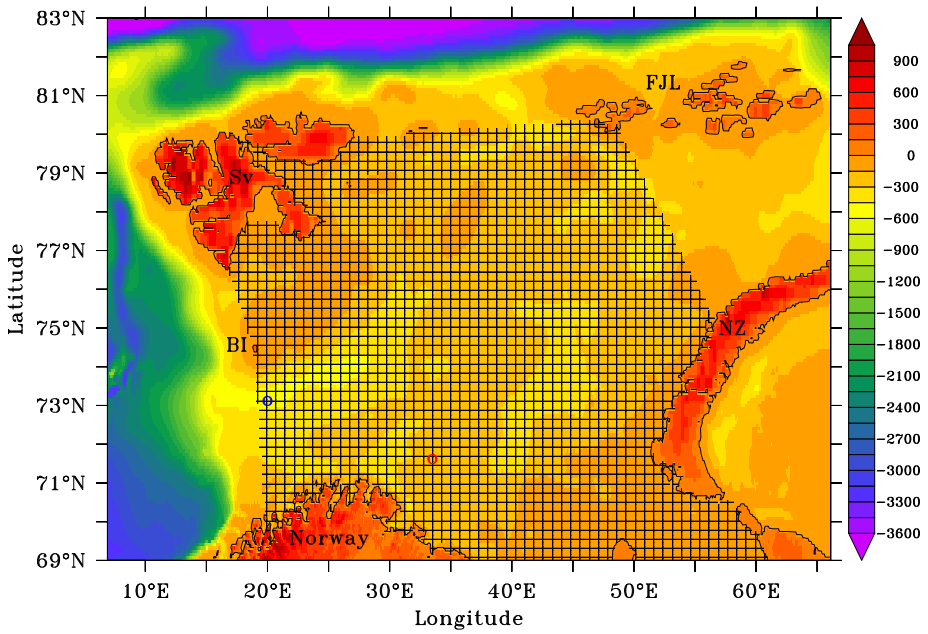

Figure 5.1: Bathymetry of the Barents Sea and its neighbouring seas. Our analyses on the Barents Sea correspond to the shaded region. The Barents Sea Opening, located between the Norwegian coast and Bear Island, and the Kola sections are shown as blue and red circles respectively. BI stands for Bear Island, Sv for Svalbard, FJL for Franz Jozef Land and NZ for Novaja Zemlja.

5.2 Data sources

In situ hydrographic data were obtained from three different sources, the World Ocean Database 2013 (WOD13), the Norwegian Polar Institute, and the Polar Branch of Russian Federal Research Institute of Fisheries and Oceanography (PINRO). The data consist mostly of Conductivity-Temperature-Depth (CTD) cast profiles, while data from the pre-CTD era (ca. mid–1970s) consist of Salinity-Temperature-Depth (STD) cast profiles as well as discrete samples. Expendable bathythermograph (XBT) data are also included. Data from CTD are usually provided at a vertical resolution of 1 meter, while some profiles are provided at a vertical resolution of 5 meters. Discrete samples are provided at standard depths where the vertical resolution varies with depth and increases from 5 meters near the surface to 50 meters near the bottom depth in the Barents Sea (around 200-300 m).

The hydrographic data obtained from WOD13 included data until 2016 and were limited to the area 7°E–66°E, 68°N–83°N. Only data with a quality control flag value of 0 (i.e., accepted cast) were included.

Hydrographic data from the Norwegian Polar Institute, which are not included in the WOD13 database, include CTD casts from 1998, 2003, 2004, 2005, and 2011. These data only included post-processed, quality-controlled data with a quality flag value of 1 (“good data”).

From the hydrographic data obtained from PINRO, which cover the period 1965-2014, only data with a quality control flag value of 1 (“good data”) were included. These data complement CTD data from the Institute of Marine Research already

available from the WOD13 with respect to geographical coverage from joint surveys in winter and summer.

The data coverage is usually better in the spring (Feb-Mar-Apr) and autumn (Aug-Sep-Oct) seasons compared with the rest of the year due to extensive survey activity during these seasons. However, while the surveys generally cover the ice-free area of the Barents Sea, the spatial coverage vary between years and the coverage is usually more extensive in the autumn compared with the spring. Moreover, while data from the annual spring and autumn surveys in the Barents Sea are obtained on a regular grid, data from other surveys are more focused in smaller areas or along fixed sections.

5.3 Software and method

Ocean Data View (ODV) software was used to convert the hydrographic data files into a format readable by the DIVA software, the ODV spreadsheet (`https://www.bodc.ac.uk/resources/delivery_formats/odv_format/`).

DIVA is a statistical software designed to generate continuous fields from heterogeneously distributed *in situ* data using a Variational Inverse Method (Brasseur, 1995; Troupin et al., 2012). The result of its variational analysis are gridded fields which minimise the expected errors with respect to the unknown true fields. Under a few assumptions on the correlations, the Variational Inverse Method (VIM) is equivalent to the popular Optimal Interpolation (Rixen et al., 2000). In practice, the aim of the VIM is to minimize the following cost function J:

$$J\left[\varphi\right] = \sum_{j=1}^{N_d} \mu_j \left[d_j - \varphi(x_j, y_j)\right]^2 + ||\varphi||^2$$

where the N_d observations d_j are used to reconstruct the analysed field φ and with

$$||\varphi||^2 = \int_D (\alpha_2 \nabla\nabla\varphi : \nabla\nabla\varphi + \alpha_1 \nabla\varphi.\nabla\varphi + \alpha_0\varphi^2) dD$$

where α_0 penalizes the field itself (anomalies with respect to a reference field, e.g., a climatological average), α_1 penalizes gradients (no trends), α_2 penalizes variability (regularization), and μ_j penalizes data-analysis misfits (objective analysis) (Troupin et al., 2016).

Unless specified otherwise, we always use the command line version of DIVA in this study. This version comes with the full set of options, for instance regarding the optimization of the statistical parameters later used in the analyses.

Then, using DIVA preprocessing tools, the data were vertically interpolated onto 23 depths (500, 450, 400, 350, 300, 250, 200, 175, 150, 125, 100, 75, 50, 45, 40, 35, 30, 25, 20, 15, 10, 5, 0) following the Weighted Parabolas method (Reiniger & Ross, 1968). These levels were chosen in view of increasing the resolution next to the surface where the variability of both temperature and salinity are expected to be higher.

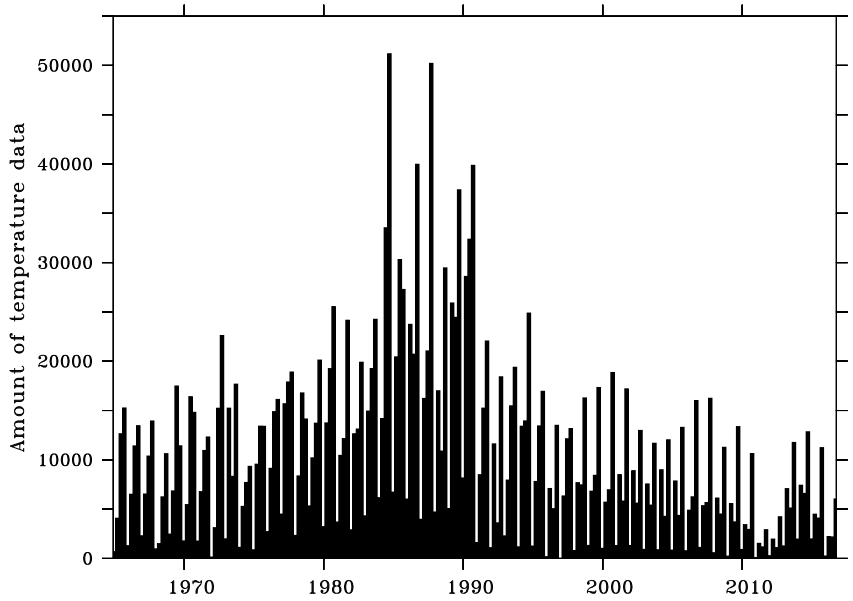

Figure 5.2: Availability of temperature data in the Barents Sea as a function of time (seasons).

The Barents Sea bathymetry to be used in the atlas processing was extracted from the General Bathymetric Charts of the Oceans (GEBCO) at a spatial resolution of 30 seconds by using Diva-on-web (`http://ec.oceanbrowser.net/emodnet/diva.html`). This bathymetry was then smoothed to a resolution of 1/8° by using a 2D convolution low-pass filter followed by a linear interpolation to avoid too complex shapes when computing the coastlines for each depth level. Besides, several fjords were removed from the bathymetry. All the interpolated data falling outside these smoothed coastlines or outside the full domain (6.9–66.1°E ; 69–83°N) shown in Fig. 5.1 were removed. A data range check was also performed and excluded temperature data falling outside -1.9–20° C and salinity data outside 30–36. The remaining data availability per season is shown in Fig. 5.2 for temperature and in Fig. 5.3 for salinity.

For each of the 23 depth levels, the objective is to perform one analysis for each season and for each year between 1965–2016. Based on data availability from regular cruise activity, we chose the seasons as follows: November to January (winter), February to April (spring), May to July (summer) and August to October (autumn). The first season is thus November 1964 to January 1965, the last being August to October 2016. The analysis is carried out in two steps. A reference field, or a first guess state, needs to be created before each analysis is carried out. The reference fields are created by collecting all data for each season across 11 years centred around the year to be analysed. A moving window centred at the year of interest is used due to the strong multidecadal variability of the region (e.g. Smedsrud et al., 2013). Near the beginning and end of the period the window size is reduced to the available years (i.e., the reference field for 1965 is based on data from the period 1965–1970). The horizontal average is used as a constant first guess when creating the reference fields. Therefore, 4 reference fields are generated per year, that is one per season. By subtracting the reference field from the original data, DIVA

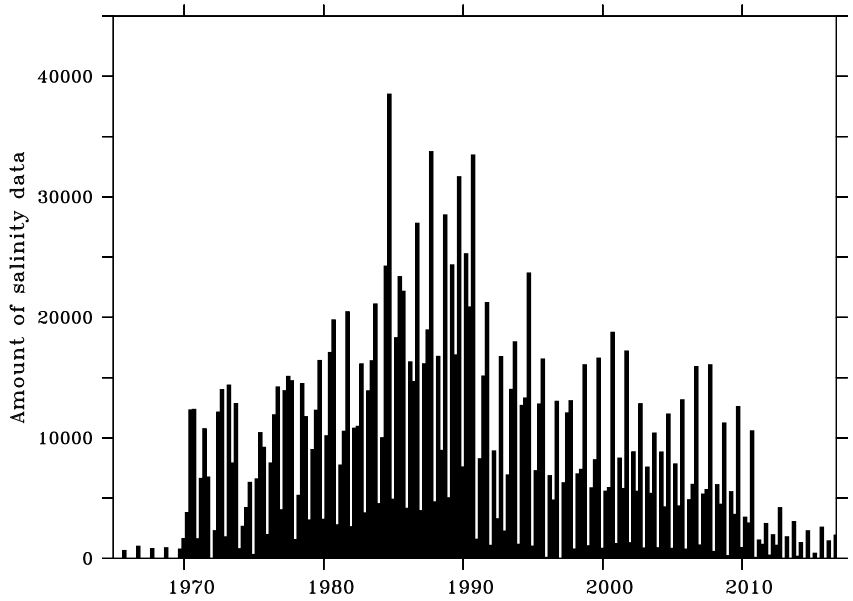

Figure 5.3: Availability of salinity data in the Barents Sea as a function of time (seasons).

directly works with anomalies of temperature and salinity before adding back the reference to the optimal analysis. In this way, the analysis tends to smoothly reach the reference values in the absence of data.

In the reference fields, the correlation length is estimated by a fit between the empirical data correlation function as a function of the distance and its theoretical counterpart, while the signal to noise ratio is approximated by cross validation techniques (Craven & Wahba, 1978). Both the correlation length and the signal-to-noise ratio are thus estimated on the basis of the data sets. Moreover, they are both filtered vertically to avoid unrealistic discontinuities between depth levels. To avoid an overconfidence in the data accuracy, the signal-to-noise ratio is capped at 10 for salinity and 3 for temperature, because of its higher temporal variability. Using these statistical parameters, the reference fields are computed by the Variational Inverse Method with DIVA over the same 11 years, for each season.

Then, each analysis is performed using the corresponding 11 year-reference field and the associated statistical parameters. We decided to use the statistical parameters based on the larger amount of data (11 years) in order to increase their robustness and decrease their variability. For temperature, a logit transformation was applied on data beforehand, so as to ensure the results are constrained between -1.9 and 20°C after applying a reciprocal function to the analyses. This extra precaution for temperature is justified by the sea ice formation around -1.9° C. The analyses are stored on an output grid with a resolution of 0.1° in latitude and 0.25° in longitude. Other atlas products, such as the WOA, are also provided on regular lat-lon grids, as well as most operational ocean models. Hence, it makes some of the usages more straightforward.

In order to assess the reliability of the analyses, an error field associated with each of them is computed by using the clever poor man's method, a good compromise between the computation time and the accuracy (see Beckers et al. (2014)). The

poor man's error is computed by analysing a "data" vector with unit values and is very cost-effective (Troupin et al., 2010), but the error field is too optimistic. It is shown that using the same method with a correlation length divided by a factor ~ 1.7 requires a similar computation time and yields a more realistic estimate of the error, that is, the clever poor man's error. This analysis error is then compared to the first guess error, and the ratio of those errors yields the relative error field which thus consists in a value between 0 and 1. Qualitatively, this figure measures the added value brought by *in situ* data to the analysis: 0 would be the true field while 1 corresponds to an absence of data, that is an analysis equal to the first guess.

5.4 Temperature and salinity atlas

The temperature and salinity atlas is available at the Norwegian Marine Data Centre as two NetCDF files. Each file contains analyses of temperature or salinity, respectively, for all seasons and years at all depths, and also includes the error field associated with each analysis. The statistical parameters (correlation length and signal to noise ratio) and the analysed fields restricted to the most reliable areas are also available. These latter analyses are masked if the relative error exceeds 0.3 or 0.5. As shown in Fig. 5.2 and 5.3, there are several seasons with data gaps. In such cases, the atlas only contains a missing value, for both the analysis and the error field. The data gaps for salinity are mainly found before 1970 and after 2010, while the temperature has only exceptional data gaps. Between 1970–2010, there are data gaps in the salinity atlas during the 1971—1972 winter period and in both temperature and salinity atlas during the 1996–1997 winter period. Besides, other gaps appear sometimes in the deepest layers. In Section 5.5, we explain how to make use of the error field to take into account the data coverage before applying any analysis. The data is accessible at 10.21335/NMDC-2058021735 (Watelet et al., 2020c).

The hydrographic atlas presented here complements global gridded data products, such as the World Ocean Atlas (Locarnini et al., 2018; Zweng et al., 2018), by providing a regional approach tailored to the specific region by offering a higher spatiotemporal resolution allowed by the higher regional data coverage. The presented gridded dataset provides researchers with readily available observation-based data, including error estimates, for several key purposes, such as numerical ocean model validation and regional climate studies. While point-based observations are useful for process studies and observation-model comparisons, a gridded dataset enables the researcher to easily conduct spatiotemporal analysis, such as empirical-orthogonal-function (EOF) analysis for a more robust measure of a numerical model's performance (e.g. Wang et al., 2014). Furthermore, a gridded dataset enables easy computation of integrated measures such as ocean heat content and ocean freshwater content (e.g. Lind et al., 2018), area covered by specific water masses (e.g. Johannesen et al., 2012), or overall changes in water mass characteristics (e.g. Skagseth et al., 2020) for regional climate studies.

5.5 Uncertainties and use of error field

In the following sections we demonstrate how the error field provided in the atlas can be utilized to objectively limit the data in time or space before applying the desired analysis. Moreover, we give some examples of possible usages of the atlas product.

5.5.1 Most reliable period

Lind et al. (2018) provided some evidence suggesting a warmer and saltier northern Barents Sea since the mid–2000s. Here, we show the changes in water mass characteristics in the whole Barents Sea based on the results from the atlas, by use of volumetric Temperature–Salinity (T-S) diagrams. We limit our analysis to comparing the two 5-year periods 1994–1998 and 2006–2010, where the former represents a relatively cold period while the latter represents a warm period relative to the last 50 years.

First, we consider uncertainties by investigating the error field from the atlas. As the data coverage in the Barents Sea varies between years, seasons and sub-regions, the error field varies accordingly (Fig. 5.4). The geographical patterns of the error fields are similar at other depths (not shown). Generally, the errors are larger in the northern and eastern parts of the Barents Sea compared with the western and southern parts, due to differences in data coverage (see Section 5.5.2; Fig. 5.4; Supplementary Material). Moreover, the data coverage is generally better in the autumn season and, hence, the error is generally smaller compared with the other seasons. For this reason, we decided to focus on the autumn only when considering the whole Barents Sea. For studies needing the whole Barents Sea climatology in other seasons (e.g. winter), other data sources could prove necessary.

Volumetric T-S diagrams for both 1994–1998 and 2006–2010 were compiled by summing all the pixels falling inside the T-S classes defined by temperature ranging from -1 to 7 °C and salinity varying between 33 and 35.5, using steps of 0.05 °C and 0.025, respectively. In this calculation, each pixel is weighted by its vertical extent for each corresponding layer to get a proportional representation of to the water volume within each T-S class. Moreover, the horizontal extent of each pixel is weighted by the latitude φ relative to the average latitude φ_0 of all the grid cells, due to the narrowing of the longitudinal bands towards the north, using the function

$$Weight = \frac{\cos\varphi}{\cos\varphi_0}.$$

The average T-S properties in both periods is shown in Fig. 5.5a, while the difference between the two periods is shown in Fig. 5.5b. Clearly, both the temperature and the salinity increased, on average, from the 1990s to the 2000s in the whole Barents Sea, which is in line with the findings of, e.g., Skagseth et al. (2020). Between the T or S classes showing the highest change, there is temperature shift of 5° C and a salinity shift of 0.2. The density, however, remained more or less unchanged due to the cancelling effects of increasing haline contraction and thermal expansion on density, again consistent with the findings of Skagseth et al. (2020).

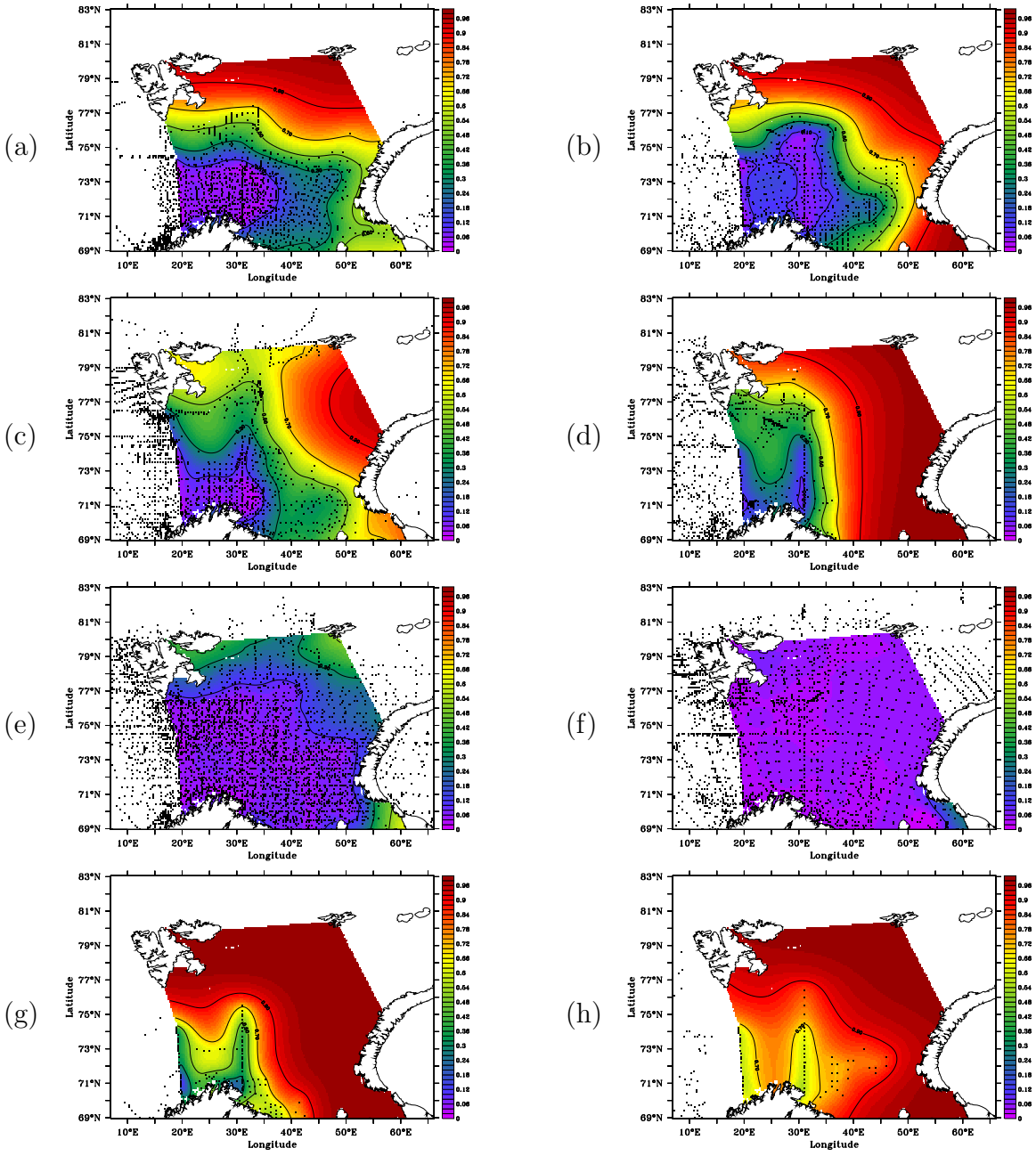

Figure 5.4: Average relative error for temperature at the Barents Sea surface between 1994–1998 (left column) and 2006–2010 (right column) between 1994–1998. (a) and (b) correspond to spring, (c) and (d) to summer, (e) and (f) to autumn, (g) and (h) to winter. This variable measures the added value brought by *in situ* data to the analysis: 0 would be the true field while 1 corresponds to an absence of data, that is an analysis equal to the first guess. The winter 1996–1997 was excluded from the computations due to a lack of data.

Further utilizing the error field, we provide an estimation of the uncertainties for both the two 5-year periods included in the above analysis. Comparing the error fields in both periods (Fig. 5.5c, d) with the changes in the T-S properties between the two periods (Fig. 5.5b), as well as the T-S diagrams of both periods (Fig. 5.5a), it is clear that the error is small for the T-S classes that have the largest presence and also are showing the largest changes. This strengthens the reliability of the findings of T-S changes in the Barents Sea in autumn.

5.5.2 Most reliable area

In this Section, we focus on the spatial pattern of the error field. We first limit our study area to the area where the average relative error for temperature is less than 0.5 (Fig. 5.6), hereafter referred to as the Most Reliable Area (MRA). Similarly to Section 5.5.1, salinity and temperature exhibit close relative error fields (not shown). We then average the relative error fields for all seasons (see Supplementary Material). Compared to the rest of the Barents Sea, the MRA shows relatively low uncertainties for all seasons due to the better data coverage. The MRA encompasses the southern part of the Barents Sea which is dominated by the Atlantic Water inflow and kept ice-free year round, hence the better data coverage in all seasons. This allows us to analyze all the seasons in the MRA, in contrast to only the autumn season when analyzing the whole Barents Sea (see section 5.5.1), with the exception that for salinity the data coverage is sufficient only for the period 1970—2010. For temperature, we use the period 1965–2015. In addition, there are gaps in the salinity data during the 1971—1972 winter period and in both temperature and salinity data during the 1996–1997 winter period.

We start the analysis of the MRA by investigating the water mass characteristics within the region represented by vertical profiles of temperature and salinity averaged over the MRA and for each season (Figs. 5.7, 5.8). The temperature gradually increased throughout the whole water column during the period 1965–2015, by 1.74° C on average. For salinity, matters are not so clear, except the unambiguous average increase of 0.11 between 1990–2010, similarly to the observation made for the whole Barents Sea between the 1990s and the 2000s. The potential density relative to the surface is shown in Fig. 5.9. There is no clear trend throughout the period, which indicates that the observed warming trend is compensated to some extent by a salinity increase. This result is consistent with the changes in the Barents Sea hydrographic properties reported by Skagseth et al. (2020) and also upstream in the Norwegian Sea (Mork et al., 2019).

Further analyses of volumetric changes in the MRA are performed in order to better assess the evolution of temperature, salinity and density classes throughout the water column. The calculations follow a method similar to Section 5.5.1 and are performed for each season between 1965–2015 for temperature and between 1970–2010 for both salinity and density. The aim is to show the relative volume occupied by each temperature and salinity class. Fig. 5.10 shows the evolution of temperature classes ranging from -1 to +7 °C with a step of 1 °C. There is a clear increase in the volume of the warmest temperature classes at the expense of the coldest classes throughout the period. For instance, between the periods 1975–1985 and 2005–2015,

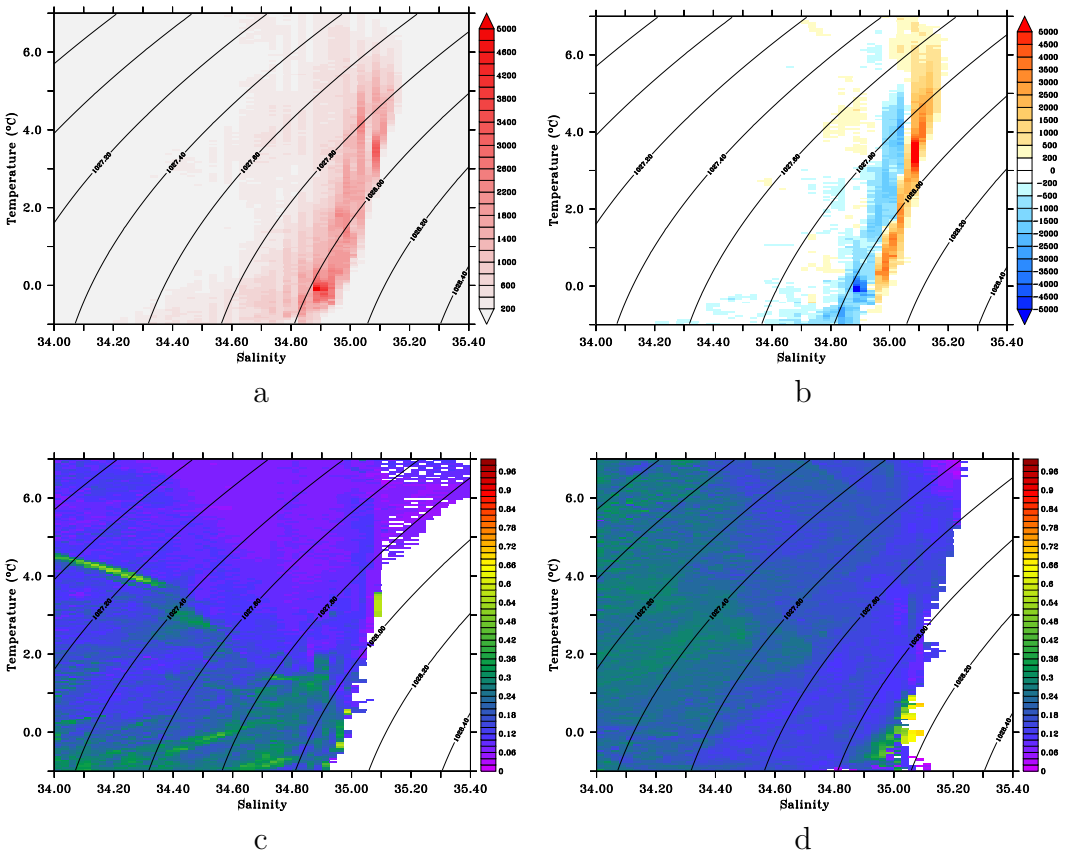

Figure 5.5: (a) Average of the volumetric T-S diagrams during both 1994–1998 and 2006–2010 periods. A value of 1 corresponds to a pixel with a vertical extent of 1 m at φ_0 =74.5°N, that is $8.26 \times 10^7\,\mathrm{m}^3$. Isopycnals are shown for 0 m (black). (b) Difference in volumetric T-S diagrams between 2006–2010 and 1994–1998. (c) Average relative error weighted by the layer thickness and the latitude for each T-S class between 1994–1998. (d) Average relative error weighted by the layer thickness and the latitude for each T-S class between 2006–2010. For all panels, only autumn is used and the areas with errors above 0.99 were excluded from the computations to avoid contamination by small areas without data and disconnected from the sea.

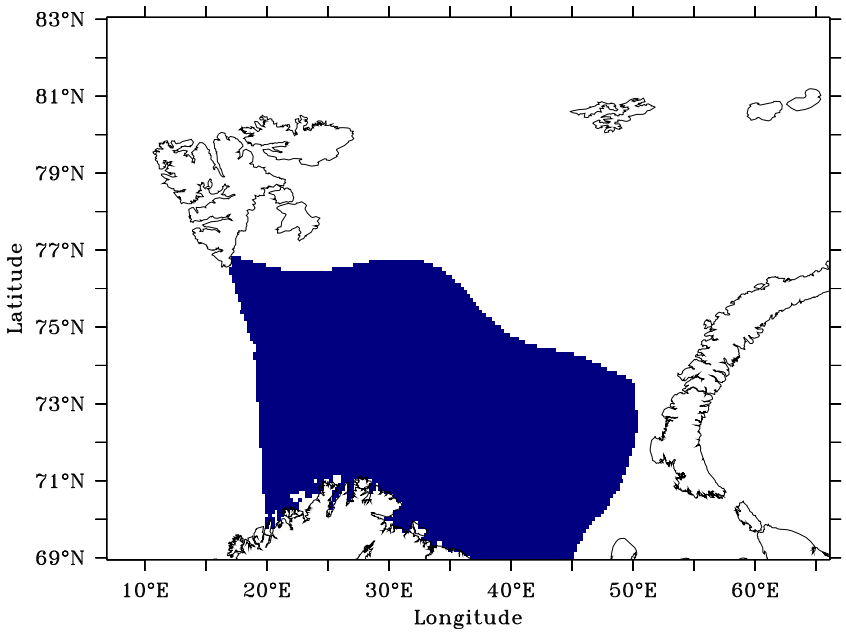

Figure 5.6: Most reliable area as defined from temperature and salinity relative errors.

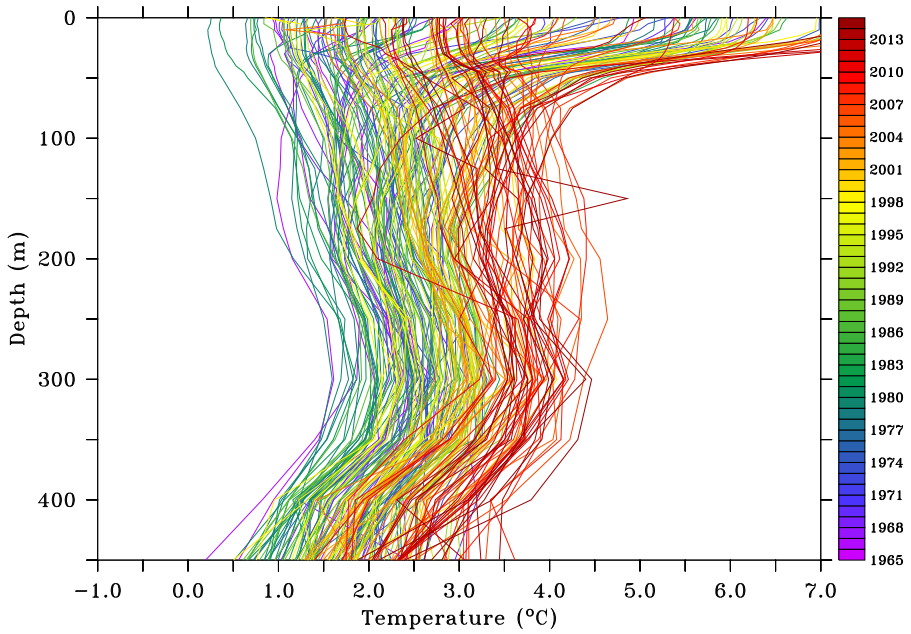

Figure 5.7: Seasonal averaged profiles of temperature on the most reliable area between 1965–2015.

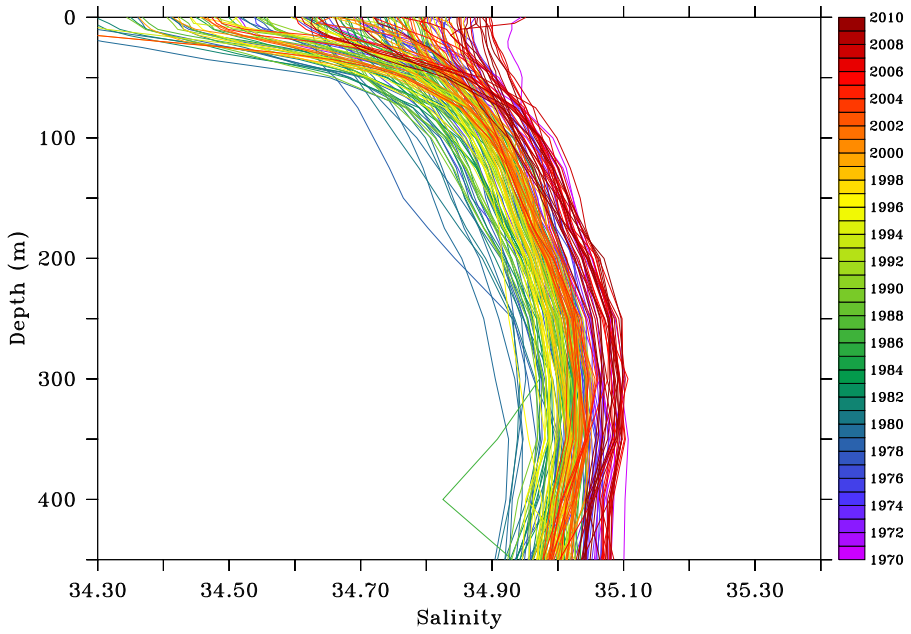

Figure 5.8: Seasonal averaged profiles of salinity on the most reliable area between 1970–2010.

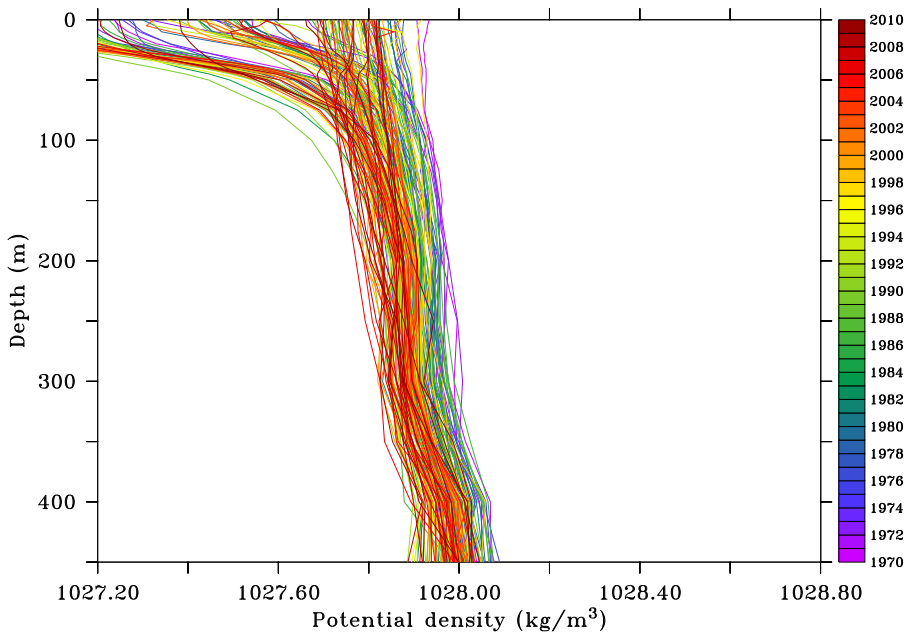

Figure 5.9: Seasonal averaged profiles of potential density on the most reliable area between 1970–2010.

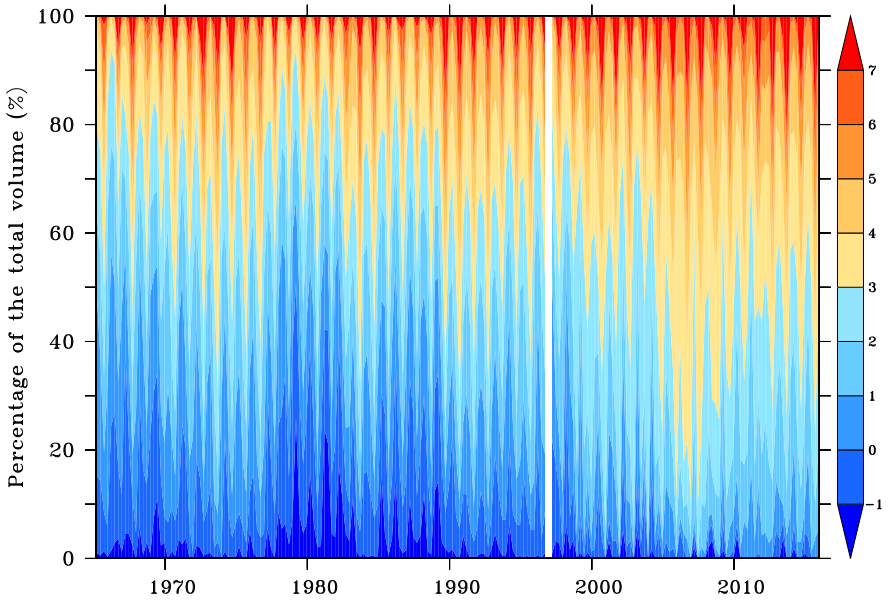

Figure 5.10: Volumetric temperature classes ranging from -1 to +7 °C in the most reliable area per season between 1965–2015.

the relative volume occupied by temperature below 0° C decreased from 19.64% to 1.77%. Changes in salinity classes between 34.4 and 35.2 with a step of 0.1 are shown in Fig. 5.11. Here, matters are less clear but there is however an increase of salinity classes above 35 and a decrease of the lowest-salinity class between 1980–2010. For instance, between the periods 1975–1985 and 2000–2010, the relative volume occupied by salinity below 35 decreased from 86.84% to 62.67%. Moreover, the low salinity associated with the "Great Salinity Anomaly of the 1980s" Dickson et al. (1988) is seen as a distinct maximum of salinities below 34.8. Finally, the potential density relative to the surface is shown in Fig. 5.12 where classes range between 1027.2 and 1028.8 $\mathrm{kg\,m^{-3}}$ with a step of 0.2 $\mathrm{kg\,m^{-3}}$. The potential density does not display large changes on the long term, similarly to the conclusions made above by using profiles. However, water masses with densities above 1028.0 $\mathrm{kg\,m^{-3}}$, associated with dense water production, has rarely exceeded 20 percent of the total water mass within the MRA after year 2000.

5.5.3 Ocean Heat Content

The Ocean Heat Content (OHC) change at the MRA is calculated following the method described in Boyer et al. (2007):

$$OHC = \iiint \rho(T,S,p)c_p(T,S,p)\Delta T\, dxdydz \tag{5.1}$$

where T and S are temperature and salinity averages at each location between 1970–2010, ρ is the density of seawater averaged over 1970–2010 for each grid point, c_p is the specific heat of seawater taken here as 3985 $\mathrm{J\,kg^{-1}\,K^{-1}}$ (Hill, 1962) and ΔT is the temperature anomaly with respect to the averaged temperature on the reference period 1970–2010, that is 2.73° C.

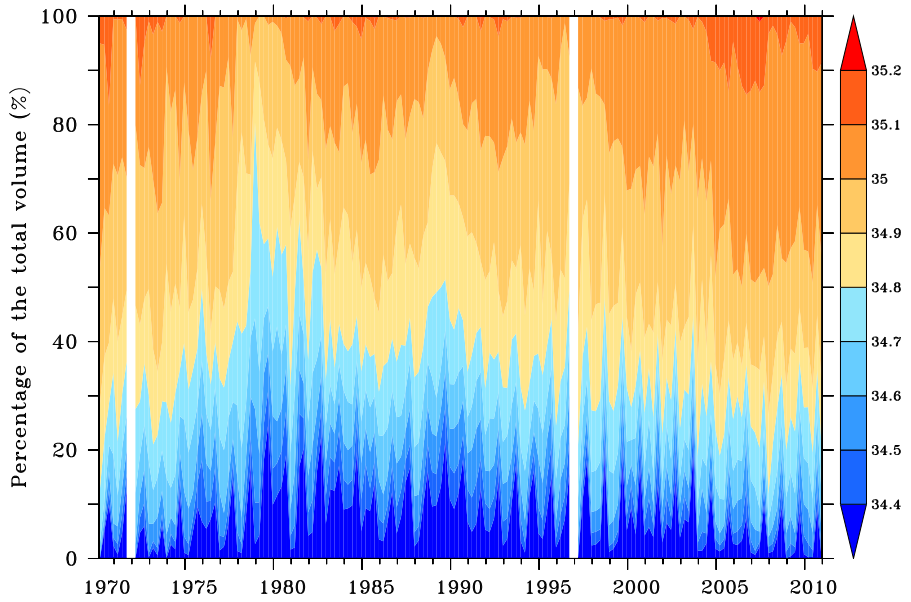

Figure 5.11: Volumetric salinity classes ranging from 34.4 to 35.2 in the most reliable area per season between 1970–2010.

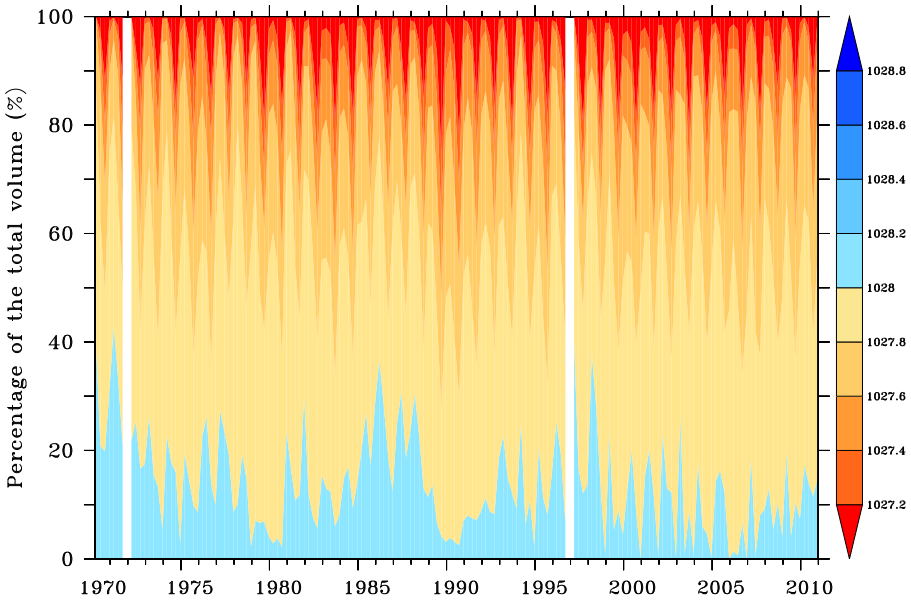

Figure 5.12: Volumetric potential density classes ranging from 1027.2 to 1028.8 $\mathrm{kg\,m^{-3}}$ in the most reliable area per season between 1970–2010.

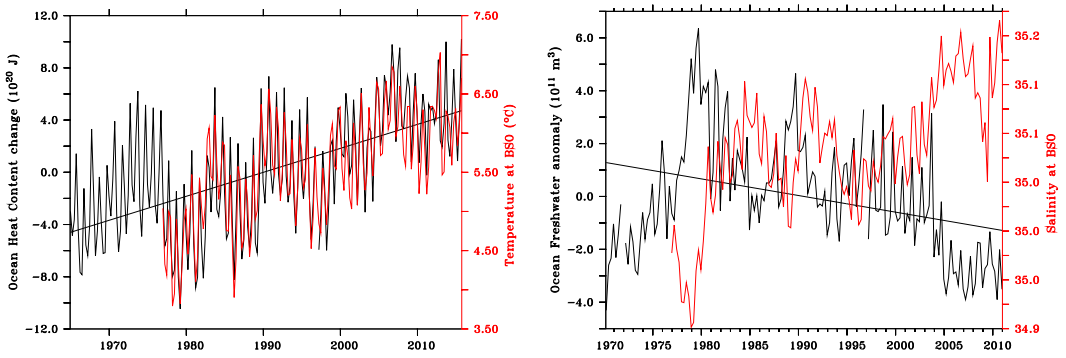

Figure 5.13: (a) Ocean heat content in the Most Reliable Area between 1965–2015, its linear trend (black) and temperature at the Barents Sea Opening. (b) Equivalent freshwater content in the Most Reliable Area between 1970–2010, its linear trend (black) and salinity at the Barents Sea Opening.

Fig. 5.13a shows the OHC changes in the MRA between 1965–2015. The time series shows a positive trend of 5.043×10^{16} J d^{-1} with a R^2 of 0.36, which is significant at a confidence level of 95%. We followed the Fisher–Snedecor test of significance described in Chouquet (2009) and Montgomery et al. (2012) augmented by a penalization of autocorrelation (Wilks, 1995). The temperature from the BSO extracted from ICES (`https://ocean.ices.dk/iroc/#`) is also shown. The correlation between the temperature at the BSO and the OHC is 0.89 (winter 1976– autumn 2015) and also significant at a confidence level of 95%, indicating that the temperature observed at the BSO is a reliable proxy for the OHC downstream in the southern part of the Barents Sea.

5.5.4 Equivalent freshwater content

To investigate changes in salinity in the MRA, we use the Boyer et al. (2007) method to compute the Ocean FreshWater (OFW) anomaly.

$$OFW = -\iiint \frac{\rho(T,S,p)}{\rho(T,0,p)} \frac{\Delta S}{S+\Delta S}\, dxdydz \tag{5.2}$$

where ΔS is the salinity anomaly with respect to averaged salinity on the reference period 1970–2010, that is 34.88, ρ is the density of seawater at each grid point.

In Fig. 5.13b, changes in the OFW in the MRA are shown between 1970–2010. The slope is -1.722×10^7 m^3 d^{-1} with a R^2 of 0.11, which means the negative trend is not significant at a confidence level of 95%, although very close to the significance threshold. We followed the same method as for the OHC to examine the significance. The salinity at the BSO extracted from ICES (`https://ocean.ices.dk/iroc/#`) is also shown. The correlation with the OFW between winter 1976–1977 and winter 2010–2011 is -0.57, also not significant but very close to the significance threshold.

5.6 Conclusions

This research provides a comprehensive atlas of temperature and salinity covering the whole Barents Sea on a regular grid, with an emphasis on its MRA. Although the *in situ* data is sometimes scarce in this part of the Arctic, we show here that physical information can still be extracted from compiled databases by using a variational method minimising the expected errors on the resulting fields. These error fields can be used to exclude unreliable periods of areas, as shown by the examples of usage provided in this study. Besides, the regular grid facilitates the computation and the visualization of various metrics such as profiles, volumetric T-S diagrams or OHC and OFW.

The results of these examples are consistent with the recent "Atlantification" processes at the Barents Sea already observed in the previous studies (e.g. Barton et al., 2018; Lind et al., 2018), that is warmer and more saline Barents Sea, even though our analysis only includes autumn when considering the whole Barents Sea. Concentrating on the MRA in the Barents Sea allowed us to analyze longer period (1965–2015) with all seasons included. The analyses showed similar results to the ones made for the whole Barents Sea, showing an overall positive temperature and salinity trend, that is +1.74° C between 1965–2015 and a salinity increase of 0.11 between 1990–2010. No clear trend was found in density due to the cancelling effects of both temperature and salinity increase. This conclusion is supported by both vertical profiles and volumetric analysis. Finally, the computation of OHC and OFW are consistent with these conclusions as they show positive and negative trend, respectively, during the period 1965–2015 for the OHC and 1970–2010 for the OFW, although the latter trend is not significant. The measurements of temperature and salinity at the BSO are also consistent with the OHC and OFW variabilities. The code as well as the data are made available online (see Sections 5.4 and 5.7) to encourage further research on this topic.

5.7 Code and data availability

The Diva software we used for this research as well as its user guide are available here: `https://github.com/gher-ulg/DIVA`. The data is accessible at `https://doi.org/10.21335/NMDC-2058021735` (Watelet et al., 2020c).

5.8 Supplementary material

5.8.1 Most reliable period

Average relative error for salinity at the Barents Sea surface for the periods 1994–1998 and 2006–2010 is shown in Fig. 5.14.

5.8.2 Most reliable area

Relative error fields are averaged by season in Fig. 5.15 and 5.16 for the most reliable area.

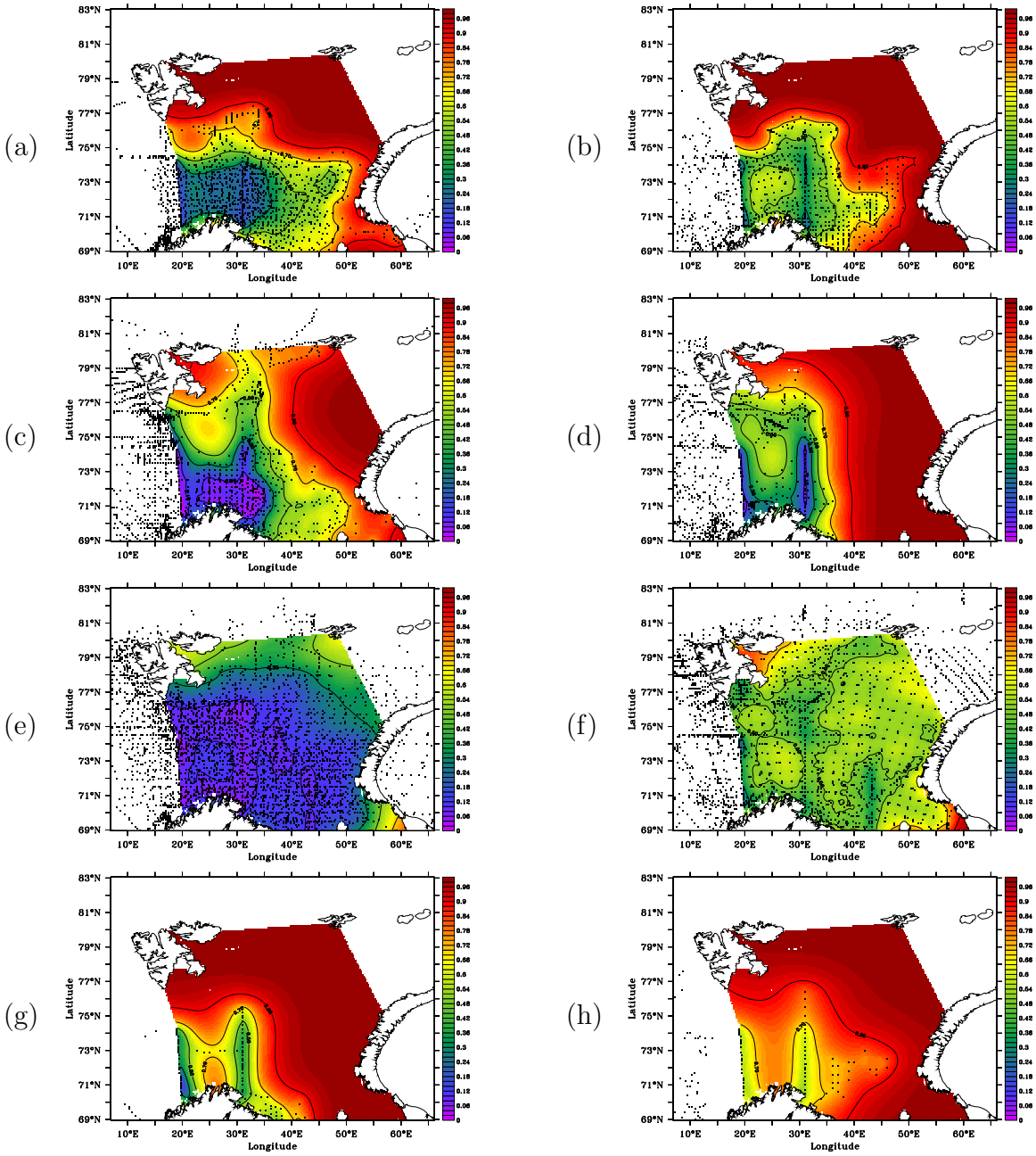

Figure 5.14: Average relative error for salinity at the Barents Sea surface between 1994–1998 (left column) and 2006–2010 (right column) between 1994–1998. (a) and (b) correspond to spring, (c) and (d) to summer, (e) and (f) to autumn, (g) and (h) to winter. This variable measures the added value brought by *in situ* data to the analysis: 0 would be the true field while 1 corresponds to an absence of data, that is an analysis equal to the first guess. The winter 1996–1997 was excluded from the computations due to a lack of data.

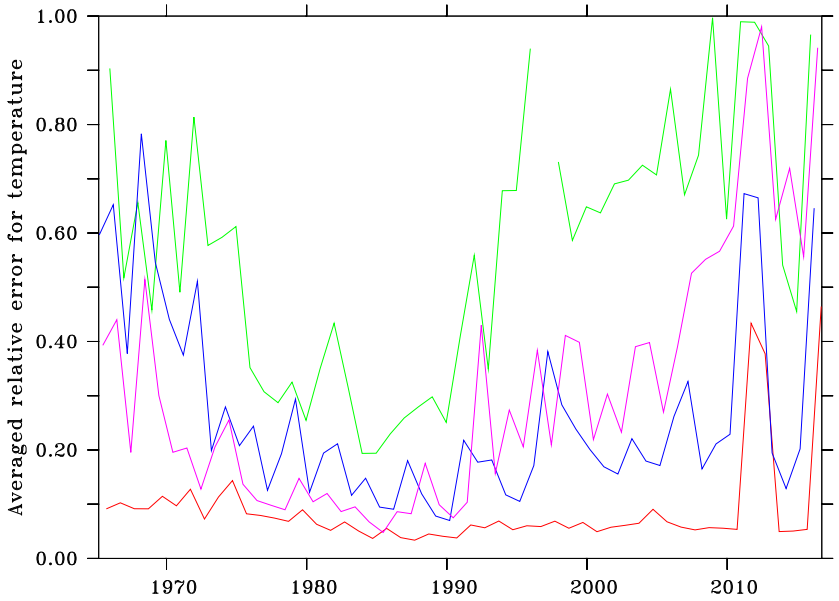

Figure 5.15: Average relative error on the most reliable area for temperature as a function of seasons: autumn (red), winter (green), spring (blue), summer (purple).

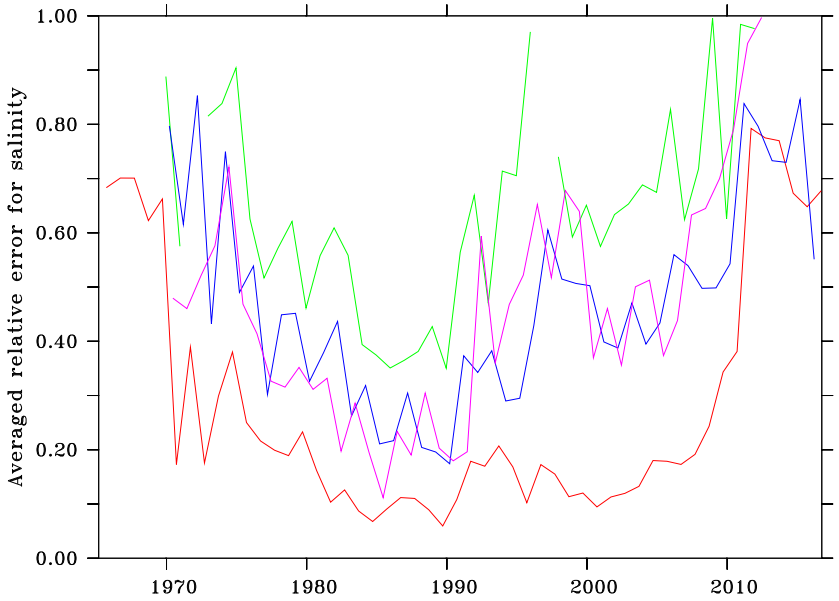

Figure 5.16: Average relative error on the most reliable area for salinity as a function of seasons: autumn (red), winter (green), spring (blue), summer (purple).

Chapter 6

Take-home message

Contents

6.1 Open questions

6.1.1 Global warming and AMOC weakening

In Sections 1.4 and 3.7, we already had a look at the past and future impact of the global warming on the AMOC intensity. Regarding the past, the IPCC concludes to an absence of long-term trend although the consensus is not complete in the scientific community, with several studies suggesting a recent weakening of the AMOC. The literature regards the GS as more stable in intensity, which is confirmed in this thesis through the absence of trend in the GSD index for various recent periods. Considering the future, the IPCC reports a very likely weakening of the AMOC but a near-term increase of the NAO. Following the results of this thesis, a NAO increase could however contribute to a more intense GS. The question is thus: will the AMOC predicted decrease be balanced by the expected positive effect of a NAO boost on the GS intensity?

In this respect, a possible line of research is the use of the IPCC climate models in order to recalculate the GS indices. A comparison of these indices with the ones calculated in this thesis would allow a validation on the recent past. Such a validation is critical before considering future IPCC numerical simulations, as the literature detailed in Section 3.1 describes how the low spatial resolution of the physical models or their short simulation period are often an issue in the current modelling of the GS. If the IPCC models are able to reliably reconstruct the GS position and transport, then the contribution of the NAO in the GS variability could easily be quantified and compared to the results of this thesis. The future trend of this teleconnection could be analyzed as well as its variability, which can only help understanding why the IPCC reports an increase of the NAO but a weakening of the AMOC. Of course, the GS is not the only component of the AMOC and the NAO is not the only driver of the GS, so these results are not necessarily inconsistent. Besides, the impact of the future melt of the Greenland Ice Sheet (GrIS) on the weakening of the AMOC is largely neglected in the IPCC reports, which is why Bakker et al. (2016) used 8 state-of-the-science GCMs (AMOCMIP) to estimate the impact of this melt on the AMOC until 2300. Up to 2100, they show the contribution of the GrIS meltwater to the AMOC weakening to be minor with respect to other factors, although this contribution raises to 37% by 2300 for the RCP8.5 global warming scenario corresponding to high greenhouse-gas emissions. Here also, only the AMOC defined as the maximum overturning streamfunction below 500 m at 26°N is considered, which reveals a need for more studies focussing on its GS component.

6.1.2 DIVAnd and improvement of data analyses

The data analyses that were performed in this thesis used the pseudo-3D version of DIVA to generate series of 2D analyses for each depth layer and each time step. Recently, a new version of DIVA named DIVAnd has been developed by the GHER (ULiège) and is able to take depth and time dimensions into account. Can these added dimensions bring significantly better analyses that would mitigate the scarcity of data for the pre-1940 era?

6.1.3 Rossby waves and mesoscale eddies

Using satellite observations, Chelton et al. (2011) showed that a part of the westward-propagating SSH variability is due to nonlinear mesoscale eddies. However, the eddies they found have an average lifetime of 32 weeks and an average propagation distance of 550 km, which are much smaller scales than the Rossby waves we describe. In addition, the wavelength of these Rossby waves (1066 km) is much larger than the Rossby radius of deformation (30 km) at 39° N, indicating the observed westward propagation to be mostly due to waves rather than eddies. In order to further quantify the part of the westward signal from the 2D-RT that is due to Rossby waves against possible eddies, we propose the following future experiments. 1) Performing a tracking of eddies for different latitudes based on the DRAKKAR SSH fields. 2) From DRAKKAR temperature and salinity fields, calculate the densities, the baroclinic eigen modes, the steric height, and the eddie propagation relative to each baroclinic mode. This would also help future studies to analyse how the NAO signal is carried to the westward propagating SSH, and how this SSH variability impacts in turn the GS.

6.1.4 Deep water formation in the Barents Sea

In Section 5.1, we showed that the literature suggests the Barents Sea to be one of the places in the Global ocean where the deep-water formation occurs and thus feed the AMOC. Will the observed "Atlantification" of the Barents Sea contribute to a future change in this crucial process?

This Barents Sea atlas could be seen as a reference in order to carry an intercomparison of numerical models on such a region with limited data available. Also, deep water formation is also present in the other seas of the Arctic Ocean, and the Norwegian Sea would be a good candidate for another temperature and salinity atlas due to the amount of data available in this area.

6.1.5 Other climate indices

Other climate indices are or might be correlated to the GS. Among them, Hameed et al. (2018) showed the Atlantic Meridional Mode (AMM) also impacts the interannual variability of the GSNW. Taylor et al. (1998) showed that the GS shifts northward after an El Niño Southern Oscillation (ENSO) event, although the NAO remains the primary cause of GS latitude changes. To our best knowledge, the Arctic Oscillation (AO) and the Quasi-Biennal Oscillation (QBO) have not been correlated with the GS so far.

6.2 Summary of the findings

In Chapter 3, we reconstructed monthly fields of ocean temperature and salinity in the GS region since 1940. From these fields, we derived a GS index relative to its position (the GSNW) and 2 GS indices relative to its intensity (the GSD and GST). We were able to show that these indices are significantly correlated with the NAO

provided a time lag is taken into account. This lag between the NAO and the GS is approximately 1 year for the GSNW and 0 or 2 years for the GSD and GST indices.

Since a correlation does not necessarily imply a cause-and-effect relationship, we explored in depth one possible physical explanation for these time lags. The Chapter 4 shows that the DRAKKAR simulations are able to model baroclinic Rossby waves at the GS latitude. Using a very long time series of 46 years, the speed of these waves is estimated at $4.17\,\mathrm{cm\,s^{-1}}$ which is consistent with the longest time lag observed between the NAO and the GS intensity.

Finally, a comprehensive atlas of temperature and salinity in the Barents Sea is presented in Chapter 5. This atlas covers all the water column for each season between 1965–2016. The evolution of the T-S characteristics over time are investigated through volumetric analyses and time series of ocean heat and freshwater contents are calculated. The results show a clear "Atlantification" of the Barents Sea, where the temperature and salinity increase whilst the density remains virtually unchanged. While a relatively stable density throughout the whole water column would not suggest large changes in the deep water formation processes, the magnitude of the recent temperature and salinity increases advocates for a greater focus on the Barents Sea in the measuring campaigns, especially in the areas where we identified larger analysis errors due to the scarcity of data.

Bibliography

Bakker, P., Schmittner, A., Lenaerts, J., Abe-Ouchi, A., Bi, D., van den Broeke, M., Chan, W.-L., Hu, A., Beadling, R., Marsland, S. et al. (2016). Fate of the Atlantic Meridional Overturning Circulation: Strong decline under continued warming and Greenland melting. *Geophysical Research Letters*, *43*, 12–252.

Banzon, V. F., & Reynolds, R. W. (2013). Use of WindSat to Extend a Microwave-Based Daily Optimum Interpolation Sea Surface Temperature Time Series. *Journal of Climate*, *26*, 2557–2562.

Barnier, B., Brodeau, L., Le Sommer, J., Molines, J.-M., Penduff, T., Theetten, S., Treguier, A.-M., Madec, G., Biastoch, A., Böning, C. W. et al. (2007). Eddy-permitting ocean circulation hindcasts of past decades. *Clivar Exchanges*, *42*, 8–10.

Barnier, B., Madec, G., Penduff, T., Molines, J.-M., Treguier, A.-M., Le Sommer, J., Beckmann, A., Biastoch, A., Böning, C., Dengg, J. et al. (2006). Impact of partial steps and momentum advection schemes in a global ocean circulation model at eddy-permitting resolution. *Ocean Dynamics*, *56*, 543–567. doi:10.1007/s10236-006-0082-1.

Barnston, A. G., & Livezey, R. E. (1987). Classification, seasonality and persistence of low-frequency atmospheric circulation patterns. *Monthly weather review*, *115*, 1083–1126.

Barton, B. I., Lenn, Y.-D., & Lique, C. (2018). Observed Atlantification of the Barents Sea causes the polar front to limit the expansion of winter sea ice. *Journal of Physical Oceanography*, *48*, 1849–1866.

Beckers, J.-M., Barth, A., Troupin, C., & Alvera-Azcárate, A. (2014). Approximate and efficient methods to assess error fields in spatial gridding with data interpolating variational analysis (DIVA). *Journal of Atmospheric and Oceanic Technology*, *31*, 515–530.

Blanke, B., & Delecluse, P. (1993). Variability of the tropical Atlantic Ocean simulated by a general circulation model with two different mixed-layer physics. *Journal of Physical Oceanography*, *23*, 1363–1388.

Booth, J. F., Thompson, L., Patoux, J., & Kelly, K. A. (2012). Sensitivity of midlatitude storm intensification to perturbations in the sea surface temperature near the Gulf Stream. *Monthly Weather Review*, *140*, 1241–1256.

Borkman, D. G., & Smayda, T. J. (2009). Gulf Stream position and winter NAO as drivers of long-term variations in the bloom phenology of the diatom Skeletonema costatum "species-complex" in Narragansett Bay, RI, USA. *Journal of plankton research*, *31*, 1407–1425.

Boyer, T., Antonov, J., Baranova, O., Coleman, C., Garcia, H., Grodsky, A., Johnson, D., Locarnini, R., Mishonov, A., O'Brien, T., Paver, C., Reagan, J., Seidov, D., Smolyar, I., & Zweng, M. (2013). *World Ocean Database 2013* volume 72. Sydney Levitus, Ed.; Alexey Mishonov, Technical Ed.; NOAA Atlas NESDIS.

Boyer, T., Levitus, S., Antonov, J., Locarnini, R., Mishonov, A., Garcia, H., & Josey, S. A. (2007). Changes in freshwater content in the North Atlantic Ocean 1955–2006. *Geophysical Research Letters*, *34*.

Brasseur, P. (1995). *Reconstitution de champs d'observations océanographiques par le Modèle Variationnel Inverse: Méthodologie et Applications*. Ph.D. thesis Universite de Liege, Faculte des sciences appliquees.

Buckley, M. W., & Marshall, J. (2016). Observations, inferences, and mechanisms of the Atlantic Meridional Overturning Circulation: A review. *Reviews of Geophysics*, *54*, 5–63.

Caesar, L., Rahmstorf, S., Robinson, A., Feulner, G., & Saba, V. (2018). Observed fingerprint of a weakening Atlantic Ocean overturning circulation. *Nature*, *556*, 191–196.

Challenor, P. G., Cipollini, P., & Cromwell, D. (2001). Use of the 3D Radon transform to examine the properties of oceanic Rossby waves. *Journal of Atmospheric and Oceanic Technology*, *18*, 1558–1566. doi:10.1175/1520-0426(2001)018<1558:UOTRTT>2.0.CO;2.

Chaudhuri, A. H., Gangopadhyay, A., & Bisagni, J. J. (2009). Interannual variability of Gulf Stream warm-core rings in response to the North Atlantic Oscillation. *Continental Shelf Research*, *29*, 856–869.

Chaudhuri, A. H., Gangopadhyay, A., & Bisagni, J. J. (2011). Response of the Gulf Stream transport to characteristic high and low phases of the North Atlantic Oscillation. *Ocean Modelling*, *39*, 220–232.

Chelton, D. B., Deszoeke, R. A., Schlax, M. G., El Naggar, K., & Siwertz, N. (1998). Geographical variability of the first baroclinic Rossby radius of deformation. *Journal of Physical Oceanography*, *28*, 433–460. doi:10.1175/1520-0485(1998)028<0433:GVOTFB>2.0.CO;2.

Chelton, D. B., & Schlax, M. G. (1996). Global observations of oceanic Rossby waves. *Science*, *272*, 234–238. doi:10.1126/science.272.5259.234.

Chelton, D. B., Schlax, M. G., & Samelson, R. M. (2011). Global observations of nonlinear mesoscale eddies. *Progress in oceanography*, *91*, 167–216.

Chen, W. Y., & Van den Dool, H. (2003). Sensitivity of teleconnection patterns to the sign of their primary action center. *Monthly weather review*, *131*, 2885–2899.

Chouquet, C. (2009). Modèles Linéaires, Laboratoire de Statistique et Probabilités. `www.math.univ-toulouse.fr/~barthe/M1modlin/poly.pdf`. [Online; accessed 22-September-2015].

Church, J. A. (2007). A change in circulation? *Science*, *317*, 908–909.

Cipollini, P., Cromwell, D., Jones, M. S., Quartly, G. D., & Challenor, P. G. (1997). Concurrent altimeter and infrared observations of Rossby wave propagation near 34°N in the Northeast Atlantic. *Geophysical Research Letters*, *24*, 889–892. doi:10.1029/97GL00758.

Cipollini, P., Cromwell, D., & Quartly, G. (1998). Observations of Rossby wave propagation in the northeast Atlantic with TOPEX/POSEIDON altimetry. *Advances in Space Research*, *22*, 1553–1556.

Cipollini, P., Quartly, G. D., Challenor, P. G., Cromwell, D., & Robinson, I. S. (2006). Remote sensing of extra-equatorial planetary waves. In *Manual of Remote Sensing*. American Society for Photogrammetry and Remote Sensing.

Comiso, J. C., & Hall, D. K. (2014). Climate trends in the Arctic as observed from space. *Wiley Interdisciplinary Reviews: Climate Change*, *5*, 389–409.

Cook, E. R., D'Arrigo, R. D., & Briffa, K. R. (1998). A reconstruction of the North Atlantic Oscillation using tree-ring chronologies from North America and Europe. *The Holocene*, *8*, 9–17. doi:10.1191/095968398677793725.

Cook, J., Nuccitelli, D., Green, S. A., Richardson, M., Winkler, B., Painting, R., Way, R., Jacobs, P., & Skuce, A. (2013). Quantifying the consensus on anthropogenic global warming in the scientific literature. *Environmental research letters*, *8*, 024024.

Craven, P., & Wahba, G. (1978). Smoothing noisy data with spline functions. *Numerische mathematik*, *31*, 377–403.

Curry, R. G., & McCartney, M. S. (2001). Ocean Gyre Circulation Changes Associated with the North Atlantic Oscillation. *Journal of Physical Oceanography*, *31*, 3374–3400.

Cushman-Roisin, B., & Beckers, J.-M. (2011). *Introduction to geophysical fluid dynamics: physical and numerical aspects* volume 101. Academic Press.

De Coëtlogon, G., Frankignoul, C., Bentsen, M., Delon, C., Haak, H., Masina, S., & Pardaens, A. (2006). Gulf Stream variability in five oceanic general circulation models. *Journal of Physical Oceanography*, *36*, 2119–2135. doi:10.1175/JPO2963.1.

Deans, S. R. (1983). *The Radon transform and some of its applications*. John Wiley and Sons, Inc., New York.

Dickson, R. R., Meincke, J., Malmberg, S.-A., & Lee, A. J. (1988). The "great salinity anomaly" in the northern North Atlantic 1968–1982. *Progress in Oceanography*, *20*, 103–151.

Van den Dool, H., Saha, S., & Johansson, Å. (2000). Empirical orthogonal teleconnections. *Journal of Climate*, *13*, 1421–1435.

Drinkwater, K., Myers, R., Pettipas, R., & Wright, T. (1994). *Climatic data for the northwest Atlantic : the position of the shelf/slope front and the northern boundary of the Gulf Strea between 50°W and 75°W*. Canadian Data Report of Fisheries and Ocean Sciences. Candian Department of Fisheries and Oceans, Scotia-Fundy Region.

Dussin, R., Barnier, B., Brodeau, L., & Molines, J.-M. (2018). *The making of the Drakkar Forcing set DFS5*. Technical Report University of Grenoble. doi:10.5281/zenodo.1209243.

Ebisuzaki, W. (1997). A method to estimate the statistical significance of a correlation when the data are serially correlated. *Journal of Climate*, *10*, 2147–2153. doi:10.1175/1520-0442(1997)010<2147:AMTETS>2.0.CO;2.

Eriksen, E., Gjøsæter, H., Prozorkevich, D., Shamray, E., Dolgov, A., Skern-Mauritzen, M., Stiansen, J. E., Kovalev, Y., & Sunnanå, K. (2018). From single species surveys towards monitoring of the Barents Sea ecosystem. *Progress in Oceanography*, *166*, 4–14.

Esselborn, S., & Eden, C. (2001). Sea surface height changes in the North Atlantic Ocean related to the North Atlantic Oscillation. *Geophysical Research Letters*, *28*, 3473–3476. doi:10.1029/2001GL012863.

Ezer, T., & Atkinson, L. P. (2014). Accelerated flooding along the US East Coast: On the impact of sea-level rise, tides, storms, the Gulf Stream, and the North Atlantic Oscillations. *Earth's Future*, *2*, 362–382.

Fossheim, M., Primicerio, R., Johannesen, E., Ingvaldsen, R. B., Aschan, M. M., & Dolgov, A. V. (2015). Recent warming leads to a rapid borealization of fish communities in the Arctic. *Nature Climate Change*, *5*, 673–677.

Frankignoul, C., de Coëtlogon, G., Joyce, T. M., & Dong, S. (2001). Gulf Stream Variability and Ocean-Atmosphere Interactions. *Journal of physical Oceanography*, *31*, 3516–3529.

Fuglister, F. C. (1955). Alternative analyses of current surveys. *Deep Sea Research (1953)*, *2*, 213–229.

Fuglister, F. C. (1963). Gulf stream '60. *Progress in oceanography*, *1*, 265–373.

Gangopadhyay, A., Chaudhuri, A. H., & Taylor, A. H. (2016). On the Nature of Temporal Variability of the Gulf Stream Path from 75° to 55° W. *Earth Interactions*, *20*, 1–17.

Gangopadhyay, A., Cornillon, P., & Watts, D. R. (1992). A test of the Parsons-Veronis hypothesis on the separation of the Gulf Stream. *Journal of Physical Oceanography*, *22*, 1286–1301.

Halkin, D., & Rossby, T. (1985). The structure and transport of the Gulf Stream at 73° W. *Journal of Physical Oceanography*, *15*, 1439–1452.

Hameed, S., & Piontkovski, S. (2004). The dominant influence of the Icelandic Low on the position of the Gulf Stream northwall. *Geophysical Research Letters*, *31*. doi:10.1029/2004GL019561.

Hameed, S., Wolfe, C. L., & Chi, L. (2018). Impact of the Atlantic meridional mode on Gulf Stream North Wall position. *Journal of Climate*, *31*, 8875–8894.

Hartman, L., & Hössjer, O. (2008). Fast kriging of large data sets with Gaussian Markov random fields. *Computational Statistics & Data Analysis*, *52*, 2331–2349.

Helland-Hansen, B., & Nansen, F. (1909). *The Norwegian Sea: its physical oceanography based upon the Norwegian researches 1900-1904*. Det Mallingske Bogtrykkeri.

Hill, M. N. E. (1962). *The Sea: Composition of Sea-Water* volume 2. Wiley.

Hogg, N. G. (1992). On the transport of the Gulf Stream between Cape Hatteras and the Grand Banks. *Deep Sea Research Part A. Oceanographic Research Papers*, *39*, 1231–1246.

Hurrell, J., Kushnir, Y., Ottersen, G., & Visbeck, M. (2003). *The North Atlantic Oscillation: climate significance and environmental impact* volume 134 of *Eds. Geophysical Monograph Series*. Washington DC: American Geophysical Union.

Hurrell, J. W. (1995). Decadal trends in the North Atlantic Oscillation: regional temperatures and precipitation. *Science*, *269*, 676–679. doi:10.1126/science.269.5224.676.

Hurrell, J. W., & Deser, C. (2010). North Atlantic climate variability: the role of the North Atlantic Oscillation. *Journal of Marine Systems*, *79*, 231–244. doi:10.1016/j.jmarsys.2009.11.002.

Johannesen, E., Ingvaldsen, R. B., Bogstad, B., Dalpadado, P., Eriksen, E., Gjøsæter, H., Knutsen, T., Skern-Mauritzen, M., & Stiansen, J. E. (2012). Changes in Barents Sea ecosystem state, 1970–2009: climate fluctuations, human impact, and trophic interactions. *ICES Journal of Marine Science*, *69*, 880–889.

Johns, W. E., Shay, T., Bane, J., & Watts, D. (1995). Gulf Stream structure, transport, and recirculation near 68 W. *Journal of Geophysical Research: Oceans*, *100*, 817–838.

Joyce, T. M., Deser, C., & Spall, M. A. (2000). The relation between decadal variability of subtropical mode water and the North Atlantic Oscillation*. *Journal of Climate*, *13*, 2550–2569. doi:10.1175/1520-0442(2000)013<2550:TRBDVO>2.0.CO;2.

Kelly, K. A., & Gille, S. T. (1990). Gulf Stream Surface Transport and Statistics at 69°W. *Journal of Geophysical Research*, *95*, 3149–3161.

Kelly, K. A., Small, R. J., Samelson, R., Qiu, B., Joyce, T. M., Kwon, Y.-O., & Cronin, M. F. (2010). Western boundary currents and frontal air–sea interaction: Gulf Stream and Kuroshio Extension. *Journal of Climate*, *23*, 5644–5667.

Killworth, P. D., & Blundell, J. R. (2003). Long extratropical planetary wave propagation in the presence of slowly varying mean flow and bottom topography. Part I: The local problem. *Journal of Physical Oceanography*, *33*, 784–801. doi:10.1175/1520-0485(2003)33<784:LEPWPI>2.0.CO;2.

Killworth, P. D., & Blundell, J. R. (2004). The dispersion relation for planetary waves in the presence of mean flow and topography. Part I: Analytical theory and one-dimensional examples. *Journal of physical oceanography*, *34*, 2692–2711. doi:10.1175/JPO2635.1.

Killworth, P. D., & Blundell, J. R. (2005). The dispersion relation for planetary waves in the presence of mean flow and topography. Part II: Two-dimensional examples and global results. *Journal of physical oceanography*, *35*, 2110–2133. doi:10.1175/JPO2817.1.

Killworth, P. D., Chelton, D. B., & de Szoeke, R. A. (1997). The speed of observed and theoretical long extratropical planetary waves. *Journal of Physical Oceanography*, *27*, 1946–1966. doi:10.1175/1520-0485(1997)027<1946:TSOOAT>2.0.CO;2.

Knipowitsch, N. (1905). Hydrologische Untersuchungen im Europäischen Eismeer. *Annalen der Hydrographie und Maritimen Meteorologie*, *33*, 241–260.

Kuhlbrodt, T., Rahmstorf, S., Zickfeld, K., Vikebø, F. B., Sundby, S., Hofmann, M., Link, P. M., Bondeau, A., Cramer, W., & Jaeger, C. (2009). An integrated assessment of changes in the thermohaline circulation. *Climatic Change*, *96*, 489–537.

Kwon, Y.-O., Alexander, M. A., Bond, N. A., Frankignoul, C., Nakamura, H., Qiu, B., & Thompson, L. A. (2010). Role of the Gulf Stream and Kuroshio-Oyashio systems in large-scale atmosphere-ocean interaction: A review. *Journal of Climate*, *23*, 3249–3281.

Lecointre, A., Penduff, T., Cipollini, P., Tailleux, R., & Barnier, B. (2008). Depth dependence of westward-propagating North Atlantic features diagnosed from altimetry and a numerical 1/6° model. *Ocean Science*, *4*, 99–113.

Lee, D.-T., & Schachter, B. J. (1980). Two algorithms for constructing a Delaunay triangulation. *International Journal of Computer & Information Sciences*, *9*, 219–242.

Levitus, S., & Boyer, T. P. (1994). *World Ocean Atlas 1994. Volume 4. Temperature*. Technical Report National Environmental Satellite, Data, and Information Service, Washington, DC (United States).

Li, X., Zheng, W., Pichel, W. G., Zou, C.-Z., Clemente-Colón, P., & Friedman, K. S. (2004). A cloud line over the Gulf Stream. *Geophysical research letters*, *31*.

Lind, S., Ingvaldsen, R. B., & Furevik, T. (2018). Arctic warming hotspot in the northern Barents Sea linked to declining sea-ice import. *Nature climate change*, *8*, 634.

Locarnini, R., Mishonov, A., Baranova, O., Boyer, T., Zweng, M., Garcia, H., Reagan, J., Seidov, D., Weathers, K., Paver, C., & Smolyar, I. (2018). World ocean atlas 2018. *Temperature*, (p. 52).

Lozier, M., Li, F., Bacon, S., Bahr, F., Bower, A., Cunningham, S., De Jong, M., De Steur, L., Deyoung, B., Fischer, J. et al. (2019). A sea change in our view of overturning in the subpolar North Atlantic. *Science*, *363*, 516–521.

Lund, D. C., Lynch-Stieglitz, J., & Curry, W. B. (2006). Gulf Stream density structure and transport during the past millennium. *Nature*, *444*, 601–604.

Madec, G., Delecluse, P., Imbard, M., & Levy, C. (1998). OPA8. 1 ocean general circulation model reference manual. Notes du Pôle de Modélisation IPSL. *Pierre Simon Laplace, Paris*, .

Madec, G., & NEMO-team (2016). *Note du Pôle de modélisation de l'Institut Pierre-Simon Laplace No 27*. Technical Report.

Maharaj, A. M., Cipollini, P., & Holbrook, N. (2004). Do multiple peaks in the Radon Transform of westward propagating sea surface height anomalies correspond to higher order Rossby wave Baroclinic modes? In *13th AMS Conference on Satellite Meteorology and Oceanography, Norfolk VA, USA 20-23 Sep 2004, extended abstracts* (pp. 685–689). American Meteorological Society.

Maharaj, A. M., Cipollini, P., Holbrook, N. J., Killworth, P. D., & Blundell, J. R. (2007). An evaluation of the classical and extended Rossby wave theories in explaining spectral estimates of the first few baroclinic modes in the South Pacific Ocean. *Ocean Dynamics*, *57*, 173–187. doi:10.1007/s10236-006-0099-5.

Manning, S., & Cogliano, F. D. (2008). *The Atlantic Enlightenment*. Ashgate Publishing, Ltd.

Mauritzen, C., Rudels, B., & Toole, J. (2013). The Arctic and Subarctic Oceans/Seas. In *International Geophysics* (pp. 443–470). Elsevier volume 103.

Molines, J.-M. (2020). SSH data set used for Rossby Wave Analysis, extraction from ORCA12.L46-MJM189 DRAKKAR simulation. URL: `https://doi.org/10.5281/zenodo.3968801`. doi:10.5281/zenodo.3968801.

Montgomery, D. C., Peck, E. A., & Vining, G. G. (2012). *Introduction to linear regression analysis* volume 821. John Wiley & Sons.

Mork, K. A., Skagseth, Ø., & Søiland, H. (2019). Recent warming and freshening of the Norwegian Sea observed by Argo data. *Journal of Climate*, *32*, 3695–3705.

National Center for Atmospheric Research Staff (2015). The Climate Data Guide: Hurrell North Atlantic Oscillation (NAO) Index (PC-based). `https://climatedataguide.ucar.edu/climate-data/hurrell-north-atlantic-oscillation-nao-index-pc-based`. [Online; accessed 23-September-2015].

National Oceanic and Atmospheric Administration (1977). Gulfstream.

Nye, J. A., Joyce, T. M., Kwon, Y.-O., & Link, J. S. (2011). Silver hake tracks changes in Northwest Atlantic circulation. *Nature communications*, *2*, 1–6.

Osychny, V., & Cornillon, P. (2004). Properties of Rossby waves in the North Atlantic estimated from satellite data. *Journal of Physical Oceanography*, *34*, 61–76. doi:10.1175/1520-0485(2004)034<0061:PORWIT>2.0.CO;2.

Parker, A., & Ollier, C. (2016). There is no real evidence for a diminishing trend of the Atlantic meridional overturning circulation. *Journal of Ocean Engineering and Science*, *1*, 30–35.

Peña-Molino, B., & Joyce, T. M. (2008). Variability in the slope water and its relation to the Gulf Stream path. *Geophysical Research Letters*, *35*.

Penduff, T., Barnier, B., Dewar, W. K., & O'Brien, J. J. (2004). Dynamical response of the oceanic eddy field to the North Atlantic Oscillation: A model-data comparison. *Journal of Physical Oceanography*, *34*, 2615–2629. doi:10.1175/JPO2618.1.

Penduff, T., Juza, M., Brodeau, L., Smith, G., Barnier, B., Molines, J.-M., Tréguier, A.-M., & Madec, G. (2010). Impact of global ocean model resolution on sea-level variability with emphasis on interannual time scales. *Ocean Science*, *6*, 269–284.

Pérez-Hernández, M. D., & Joyce, T. M. (2014). Two modes of Gulf Stream variability revealed in the last two decades of satellite altimeter data. *Journal of Physical Oceanography*, *44*, 149–163.

Poli, P., Hersbach, H., Dee, D. P., Berrisford, P., Simmons, A. J., Vitart, F., Laloyaux, P., Tan, D. G., Peubey, C., Thépaut, J.-N. et al. (2016). ERA-20C: An atmospheric reanalysis of the twentieth century. *Journal of Climate*, *29*, 4083–4097.

Reiniger, R., & Ross, C. (1968). A method of interpolation with application to oceanographic data. In *Deep Sea Research and Oceanographic Abstracts* (pp. 185–193). Elsevier volume 15.

Reynolds, R. W., Smith, T. M., Liu, C., Chelton, D. B., Casey, K. S., & Schlax, M. G. (2007). Daily high-resolution-blended analyses for sea surface temperature. *Journal of Climate*, *20*, 5473–5496.

Rixen, M., Beckers, J.-M., Brankart, J.-M., & Brasseur, P. (2000). A numerically efficient data analysis method with error map generation. *Ocean Modelling*, *2*, 45–60.

Rossby, T. (1996). The North Atlantic Current and surrounding waters: At the crossroads. *Reviews of Geophysics*, *34*, 463–481.

Rossby, T. (1999). On gyre interactions. *Deep Sea Research Part II: Topical Studies in Oceanography*, *46*, 139–164. doi:10.1016/S0967-0645(98)00095-2.

Rossby, T., Flagg, C., Donohue, K., Sanchez-Franks, A., & Lillibridge, J. (2014). On the long-term stability of Gulf Stream transport based on 20 years of direct measurements. *Geophysical Research Letters*, *41*, 114–120. doi:10.1002/2013GL058636.

Sasaki, Y. N., & Schneider, N. (2011). Interannual to decadal Gulf Stream variability in an eddy-resolving ocean model. *Ocean Modelling*, *39*, 209–219. doi:10.1016/j.ocemod.2011.04.004.

Sato, O. T., & Rossby, T. (1995). Seasonal and low frequency variations in dynamic height anomaly and transport of the Gulf Stream. *Deep Sea Research Part I: Oceanographic Research Papers*, *42*, 149–164.

Schauer, U., Muench, R. D., Rudels, B., & Timokhov, L. (1997). Impact of eastern Arctic shelf waters on the Nansen Basin intermediate layers. *Journal of Geophysical Research: Oceans*, *102*, 3371–3382.

Schmutz, C., Luterbacher, J., Gyalistras, D., Xoplaki, E., & Wanner, H. (2000). Can we trust proxy-based NAO index reconstructions? *Geophysical Research Letters*, *27*, 1135–1138. doi:10.1029/1999GL011045.

Seager, R., Battisti, D. S., Yin, J., Gordon, N., Naik, N., Clement, A. C., & Cane, M. A. (2002). Is the Gulf Stream responsible for Europe's mild winters? *Quarterly Journal of the Royal Meteorological Society: A journal of the atmospheric sciences, applied meteorology and physical oceanography*, *128*, 2563–2586.

Sérazin, G., Penduff, T., Grégorio, S., Barnier, B., Molines, J.-M., & Terray, L. (2015). Intrinsic variability of sea level from global ocean simulations: Spatiotemporal scales. *Journal of Climate*, *28*, 4279–4292.

Skagseth, Ø., Eldevik, T., Årthun, M., Asbjørnsen, H., Lien, V. S., & Smedsrud, L. H. (2020). Reduced efficiency of the Barents Sea cooling machine. *Nature Climate Change*, (pp. 1–6).

Smedsrud, L. H., Esau, I., Ingvaldsen, R. B., Eldevik, T., Haugan, P. M., Li, C., Lien, V. S., Olsen, A., Omar, A. M., Otterå, O. H. et al. (2013). The role of the Barents Sea in the Arctic climate system. *Reviews of Geophysics*, *51*, 415–449.

Smeed, D., McCarthy, G., Cunningham, S., Frajka-Williams, E., Rayner, D., Johns, W., Meinen, C., Baringer, M., Moat, B., Duchez, A. et al. (2014). Observed decline of the Atlantic meridional overturning circulation 2004–2012. *Ocean Science*, *10*, 29–38.

Solomon, S., Qin, D., Manning, M., Chen, Z., Marquis, M., Averyt, K., Tignor, M., & Miller, H. (2007). IPCC, Climate change 2007: the physical science basis. Contribution of working group I to the fourth assessment report of the intergovernmental panel on climate change.

Stocker, T., Qin, D., Plattner, G., Tignor, M., Allen, S., Boschung, J., Nauels, A., Xia, Y., Bex, V., & Midgley, P. (2013). Climate change 2013: The physical science basis. Intergovernmental panel on climate change, working group I contribution to the IPCC fifth assessment report (AR5).

Swift, J. H., Takahashi, T., & Livingston, H. D. (1983). The contribution of the Greenland and Barents seas to the deep water of the Arctic Ocean. *Journal of Geophysical Research: Oceans*, *88*, 5981–5986.

Talley, L. D. (2011). *Descriptive physical oceanography: an introduction*. Academic press.

Taylor, A., Colebrook, J., Stephens, J., & Baker, N. (1992). Latitudinal displacements of the Gulf Stream and the abundance of plankton in the north-east Atlantic. *Journal of the Marine Biological Association of the United Kingdom*, *72*, 919–921.

Taylor, A., & Stephens, J. (1980). Latitudinal displacements of the gulf-stream (1966 to 1977) and their relation to changes in temperature and zooplankton abundance in the NE Atlantic. *Oceanologica Acta*, *3*, 145–149.

Taylor, A. H. (1995). North–south shifts of the Gulf Stream and their climatic connection with the abundance of zooplankton in the UK and its surrounding seas. *ICES Journal of Marine Science: Journal du Conseil*, *52*, 711–721.

Taylor, A. H., Jordan, M. B., & Stephens, J. A. (1998). Gulf Stream shifts following ENSO events. *Nature*, *393*, 638–638.

Taylor, A. H., & Stephens, J. A. (1998). The North Atlantic oscillation and the latitude of the Gulf Stream. *Tellus A*, *50*, 134–142. doi:10.1034/j.1600-0870.1998.00010.x.

Tomczak, M., & Godfrey, J. S. (2003). *Regional oceanography: an introduction*. Daya books.

Trenberth, K., & Hurrell, J. (1999). Commentary and analysis-Comments on The Interpretation of Short Climate Records with Comments on the North Atlantic and Southern Oscillations. *Bulletin of the American Meteorological Society*, *80*, 2721–2722.

Troupin, C., Barth, A., Sirjacobs, D., Ouberdous, M., Brankart, J.-M., Brasseur, P., Rixen, M., Alvera-Azcárate, A., Belounis, M., Capet, A. et al. (2012). Generation of analysis and consistent error fields using the Data Interpolating Variational Analysis (DIVA). *Ocean Modelling*, *52*, 90–101.

Troupin, C., Machin, F., Ouberdous, M., Sirjacobs, D., Barth, A., & Beckers, J.-M. (2010). High-resolution climatology of the northeast Atlantic using Data-Interpolating Variational Analysis (DIVA). *Journal of Geophysical Research: Oceans*, *115*.

Troupin, C., Ouberdous, M., Sirjacobs, D., Alvera-Azcárate, A., Barth, A., Toussaint, M.-E., Watelet, S., & Beckers, J.-M. (2015). Diva User Guide. `http://modb.oce.ulg.ac.be/mediawiki/index.php/Diva_documents`. [Online; accessed 23-September-2015].

Troupin, C., Ouberdous, M., Sirjacobs, D., Alvera-Azcárate, A., Barth, A., Toussaint, M.-E., Watelet, S., & Beckers, J.-M. (2016). Diva User Guide. `http://modb.oce.ulg.ac.be/mediawiki/index.php/Diva_documents`. [Online; accessed 30-June-2020].

Visbeck, M., Cullen, H., Krahmann, G., & Naik, N. (1998). An ocean model's response to North Atlantic Oscillation-like wind forcing. *Geophysical research letters*, *25*, 4521–4524.

Voituriez, B. (2006). *The Gulf Stream*. Unesco.

Wang, C., Zhang, L., Lee, S.-K., Wu, L., & Mechoso, C. R. (2014). A global perspective on CMIP5 climate model biases. *Nature Climate Change*, *4*, 201–205.

Watelet, S. (2020). Detrended SSH data set used for Rossby Wave Analysis, extraction at 39N from ORCA12.L46-MJM189 DRAKKAR simulation. URL: `https://doi.org/10.5281/zenodo.3968885`. doi:10.5281/zenodo.3968885.

Watelet, S., Beckers, J.-M., & Barth, A. (2017). Reconstruction of the Gulf Stream from 1940 to the Present and Correlation with the North Atlantic Oscillation. *Journal of Physical Oceanography*, *47*, 2741–2754. doi:10.1175/JPO-D-17-0064.1.

Watelet, S., Beckers, J.-M., Molines, J.-M., & Troupin, C. (2020a). Properties of baroclinic Rossby waves in the North Atlantic from eddy-resolving simulations of ocean circulation. *Ocean Science Discussions*, (pp. 1–18).

Watelet, S., Skagseth, Ø., Lien, V. S., Sagen, H., Østensen, Ø., Ivshin, V., & Beckers, J.-M. (2020b). A volumetric census of the Barents Sea in a changing climate. *Earth System Science Data Discussions*, (pp. 1–17).

Watelet, S., Skagseth, Ø., Lien S., V., Sagen, H., Østensen, Ø., Ivshin, V., & Beckers, J.-M. (2020c). Barents Sea Atlas. NMDC. doi:10.21335/NMDC-2058021735.

Wentz, F. J., Gentemann, C., Smith, D., & Chelton, D. (2000). Satellite measurements of sea surface temperature through clouds. *Science*, *288*, 847–850.

Wilks, D. S. (1995). *Statistical methods in the atmospheric sciences, an introduction* volume 59. Academic press.

Wilks, D. S. (2011). *Statistical methods in the atmospheric sciences* volume 100. Academic press.

Wunsch, C. (1999). The interpretation of short climate records, with comments on the North Atlantic and Southern Oscillations. *Bulletin of the American Meteorological Society*, *80*, 245–256. doi:10.1175/1520-0477(1999)080<0245:TIOSCR>2.0.CO;2.

Xu, H., Miller, T. J., Hameed, S., Alade, L. A., & Nye, J. A. (2018). Evaluating the utility of the Gulf Stream Index for predicting recruitment of Southern New England-Mid Atlantic yellowtail flounder. *Fisheries Oceanography*, *27*, 85–95.

Yang, X.-Y., Yuan, X., & Ting, M. (2016). Dynamical link between the Barents–Kara sea ice and the Arctic Oscillation. *Journal of Climate*, *29*, 5103–5122.

Zweng, M., Reagan, J., Seidov, D., Boyer, T., Locarnini, R., Garcia, H., Mishonov, A., Baranova, O., Weathers, K., Paver, C. et al. (2018). World Ocean Atlas 2018. *Salinity*, (p. 50).